Technical Physics Letters, Vol. 29, No. 6, 2003, pp. 441–443. Translated from Pis'ma v Zhurnal Tekhnicheskoĭ Fiziki, Vol. 29, No. 11, 2003, pp. 1–6.

Measuring Radiative Losses in the Globus-M Spherical Tokamak

B. Feng, P. G. Gabdullin, V. G. Kapralov, B. V. Kuteev, A. S. Smirnov, V. K. Gusev, S. I. Lashkul, Yu. V. Petrov, and N. V. Sakharov

St. Petersburg State Technical University, St. Petersburg, 195251 Russia
e-mail: root@phtf.stu.neva.ru
Ioffe Physicotechnical Institute, Russian Academy of Sciences, St. Petersburg, 194021 Russia
Received January 15, 2003

Abstract—We report on the first measurement of the absolute values of radiative losses in the Globus-M spherical tokamak. Measured by a wide-aperture pyroelectric bolometer, the radiative losses amount to about 30% of the total power deposited in the discharge, which is indicative of a sufficiently high purity of plasma in the experimental setup. Radiative losses on such a level have to be taken into account in determining the energy confinement time of the tokamak plasma. A new method is proposed for calibrating the bolometer using the data of other diagnostic techniques for the current ramp up stage, which provides for a coincidence up to within 15% with the calibration data obtained on a test bench. *© 2003 MAIK "Nauka/Interperiodica".*

Spherical tokamaks, which have been extensively developed and investigated in recent years [1] as possible magnetic traps for controlled thermonuclear fusion, represent interesting physical objects with insufficiently studied plasma properties. A special feature of these systems is a small aspect ratio $A = R/a \sim 1.5$ (where R and a are the major and minor radii of the tokamak torus, respectively). A decrease in the A value emphasizes toroidal effects in the plasma, on the one hand, and significantly (up to 40%) increases the efficiency of utilization of the magnetic field B, on the other hand. The latter efficiency is characterized by the ratio of pressures of the plasma and the magnetic field and expressed as $\beta = nT/(B^2/8\pi)$ (T and n being the temperature and density of the plasma, respectively). The Globus-M spherical tokamak (Ioffe Physicotechnical Institute, Russian Academy of Sciences, St. Petersburg) is a modern device with discharge parameters typical of medium-size machines (a = 0.24 m; R = 0.36 m; B = 0.6 T; plasma current I = 0.3 MA) [2].

The integral energy balance in the tokamak is described by the equation

$$\frac{\partial W}{\partial t} = P_{\mathrm{OH}} - \frac{W}{\tau_{\mathrm{E}}} - P_{\mathrm{rad}},$$

where W is the energy confined in the plasma, P_{OH} is the ohmic heating power, and τ_{E} is the energy confinement time of the plasma. Investigation of the transport component of the energy confinement and determination of the τ_{E} value require knowledge of the radiative loss power P_{rad}. In addition, the ratio of radiative and transport losses characterizes the fraction of impurities in the plasma, which is an important parameter of the quality of the tokamak plasma.

This Letter reports on the first measurement of the absolute values of radiative losses in a spherical toka-

The parameters of plasma in the spherical tokamak Globus-M

Pulse no.	I_{p}, kA	U_{loop}, V	U_{bol}, V	N_{42}, 10^{14} cm^{-2}	P_{rad}, kW	P_{OH}, kW	$P_{\mathrm{rad}}/P_{\mathrm{OH}}$, %	H_α, a.u.
3021	152	3.23	5.56	10.6	167	468	35.6	15
3022	155	3.32	5.85	10.5	173.8	493	35.2	15
3023	160	3.3	5.89	12.1	175.6	488.5	35.9	12
3024	140	3.32	5.89	12.5	178	451	39.5	26
3025	154	3.31	5.89	15.4	169	487	34.7	55
3026	156	3.3	5.82	16.1	175	519	33.6	57
3033	66	4.4	2.56	5.8	85	277	31	164

1063-7850/03/2906-0441$24.00 © 2003 MAIK "Nauka/Interperiodica"

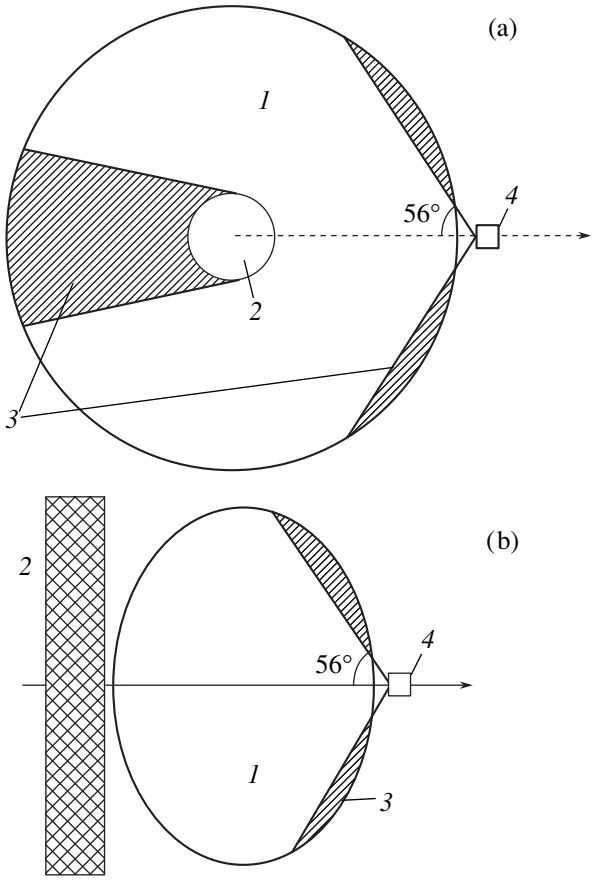

Fig. 1. Schematic diagrams illustrating the measurement of plasma radiation in the spherical tokamak Globus-M: (a) top view; (b) vertical section of the tokamak at the position of a pyrometric bolometer; (*1*) observation zone; (*2*) central rod; (*3*) shadow zone; (*4*) bolometer.

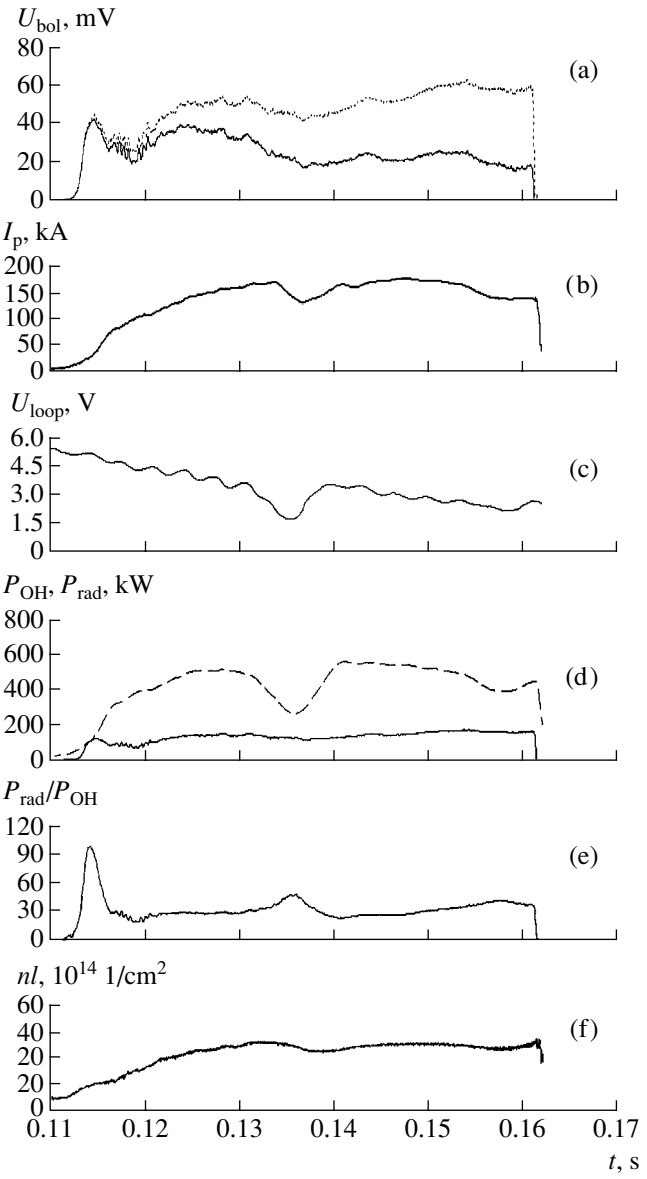

Fig. 2. A set of diagnostic signals for the spherical tokamak Globus-M (pulse No. 3023): (a) primary (dashed curve) and restored (solid curve) bolometer signals; (b) current; (c) voltage on the torus loop; (d) ohmic heating (dashed curve) and radiative loss (solid curve) power; (e) the ratio of radiative loss to ohmic heating power; (f) linear plasma density along the central chord.

mak of the Globus-M type, performed using wide-aperture pyroelectric bolometer [3].

The region of plasma monitored by the bolometer is indicated in Fig. 1. A special feature of the spherical tokamak is that, because of the small size of the central rod, the volume of plasma directly observed by the bolometer is close to the total plasma volume *V*. Under the experimental conditions employed, this effectively monitored plasma volume was 0.8*V*. Taking into account that the radiation is inhomogeneously distributed over the volume (confined in a near-wall region), we have calculated profiles of the types $I = I(\rho/a)^2$ and $I = I(\rho/a)^4$ in order to take into account the growth of radiative losses near the walls and, thus, to estimate a contribution due to the radiation registered. According to the results of these calculations, the fraction of radiation received by the bolometer amounts to 0.785 and 0.695, respectively. These estimates confirm that the bolometer detects the main fraction of plasma radiation even when it is emitted from a plasma edge at the wall surface. This circumstance removes the problem encountered in traditional tokamaks, where it is necessary to extrapolate the results of local radiation measurements to the entire chamber volume.

Figure 2a shows a typical primary signal of the bolometer. Preliminary calibration experiments using a laser source showed that the differentiation time constant of the bolometer was 30 ms at a sensitivity of 1.43 (V cm^2)/W. A signal profile restored with allowance of the differentiation time constant is presented in the same figure. As can be seen, the plasma radiation intensity increases with time and generally follows variations of the plasma current (Fig. 2b). In order to

provide for the absolute calibration of the bolometer the signal power was normalized to the power of ohmic heating at the point of maximum plasma radiation power. In calculating the ohmic power, we subtracted the inductive component from the power (*I*U*) supplied to the plasma.

As can be seen from Fig. 2a, the maximum of the radiation intensity is attained at 118 ms. At this time, the discharge current becomes sufficiently large (40 kA) and the magnetic field configuration is formed. At the same time, the temperature and density of the plasma are still low and, hence, the transport losses can be ignored in comparison to the radiative losses. Neglecting also the derivative of the energy supplied to the plasma, we find upper bound estimation of the radiative losses. This calibration of the bolometer coincided to within 15% with the results of the laser calibration. This method can be recommended for the permanent absolute calibration of bolometers under the experimental conditions on tokamaks, where it is difficult to ensure constant absorption properties of the bolometer surface.

As can be seen from Fig. 2e, the ratio of radiative power to the ohmic heating component drops sharply (to a level of 0.25) after passing through the maximum and then slowly increases again (not exceeding 0.3–0.4 in the middle part of the discharge). The ratios of radiative losses to ohmic power in the middle part of the discharge for various discharge parameters are presented in the table. As can be seen, the radiative losses do not exceed 40% of the ohmic power level. This fact is indicative of a sufficiently high purity of plasma in the described experiments. At the same time, radiative losses are sufficiently large and have to be taken into account in determining the energy confinement time of the tokamak plasma.

REFERENCES

1. A. Sykes, Control. Fus. Plasma Phys. **40** (Suppl. 11B), A127 (2000).
2. V. K. Gusev, V. E. Golant, E. Z. Gusakov, *et al.*, Zh. Tekh. Fiz. **69** (9), 58 (1999) [Tech. Phys. **44**, 1054 (1999)].
3. B. Feng, P. G. Gabdullin, V. G. Kapralov, *et al.*, *Proceedings of the Int. Conf. "Engineering Problems of Thermonuclear Reactors", 27–30.10.2002, St. Petersburg*, p. 196.

Translated by P. Pozdeev

Technical Physics Letters, Vol. 29, No. 6, 2003, pp. 444–446. Translated from Pis'ma v Zhurnal Tekhnicheskoĭ Fiziki, Vol. 29, No. 11, 2003, pp. 7–13.

The Effect of Pulsed Magnetic Fields on High-Temperature Superconductor $YBa_2Cu_3O_{7-x}$ Ceramics

M. N. Levin, V. V. Postnikov, and M. A. Dronov

Voronezh State University, Voronezh, Russia

e-mail: levin@lev.vsu.ru

Received January 8, 2003

Abstract—We have observed a change in the sign of the temperature coefficient of resistance of $YBa_2Cu_3O_{7-x}$ ceramics in the region of the superconducting transition under the action of relatively weak (<1 T) pulsed magnetic fields. The effect is probably caused by the transition of the oxide based superconductor from the normal metallic state to a pseudogap regime as a result of the partial loss of oxygen atoms from Cu–O chains. © *2003 MAIK "Nauka/Interperiodica".*

Previously, we established the unique ability of relatively weak (<1 T) pulsed magnetic fields (PMFs) to produce significant effects upon the real structure and physical properties of a broad class of nonmagnetic materials, including silicon crystals [1], $A^{III}B^{V}$ semiconductor compounds [2], ferroelectrics with hydrogen bonds [3], and crystallizable polymers [4].

An important feature of the observed phenomenon is that the energy of the PMF action inducing these effects is negligibly small as compared to the thermal energy of the crystal: $\mu_B B \le 10^{-3} kT$, where μ_B is the Bohr magneton, B is the magnetic field induction, k is the Boltzmann constant, and T is the absolute temperature. It was suggested that the PMF action is of a spin nature and is capable of initiating decomposition of defect complexes in real crystals by lifting prohibitions for the intercombination transitions. These transitions excite chemical bonds in the defect complexes, after which the rupture of PMF-excited bonds (and decomposition of these complexes) takes place at the expense of thermal energy taken from the crystal lattice.

In view of the fact that an exhaustive phenomenological pattern of PMF-induced effects in real crystals is far from being outlined and the mechanisms of PMF action are insufficiently clear, it is expedient to proceed with a consistent search for and investigation of objects capable of changing their properties under the action of this factor.

In the experiments described below, we have studied the influence of the PMF treatment upon a high-temperature superconductor (HTSC) based on an Y–Ba–Cu–O (YBCO) compound with respect to the temperature dependence of the electric resistance in the region of the phase transition to a superconducting state.

The investigation was performed on the samples of $YBa_2Cu_3O_{7-x}$ ($0 < x < 1$) ceramics prepared from a homogeneous mixture of fine powders of Y_2O_3, $BaCO_3$, and CuO by two-stage sintering in air (5 h at 1200 K + 5 h at 1250 K) followed by slow cooling. The ceramics selected for the experiments were characterized by a sharp "total" transition into a superconducting state at $T_c = 90 \pm 0.5$ K. The samples had the shape of rectangular parallelepipeds with dimensions $1.5 \times 5 \times 20$ mm. Leads connecting the samples to a measuring circuit were soldered to indium contacts fused into 1.5×5 mm end faces of the samples. The electric resistance was measured by a standard four-point-probe technique in a cryostat cooled by liquid nitrogen. The temperature was varied in the interval from 77 to 300 K and monitored by a germanium resistance thermometer to within 0.05 K or below. The rate of temperature variation was automatically controlled and amounted to 0.5 K/min in the region of superconducting transition.

The PMF treatment consisted in exposure to a series of $N = 3000$ unipolar symmetric pulses of a nearly triangular shape with a duration of $\tau = 4 \times 10^{-5}$ s, a repetition rate of $f = 50$ Hz, and an amplitude of $B_0 = 0.3$, 0.35, or 0.5 T. The magnetic field pulses were generated by discharge of a capacitor bank through a low-inductance solenoid coil. A sample to be treated was placed into a copper capsule kept at a temperature controllable within 400–420 K but maintained constant during the PMF treatment. After the exposure, the capsule with the sample was cooled to room temperature and the sample was transferred into the thermostat and connected to the measuring circuit. The temperature dependence of the sample resistance, $\rho(T)$, was measured upon keeping the samples for various times after the PMF treatment. Between the measurements, the samples were stored in air at room temperature.

The effect of the PMF treatment on the high-T_c $YBa_2Cu_3O_{7-x}$ ceramics is illustrated in Fig. (1). As can be seen, treating the samples by PMF at an induction amplitude B_0 and a temperature below certain threshold

1063-7850/03/2906-0444$24.00

values does not induce significant changes in the $\rho(T)$ curves before the superconducting transition (curves *1–3*). At the same time, these PMF treatments led to the appearance of residual resistance at temperatures below the superconducting transition (T_c = 90 K), whereby both the magnitude of this residual resistance and the temperature interval in which it was observed increased with the PMF amplitude and the treatment temperature.

The basic result is that, upon reaching a certain threshold value of the PMF amplitude (in our experiments, B_0 = 0.5 T at T = 420 K), the character of the temperature dependence of the electric resistance of HTSC ceramics changed in a radical manner. Upon such PMF treatment, the initial $\rho(T)$ curve characterized by a sharp jump in the resistance at T_c and a nearly linear increase in the resistance with the temperature at $T > T_c$ (curve *1*) changes to a smooth nonlinear curve describing a monotonic decrease in the resistance with increasing temperature (curve *4*). Note that the thermal treatment of the same samples for 10 min at T = 420 K in the absence of a PMF did not lead to any changes in the temperature profile of the resistance.

It is important to note that the PMF treatment alters the sign of the temperature coefficient of resistance, which is evidence of a change in the mechanism of conductivity of HTSC ceramics as a result of this action. The PMF-induced change in the character of the temperature dependence of resistance of high-T_c $YBa_2Cu_3O_{7-x}$ ceramics is followed by prolonged (hundreds of hours at T = 300 K) relaxation of the sample to the initial state (Fig. 1, curves *5–7*).

The whole body of experimental data can be interpreted as follows. It is known that the phase state of $YBa_2Cu_3O_{7-x}$ at a given temperature T is determined by the proportion and the character of distribution of oxygen vacancies in the linear Cu–O chains representing a reservoir of charge carriers for the superconducting CuO_2 planes [5, 6]. As the parameter x varies from 1 to 0, the properties of these ceramics can change from dielectric to superconducting.

Figure 2 presents a qualitative phase diagram showing the main phase states in which $YBa_2Cu_3O_{7-x}$ ceramics can occur, depending on the content of oxygen vacancies (x) and the temperature: dielectric antiferromagnetic (AF), superconducting (SC), and metallic (M). The existence of these phases in superconducting cuprates is well established [5, 6]. In addition, the phase diagram shows a conditional region representing the so-called pseudogap regime (PGR), which has been identified quite recently. The pseudogap regime differs from the normal metallic state by reduced density of electron states near the Fermi level.

One possible reason for the density of single-particle states to decrease with the temperature (the behavior characteristic of PGR) is the pairing of electrons at a temperature below the crossover temperature T^* of the normal metallic state. In order to participate in the current transfer, such electron pairs have to overcome a certain potential gap. This circumstance determines a complicated character of the temperature dependence of electric resistance in the pseudogap region. As the temperature decreases, the amount of paired electrons increases, while both the density of conduction electrons and the fraction of electron pairs contributing to the conductivity decrease. The negative sign of the tem-

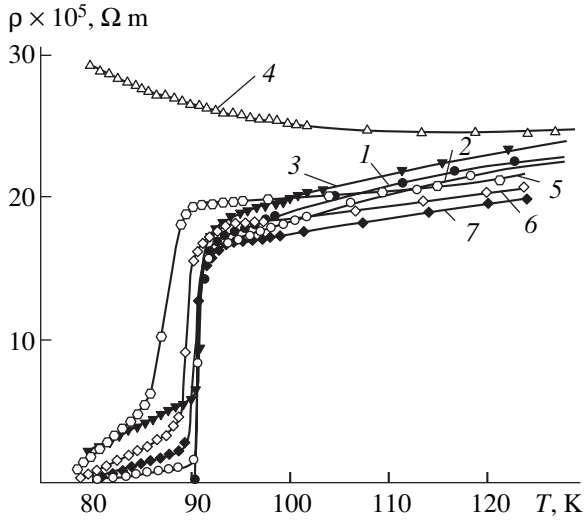

Fig. 1. Temperature dependences of the electric resistance of $YBa_2Cu_3O_{7-x}$ ceramics: (*1*) initial; (*2–4*) measured 1 h after 1-min PMF treatment at B_0 = 0.3 T (T = 400 K), 0.32 T (T = 410 K), and 0.5 T (T = 420 K), respectively; (*5–7*) measured 24, 48, and 120 h, respectively, after PMF at B_0 = 0.5 T (T = 420 K).

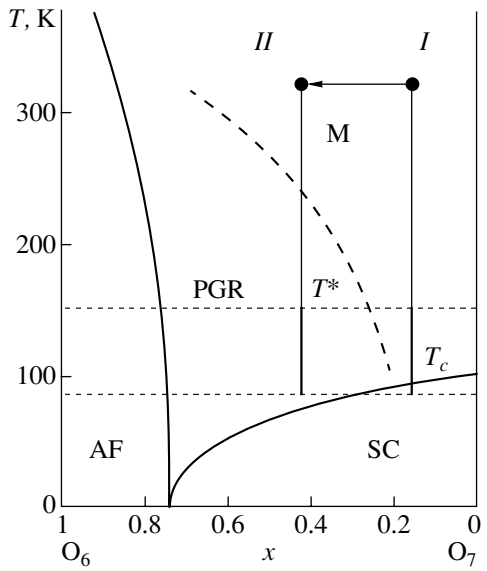

Fig. 2. Qualitative phase diagram of $YBa_2Cu_3O_{7-x}$ ceramics: (AF) antiferromagnetic phase; (SC) superconducting phase; (M) metallic phase; (PGR) pseudogap region; T^* and T_c are the temperatures of transitions from metallic to pseudogap and superconducting states, respectively.

perature coefficient of resistance (typical of the pseudogap region) indicates that a drop in the conductivity caused by a decrease in the carrier density with decreasing temperature is not compensated by an increase in the conductivity related to a lower scattering of the charge carriers on phonons.

If the PMF action leads to a decrease in the oxygen content in the linear Cu–O chains (or to an increase in the concentration x of oxygen vacancies), the point characterizing the state of the sample on the x–T phase diagram will shift leftward. As can be seen from Fig. 2, this shift can account for a transition of the sample from the metallic state with a positive temperature coefficient of resistance to a pseudogap state with a negative coefficient. As a result, the superconducting transition temperature decreases and may even fall outside the temperature interval studied.

The right-hand thick solid line (*I*) in Fig. 2 corresponds to the temperature dependence of resistance upon the transition of the initial sample from metallic to superconducting state (Fig. 1, curve *1*), while the left-hand thick solid line (*II*) corresponds to the temperature dependence of resistance upon the transition to the pseudogap regime under the action of PMF (Fig. 1, curve *4*). The above assumption concerning the loss of some weakly bound oxygen atoms from the linear Cu–O chains in $YBa_2Cu_3O_{7-x}$ ceramics under the PMF action was based on the previously observed PMF-induced escape of oxygen atoms from Si–O–Si interstitials in Czochralski-grown silicon crystals (Cz–Si) [1] with ultimately high concentration of dissolved oxygen.

A probable starting mechanism of the PMF-induced effects in Cz-Si crystals was suggested to consist in the excitation of the Si–O bonds of interstitial oxygen via occupation of the vibrational levels of a metastable term [1]. A distinctive feature of this mechanism is the existence of a threshold with respect to the PMF amplitude and a sufficiently high temperature required for occupation of the upper vibrational states of the metastable term. The presence of these signs in the PMF-induced effect observed in $YBa_2Cu_3O_{7-x}$ ceramics suggests that this phenomenon can also be explained within the framework of the same model [1] (at least in this stage of investigations and at the present-day level of knowledge of PMF-induced effects).

Oxygen liberated from the Cu–O chains under the PMF action can be trapped at the ceramic grain boundaries or escape into atmosphere. As is known, weakly bound oxygen of Cu–O chains can also escape from $YBa_2Cu_3O_{7-x}$ crystals under usual thermal action, but this process takes place at much higher temperatures ($T > 800$ K) [5].

Relaxation of the ceramic sample after the PMF action seems to be determined by a decrease in the oxygen deficiency in the Cu–O chains, which is related to the return of oxygen from the ceramic grain boundaries and/or its supply from the atmosphere. The prolonged character of the relaxation is explained by the process of oxygen diffusion, which is rather slow at room temperature. The fact that the initial temperature dependence of the sample resistance is not fully restored could be related to the difference between the distribution of oxygen vacancies in the Cu–O chains before and after PMF treatment.

In conclusion, it should be noted that the observed effect provides additional possibilities for controlled modification of the real structure and properties of oxide based high-T_c superconductors.

REFERENCES

1. M. N. Levin and B. A. Zon, Zh. Éksp. Teor. Fiz. **111** (4), 1373 (1997) [JETP **84**, 760 (1997)].
2. M. N. Levin, G. V. Semenova, T. P. Sushkova, *et al.*, Pis'ma Zh. Tekh. Fiz. **28** (19), 50 (2002) [Tech. Phys. Lett. **28**, 818 (2002)].
3. M. N. Levin, V. V. Postnikov, M. Yu. Palagin, and A. M. Kostsov, Fiz. Tverd. Tela (St. Petersburg) **45**, 513 (2003) [Phys. Solid State **45**, 542 (2003)].
4. M. N. Levin and M. N. Matveev, Zh. Fiz. Khim. **75**, 1886 (2001).
5. N. M. Plakida, *High-Temperature Superconductors* (Mezhd. Progr. Obraz., Moscow, 1996).
6. E. Dagotto, Rev. Mod. Phys. **66**, 763 (1994).
7. T. Timusk and B. Statt, Rep. Prog. Phys. **62**, 61 (1999).

Translated by P. Pozdeev

Technical Physics Letters, Vol. 29, No. 6, 2003, pp. 447–449. Translated from Pis'ma v Zhurnal Tekhnicheskoĭ Fiziki, Vol. 29, No. 11, 2003, pp. 14–19.

Determining Characteristics of a Microsecond Plasma Opening Switch at the Moment of Current Interruption

S. V. Loginov

Institute of High-Current Electronics, Siberian Division, Russian Academy of Sciences, Tomsk, Russia
e-mail: loginov@oit.hcei.tsc.ru

Received January 10, 2003

Abstract—A new approach to determining characteristics of a microsecond plasma opening switch at the moment of current interruption is proposed. Dependences of the switch voltage and resistance on the current and geometric parameters are presented, and the calculated values of the resistance are compared to the experimental data. © *2003 MAIK "Nauka/Interperiodica".*

Plasma opening switches are used as interrupters providing for power profile sharpening in inductive energy storage systems [1]. The existing theoretical descriptions of such switches explain the penetration of a magnetic field into the switch plasma in the conduction phase, but the calculated values of resistance at the moment of current interruption do not agree with the available experimental data. The switch plasma dynamics can be traced in detail by numerical simulation methods, but such analysis must involve calculation of a large number of variants in order to reveal the laws of switch operation.

This Letter proposes a new approach to calculating characteristics of a microsecond plasma opening switch, the results of which agree with experiment.

A plasma opening switch (Fig. 1) is essentially a crosspiece of length L in a coaxial vacuum line of an inductive energy storage with the cathode and anode radii r and R, respectively, which is preliminarily filled with a plasma of density n injected from the anode side. In microsecond switches, the conduction current is much smaller than that related to the directed motion of ions in a bipolar saturation current [2], $I_{sat} = (m_i/mZ)^{1/2}2\pi env_d rL$, where m and e are the electron mass and charge; m_i and Z are the ion mass and charge; v_d is the ion drift velocity.

Under the action of the pressure of the magnetic field created by the current passing in the switch, the plasma is accelerated in the axial direction. At the end of the conduction phase, the plasma velocity can be estimated as

$$u \sim v_A = \frac{B}{(4\pi m_i n/Z)^{1/2}},$$

where $B = 2I/cr$ [3]. Since v_A depends on the radius and the plasma density, the plasma may exhibit a certain radial shift toward electrodes in addition to homogeneous drift in the axial direction. As a result, a vacuum gap may form in the field penetration region so that the plasma surface on the storage side would become concave (Fig. 1).

Penetration of the magnetic field into the switch plasma leads to suppression of the electron conduction in the radial direction as a result of the magnetic isolation of electrons. The switch length in the axial direction, accessible for shunting at the end of the conduction phase, decreases to a certain value $l_s = (I_s/I_{sat})L$. This value is defined as the length necessary to close a conduction current I_s in the bipolar regime: $I_s = (m_i/Zm)^{1/2}j_{i\,sat}S$, where $j_{i\,sat} = env_d$ and $S = 2\pi rl_s$. As l_s decreases further, the current I_s becomes greater than the bipolar saturation current. This can lead to plasma erosion and the formation of a vacuum gap d in which the electron component of the current is magnetically

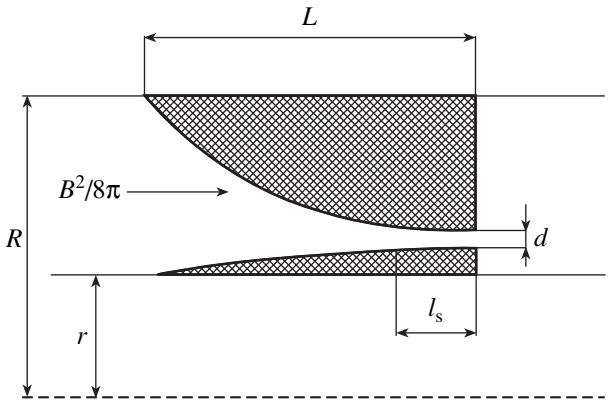

Fig. 1. Plasma opening switch geometry (see the text for explanations).

1063-7850/03/2906-0447$24.00 © 2003 MAIK "Nauka/Interperiodica"

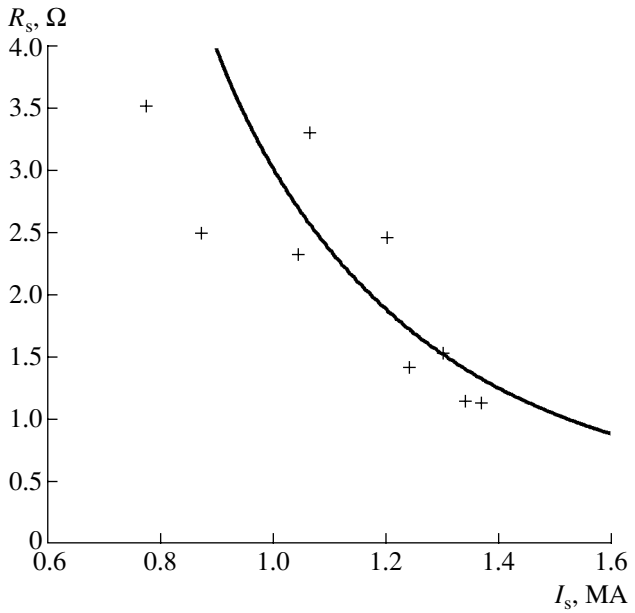

Fig. 2. The calculated switch resistance $R_s(I_s)$ (solid curve) in comparison to experimental data (+).

insulated. The current and the voltage across the switch are related to the gap width as [2]

$$I_s \cong I_{mi} = \beta \frac{mc^3}{e}(\gamma^2 - 1)^{1/2}\frac{r}{d}, \quad (1)$$

where $\gamma = 1 + eU_s/mc^2$ and $\beta = 0.5$–1 [4]. When the switch operates without load, the current decay at the moment of interruption is small and it can be assumed that $I_s \approx \text{const}$.

The decrease of l_s and the growth of d take place over the time $t_s = l_s/u$. For $0 \le z \le l_s$, the gap width increases for the time $t = z/u$ at the rate

$$\dot{d} = \left(\frac{l_s}{l_s - ut} - 1\right)v_d, \quad (2)$$

and after the electron current cutoff for $t = (l_s - z)/u$, at the rate

$$\dot{d} = \left(\frac{j_i}{j_{i\,sat}} - 1\right)v_d. \quad (3)$$

Here,

$$j_i = F\left(\frac{Zm}{m_i}\right)^{1/2}\frac{\sqrt{2}}{9\pi}\frac{mc^3}{e}\frac{(\gamma-1)^{3/2}}{d^2},$$

F is the coefficient of the ion current amplification related to the space charge of magnetized electrons [5]. According to Eq. (2),

$$d = \frac{v_d}{u}\left(l_s \ln\frac{l_s}{l_s - z} - z\right), \quad (4)$$

while Eq. (3) yields, in the approximation of $\gamma \gg 1$ and $v_d \ll \dot{d}$ with allowance for Eq. (1),

$$d = \left(\frac{F}{\beta^{3/2}}\frac{\sqrt{2}}{3}\left(\frac{I_s}{mc^3/e}\right)^{1/2}\frac{l_s}{\sqrt{r}}\frac{v_d}{u}(l_s - z)\right)^{2/3}. \quad (5)$$

The resultant gap, defined as the sum of expressions (4) and (5), reaches a minimum value of

$$d_m = \frac{v_d}{u}l_s \ln\frac{l_s}{\Delta}e^{1/2} \quad (6)$$

(where $\Delta = l_s - z_m$) at the point

$$z_m = l_s\left(1 - \frac{\beta^{3/2}}{F}\left(\frac{3^5}{2^4}\frac{mc^3/e}{I_s}\frac{r}{l_s}\frac{v_d}{u}\right)^{1/2}\right). \quad (7)$$

The magnetohydrodynamic model [6] yields the conduction time and current values in agreement with experiment. For a linear current growth rate $\dot{I}$, the conduction current is

$$I_s = \left(6\pi\frac{m_i c^2}{Z}\right)^{1/4}(\dot{I}^2 r^2 L^2 n/k)^{1/4}, \quad (8)$$

where $k = \dfrac{\ln R/r}{(R/r)^2 - 1}$. The speed of the magnetic field penetration into the switch plasma at the end of the conduction phase is

$$u = \sqrt{2k/3}\,v_A. \quad (9)$$

Using relations (8) and (9), expression (6) can be rewritten as

$$d = \left(\frac{3}{2k}\right)^{1/2}\frac{c}{\omega_p}\ln\frac{l_s}{\Delta}e^{1/2}, \quad (10)$$

where $\omega_p = (4\pi ne^2/m)^{1/2}$. Formula (10) indicates that the gap width decreases with increasing plasma density as $\sqrt{n}$. Excluding the plasma density through formula (8) yields an expression involving the switch current, which is more convenient for comparison with experiment:

$$d = \frac{3}{2}\frac{mc^2}{e}\left(\frac{m_i}{Zm}\right)^{1/2}\frac{\dot{I}rL}{kI_s^2}\ln\frac{l_s}{\Delta}e^{1/2}. \quad (11)$$

Substituting formula (10) into Eq. (1), it is possible to calculate the voltage drop across the switch and the corresponding resistance. For $\gamma \gg 1$, the switch voltage is given by the formula

$$U_s = \frac{3}{2}\left(\frac{m_i}{Zm}\right)^{1/2}\frac{mc}{e}\frac{L\dot{I}}{k\beta I_s}\ln\frac{l_s}{\Delta}e^{1/2}. \quad (12)$$

Figure 2 shows the results of calculations of the switch resistance $R_s = U_s/I_s$ in comparison to the experimental data. As can be seen, the calculated dependence agrees well with the experimental behavior. The calcu-

lations were performed for the switch with $r = 3.8$ cm, $R = 10$ cm, and $L = 12.4$ cm. The concentration of C^{++} ions in the plasma was varied from 10^{14} to 10^{16} cm^{-3} and the ion drift velocity was $v_d = 2$ cm/μs; the current parameters were $\dot{I} = 1.8$ kA/ns; $F = 5$; and $\beta = 0.5$. For $I_s \sim 1$ MA, the plasma density is $n \sim 1.2 \times 10^{15}$ cm^{-3} and $l_s \sim 1$ cm. With increasing n, the length l_s decreases as $\sim n^{-3/4}$.

According to formula (12), the switch resistance is inversely proportional to I_s^2. In the case of a linear current growth in the switch, the resistance will be inversely proportional to the charge transferred. This behavior was experimentally observed in GIT-4 [7] and GIT-12 [8] setups.

The voltage across the switch is $\sim \dot{I}^{1/2} \sim U_0^{1/2}$, where U_0 is the generator output voltage. This behavior is close to the dependence $(\sim U_0)^{4/7}$ reported in [9], which is consistent with a large volume of experimental data for various setups.

Thus, using the proposed approach, it is possible to determine the characteristics of a microsecond plasma opening switch at the moment of current interruption and to establish their dependence on the system parameters. The switch resistance can be calculated using the initial plasma density n.

REFERENCES

1. V. M. Bystritskiĭ, G. A. Mesyats, A. A. Kim, *et al.*, Fiz. Élem. Chastits At. Yadra **23**, 19 (1992) [Sov. J. Part. Nucl. **23**, 7 (1992)].
2. P. F. Ottinger, S. A. Goldstein, and R. A. Meger, J. Appl. Phys. **56**, 774 (1984).
3. A. S. Chuvatin, A. A. Kim, V. A. Kokshenev, and S. V. Loginov, Izv. Vyssh. Uchebn. Zaved., Fiz., No. 12, 56 (1997).
4. S. Ya. Belomyttsev and V. V. Ryzhov, Pis'ma Zh. Tekh. Fiz. **27** (14), 74 (2001) [Tech. Phys. Lett. **27**, 608 (2001)].
5. K. D. Bergeron, Appl. Phys. Lett. **28**, 306 (1976).
6. B. V. Weber, R. J. Commisso, G. Cooperstein, *et al.*, *Proc. 8th Int. Conf. on High-Power Particle Beams, Novosibirsk, 1990*, pp. 406–413.
7. A. N. Bastrikov, B. M. Kovalchuk, S. V. Loginov, *et al.*, *Proc. 12th Symp. on High-Current Electronics, Tomsk, 2000*, pp. 360–362.
8. V. A. Kokchenev, N. E. Kurmaev, and F. I. Fursov, *Proc. 12th Symp. on High-Current Electronics, Tomsk, 2000*, pp. 268–273.
9. G. I. Dolgachev and A. G. Ushakov, Fiz. Plazmy **27**, 121 (2001) [Plasma Phys. Rep. **27**, 110 (2001)].

Translated by P. Pozdeev

Technical Physics Letters, Vol. 29, No. 6, 2003, pp. 450–453. Translated from Pis'ma v Zhurnal Tekhnicheskoĭ Fiziki, Vol. 29, No. 11, 2003, pp. 20–29.

A Bidirectional Ring Fiber Laser with a 90° Faraday Rotator as the Nonreciprocal Phase Element. II. Experiment

R. V. Kiyan, A. A. Fotiadi, and O. V. Shakin

Ioffe Physicotechnical Institute, Russian Academy of Sciences, St. Petersburg, 194021 Russia

Received October 23, 2002; in final form, December 19, 2002

Abstract—The results of experimental investigation of an Er-doped fiber bidirectional ring laser with a 90° Faraday rotator in the cavity are presented. Two theoretically predicted regimes of the bidirectional generation of modes propagating in opposite directions with either complex-conjugate or orthoconjugate polarization states have been realized in practice. In each of these regimes, stable bidirectional generation of only one longitudinal mode propagating in each direction is possible. The former regime ensures significant stabilization of a nonreciprocal frequency shift between the modes propagating in opposite directions, this shift being determined by the Faraday phase rotator. © *2003 MAIK "Nauka/Interperiodica".*

Introduction. For creating a ring laser gyroscope based on an Er-doped fiber bidirectional ring laser, it is necessary (i) to suppress the effect of frequency locking of the counterpropagating modes, which is related to parasitic backscattering in the cavity, and (ii) to provide for the stable bidirectional generation of only one longitudinal mode propagating in each direction, with the stable frequency difference between the counterpropagating modes depending only on the angular rotation velocity of the cavity [1]. Unfortunately, the counterpropagating modes in an Er-doped fiber bidirectional ring laser are strongly coupled because of the significant homogeneous broadening of the line of erbium ion lasing in a quartz glass matrix [2]. The problem of suppressing undesired frequency locking was successfully solved [3, 4] by using a 45° Faraday phase rotator in the laser cavity.

However, the nonreciprocal frequency shift between the opposite modes, which is caused by the 45° Faraday phase rotator, strongly depends on the reciprocal birefringence of the laser cavity. This circumstance makes this frequency shift highly sensitive to various external perturbations inducing fluctuations in the reciprocal birefringence. Previously [5], we theoretically demonstrated that the problem can be solved by using a 90° Faraday phase rotator as a nonreciprocal element.

Experiment. Figure 1 shows a schematic diagram of the Er-doped fiber bidirectional ring laser used in our experiments. The laser cavity was made of a standard single-mode optical fiber. The nonreciprocal phase element in the cavity was the 90° ± 1° Faraday rotator (*1*). The birefringence of the laser cavity was controlled using two fiber polarizers of the RS-1 (*9*) and RS-2 (*10*) type. The longitudinal modes of the laser cavity were selected by means of a filter representing a short-length ring-shaped fiber cavity *3*. This element was also made of the standard single-mode optical fiber and coupled to the laser cavity via a 50/50 fiber coupler. The free spectral band of the ring fiber filter was about 900 MHz. The amplification medium represented an 11-cm-long piece of an Er-doped fiber (with an Er^{3+} ion content of about 2000 ppm). The activated fiber was pumped via a spectral-selective fiber coupler *4* of the WDM-1 type. The same coupler was used for extracting radiation propagating in the laser cavity. The radiation coupling coefficient was about 1% for waves propagating both clockwise and counterclockwise. The second spectral-selective fiber coupler *5* (WDM-2) was used for coupling a semiconductor pumping laser to the spectral-selective fiber coupler *4* (WDM-1). The pumping radiation wavelength was about 980 nm.

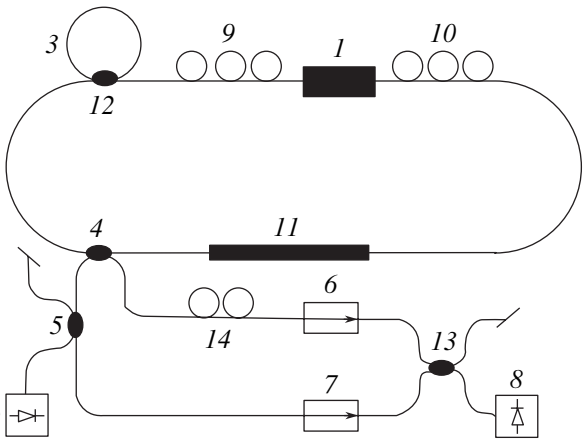

Fig. 1. A schematic diagram of the Er-doped fiber bidirectional ring laser: (*1*) 90° Faraday rotator; (*2*) 980-nm pumping laser; (*3*) ring fiber filter; (*4*, *5*) 1550/980 nm spectral-selective fiber couplers; (*6*, *7*) optical insulators; (*8*) photodetector; (*9*, *10*, *14*) polarizers; (*11*) amplifying medium; (*12*, *13*) fiber couplers.

1063-7850/03/2906-0450$24.00 © 2003 MAIK "Nauka/Interperiodica"

Both output arms of the laser contained polarization-independent fiber insulators preventing the influence of radiation backscattered outside the cavity on the laser operation. The output laser radiation corresponding to the modes propagating clockwise and counterclockwise was mixed in the 50/50 fiber coupler so as to obtain a signal of optical beats between the two modes. The polarization state of light in one of the output arms could be controlled using a fiber polarizer *14* (RS-3). This allowed the polarization states in both output arms to be made the same at the point of mixing (i.e., at the 50/50 fiber coupler). The extracted laser radiation was directed to a photodetector, the output signal of which was fed to an RF spectrum analyzer.

Since the optical elements entering into the laser cavity possess parasitic polarization-dependent losses, either unidirectional or bidirectional generation could be obtained depending on the tuning of polarization elements *9* and *10*. In both cases, the laser generated at a wavelength of 1.53 μm. First, by tuning the ring fiber filter, the laser cavity was adjusted so as to generate several longitudinal modes, whereby the spectrum of optical beats of the output radiation exhibited frequencies corresponding to the beats between these laser modes. In this way, we measured the free spectral band of the laser cavity, which amounted to 28.930 MHz. The accuracy of measurement was limited by the spectral width (~3 kHz) of the line of beats of the longitudinal modes.

Results and discussion. In the case of bidirectional single-mode generation, two qualitatively different regimes could be obtained through the corresponding tuning of polarizers *9* and *10*. In both these regimes, laser modes propagating in opposite directions possessed comparable intensities, so that the signal of beats between these modes could be observed in an oscillograph with a contrast of about 50%. In one of these regimes, a change in the tuning of polarizers *9* and *10* was accompanied by a smooth, continuous variation of the frequency of beats between the counterpropagating modes in the interval from about 100 kHz to $\Delta\nu/2$. According to the results of our theoretical analysis [5], this corresponds to the generation of orthoconjugate laser cavity modes propagating in opposite directions. Figure 2a shows the spectrum of beats between the counterpropagating modes observed in this case, with a beat frequency of 9.071 MHz.

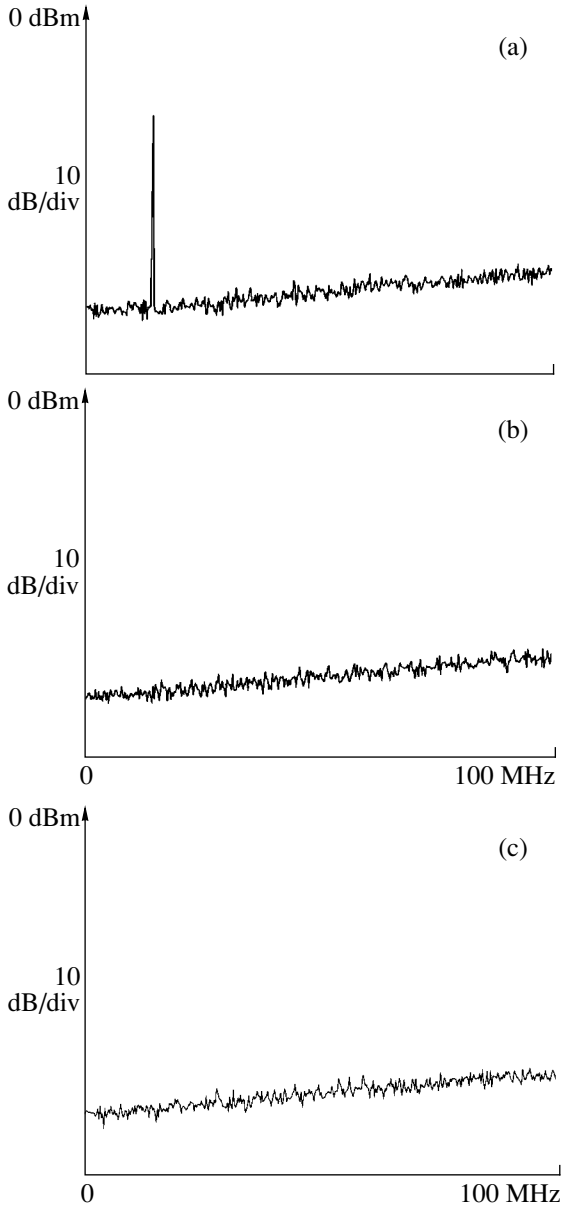

Fig. 2. RF spectra (a) of the signal of beats between counterpropagating modes with ortho- or complex-conjugate polarization states and (b, c) of the modes propagating clockwise and counterclockwise, respectively, for the Er-doped fiber bidirectional ring laser. All spectra were measured at a scan time of 604.8 ms and a spectral resolution of 9100 Hz.

By properly tuning polarizers *9* and *10*, it was also possible to obtain a bidirectional single-mode generation with a frequency of beats between the counterpropagating modes equal to 14.464 MHz. This value coincides, to within the accuracy of determination of the free spectral band of the laser cavity, with the $\Delta\nu/2$ value. The corresponding spectrum of beats between the counterpropagating modes is presented in Fig. 2a. In this generation regime, the frequency of beats remained unchanged even when the tuning of polarizers *9* and *10* was varied within rather broad limits. This tuning only changed the intensities of the counterpropagating modes and, hence, the amplitude of the beat signal. As was demonstrated theoretically [5], this behavior corresponds to the case when the laser generates opposite modes with complex-conjugate polarization states. Figures 2b and 2c show the RF spectra of each of the opposite modes. Since these spectra are virtually identical in the two regimes, the data are presented for one case only (the measurements were performed by directing the radiation from only one output

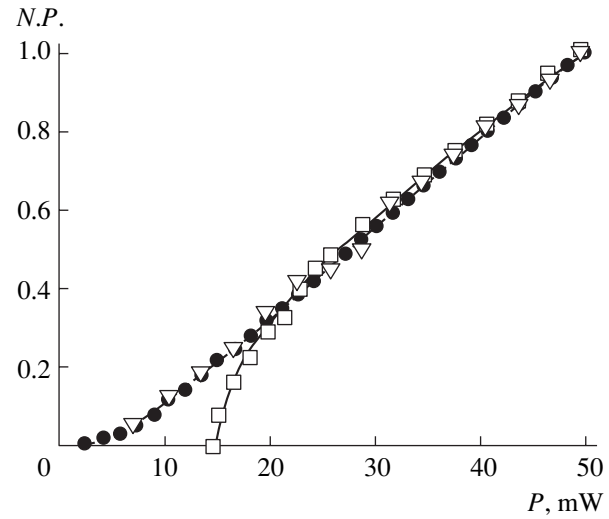

Fig. 3. Plots of the total output power (circles) and the amplitude of the signal of beats between counterpropagating modes with orthoconjugate (squares) and complex-conjugate (triangles) polarization states versus power pumped into activated fiber.

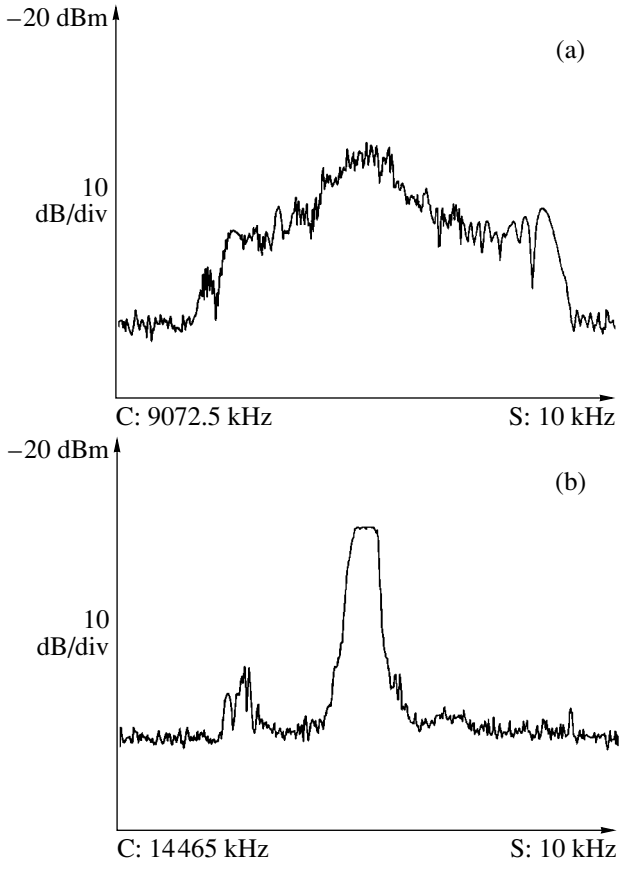

Fig. 4. RF spectra of the signal of beats between counterpropagating modes with (a) ortho- and (b) complex-conjugate polarization states (C: central frequency; S: spectral range). All spectra were measured at a scan time of 40 ms, a spectral resolution of 37 Hz (1000 video averaging cycles), and a pumping power of 26 mW.

to the photodetector). These spectra, together with the spectra of beats between the counterpropagating modes, confirm that single-mode bidirectional generation took place in both regimes.

Figure 3 shows plots of the amplitude of the signal of beats between counterpropagating modes of the laser cavity versus pumping power. Also presented in this figure is the plot of the total output power (equal to the sum of the output powers of the two opposite modes) versus the pumping power. All the curves in Fig. 3 are normalized to the values corresponding to a maximum pumping power. In the case when the laser generated a pair of complex-conjugate counterpropagating modes, the threshold pumping power for the signal of beats between these modes coincided with the lasing threshold. This coincidence is explained by the fact that modes with the complex-conjugate polarization states exhibit equal losses in the cavity, irrespective of the type of existing polarization-dependent losses. For this reason, the lasing thresholds for the counterpropagating modes are equal. On the contrary, once the laser generates the opposite modes with orthoconjugate polarization states, the losses of the counterpropagating modes are (in the general case) different in a cavity with polarization-dependent losses. Since the laser cavity always exhibits parasitic polarization-dependent losses, the lasing thresholds for the counterpropagating modes with orthoconjugate polarization states are different. Using this circumstance, it is possible to differentiate between the regime of bidirectional single-mode generation with complex-conjugate and orthoconjugate polarization states.

In one experiment, the laser was subjected to the action of an air flow inducing random fluctuations of birefringence of the laser cavity. The results of measurements using a scanning Fabry–Perot interferometer showed that the fluctuations of birefringence in the two regimes under consideration lead to a continuous variation of the frequencies of both modes, although jumps in the longitudinal mode frequencies sometimes also took place. However, the effect of fluctuating birefringence on the frequency difference between the counterpropagating modes depends on the generation regime. Figure 4 shows the RF spectra of beats between the opposite modes in the two regimes, corresponding to the generation of a pair of counterpropagating modes with complex-conjugate and orthoconjugate polarization states. The spectra were recorded in the regime of video averaging (each with 1000 averaging cycles). When the laser generated a pair of counterpropagating modes with orthoconjugate polarization states, the magnitude of fluctuations in the frequency of beats between these modes amounts to about 7 kHz. In the case of a pair of counterpropagating modes with complex-conjugate polarization states, analogous fluctuations of the cavity birefringence lead to fluctuations in the frequency of beats between these modes not exceeding 800 Hz. This result demonstrates a considerable decrease in sensitivity of the nonreciprocal fre-

quency shift between the opposite modes with respect to the laser cavity birefringence fluctuations. The spectrum presented in Fig. 4b shows weak side peaks shifted approximately by $\Delta\nu/2$, which are caused by uncertainty of the rotation angle of the 90° Faraday element. These peaks reflect the beats between the counterpropagating complex-conjugate modes and the adjacent longitudinal modes, the generation of which is strongly suppressed.

Conclusion. The results of experimental investigation of an Er-doped fiber bidirectional ring laser with a 90° Faraday rotator in the cavity are presented. Two generation regimes have been realized, corresponding to the single-mode bidirectional generation of modes propagating in opposite directions with either orthoconjugate or complex-conjugate polarization states. The latter regime provides for a strongly suppressed sensitivity of the nonreciprocal frequency shift between the opposite modes with respect to fluctuations in the laser cavity birefringence.

Acknowledgments. This study was supported by the Russian Foundation for Basic Research, project no. 00-02-16903.

REFERENCES

1. W. W. Chow, J. Gea-Banacloche, L. M. Pedrotti, *et al.*, Rev. Mod. Phys. **57**, 61 (1985).
2. E. Desurvire, *Erbium-Doped Fiber Amplifiers* (Wiley-Interscience, New York, 1994), pp. 225–244.
3. R. Kiyan, S. K. Kim, and B. Y. Kim, *Proceedings of the OFS-11, Sapporo, Japan, May 21–24, 1996*, Paper Th3-45, pp. 598–601.
4. R. Kiyan, S. K. Kim, and B. Y. Kim, IEEE Photonics Technol. Letters **8**, 1624 (1996).
5. R. V. Kiyan, A. A. Fotiadi, and O. V. Shakin, Pis'ma Zh. Tekh. Fiz. **29** (9), 24 (2003) [Tech. Phys. Lett. **29**, 364 (2003)].

Translated by P. Pozdeev

Technical Physics Letters, Vol. 29, No. 6, 2003, pp. 454–455. Translated from Pis'ma v Zhurnal Tekhnicheskoĭ Fiziki, Vol. 29, No. 11, 2003, pp. 30–34.

Mutual Diffusion at the Interface in a Two-Dimensional Ni–Al System

G. M. Poletaev and M. D. Starostenkov

Altai State Technical University, Barnaul, Russia

e-mail: genphys@agtu.secna.ru

Received January 31, 2003

Abstract—Mutual diffusion at the interface in a two-dimensional Ni–Al system has been studied by the method of molecular dynamics. It is established that the main diffusion mechanism consists in correlated jumps of atoms over the vacancies near misfit dislocation cores. *© 2003 MAIK "Nauka/Interperiodica".*

The results of numerous investigations indicate that an important (frequently, leading) role in the process of diffusion in metals belongs, in addition to the point defects, to some other structural defects such as dislocations, dislocation complexes, and grain boundaries [1–3]. However, the mechanisms of diffusion involving dislocations are still incompletely clear. Conducting the corresponding experiments, one encounters considerable difficulties, since the process dynamics has to be monitored on the atomic level. A promising way of solving this problem is offered by computer simulation methods.

We have studied the mechanism of mutual diffusion in metals by the method of molecular dynamics. The metal system was represented by the Ni–Al couple, which is primarily related to the high rate of the mutual diffusion in this system at elevated temperature. The diffusion process was modeled in a two-dimensional (2D) approximation. The interatomic interactions were described in terms of the central pairwise Morse potential with the parameters taken from [4]. The range of the potential action was restricted to 8 Å, which corresponds to the fourth coordination shell in a 2D crystal of aluminum and to the fifth shell in a nickel crystal at $T = 0$ K. The calculation cell in the numerical experiment contained about 3000 atoms. This amount is quite sufficient for studying the micromechanism of diffusion in the 2D system under consideration. Indeed, preliminary experiments showed that the influence of the cell boundaries on the process parameters is manifested only for cell dimensions on the order of 5–6 nm (20–25 interatomic distances).

The crystalline phases were assumed to possess a hexagonal package. The calculation cell had a rectangular shape and comprised crystalline phases of Ni and Al contacting along the interface. The boundary conditions were periodic in one axis, along the interface (representing an extended periodic defect), and flexible in the other axis, whereby the end atomic rows were allowed to shift as a whole. The flexible boundary conditions allowed the calculation cell to change volume in response to temperature and pressure variations. The starting structure was obtained by constructing the calculation cell configuration, simulating the primary dynamic relaxation until the kinetic energy stabilization, and ultrarapid cooling to a minimum temperature.

After dynamic relaxation of the calculation cell, the Ni–Al interface exhibited misfit dislocations oriented in two of the three close-packing directions. The formation of dislocation pairs is a characteristic feature of 2D hexagonal crystals. As a rule, each pair has a common core, which is energetically favorable. The pairwise character is related to the high order of axial symmetry: a shear in one of the close-packing directions leads to simultaneous displacement of two close-packed atomic rows forming an angle of 60°.

The experiments aimed at studying the mutual diffusion mechanism were conducted at temperatures close to the melting point of aluminum. The results of preliminary computer simulations showed that 2D aluminum in the model under consideration melts at ~1000 K.

An analysis of the atomic structure dynamics in the course of experiment showed that each diffusion event at temperatures below the melting point of aluminum consists predominantly of a combination of correlated jumps of vacancies near the misfit dislocation core, which result in an Al atom occupying the site previously occupied by a Ni atom (Fig. 1). In the course of thermal atomic oscillations, voids at the dislocation cores may behave like vacancies in the case of large displacements of adjacent atoms. At such moments, the probability that one of the adjacent atoms will occupy the previous vacant site increases. The jumps of atoms over the vacancies proceed predominantly along the close-packed rows, because such jumps require a relatively lower activation energy. The cyclic exchange mechanism involving vacancies (Fig. 1) may also proceed with participation of more than three atoms, but

1063-7850/03/2906-0454$24.00 © 2003 MAIK "Nauka/Interperiodica"

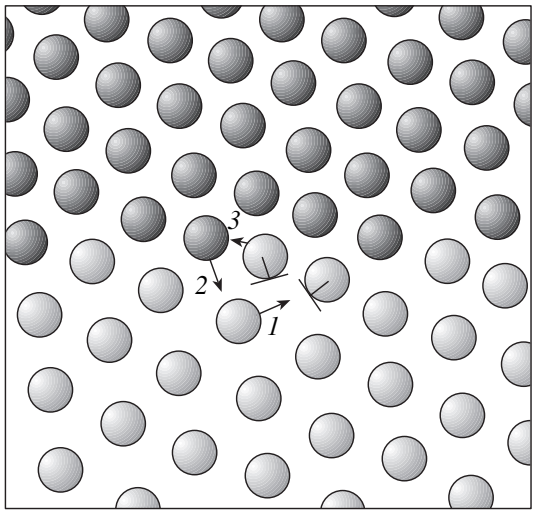

Fig. 1. A schematic diagram illustrating diffusion events at the interface in a two-dimensional Ni–Al system. Numbers indicate the possible sequence of atomic displacements (Ni and Al atoms are painted black and gray, respectively).

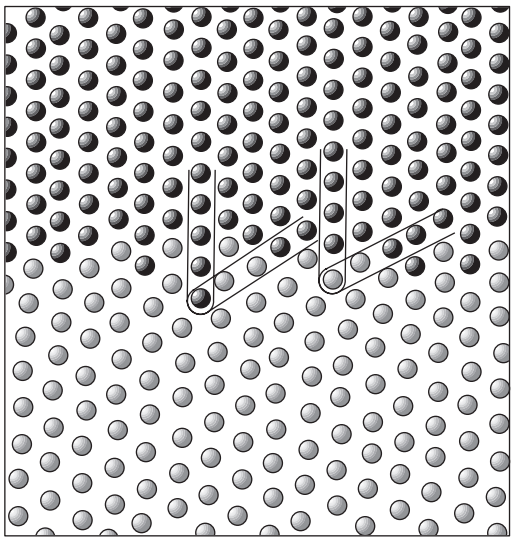

Fig. 2. A schematic diagram illustrating the free volume transfer inward the aluminum phase in the course of mutual diffusion. The free volume is transferred with misfit dislocations growing into aluminum. Lines indicate the broken atomic rows forming misfit dislocations.

the process is always activated near the local amorphization (violated crystal structure) regions.

The penetration of diffusing atoms into one or another component phase is related to the transfer of a free volume. In the case under consideration, the free volume is transferred toward aluminum (which is characterized by a higher plasticity). This is primarily determined by mismatch of the Ni–Al and Al–Al interatomic bonds, which gives rise to the lattice distortions. At the same time, misfit dislocations grow into the volume of aluminum (Fig. 2). Another factor accounting for the free volume transfer is polymorphism, which spreads inward more plastic material and leads to lattice distortions at the propagation front (representing essentially a grain boundary).

We have analyzed the influence of the mutual orientation of nickel and aluminum phases on the rate of mutual diffusion. It was established that the diffusion rate at the interface depends both on the density of misfit dislocations and on the orientation of Ni phase relative to the interface. The mutual diffusion at the interface was more intensive when the boundary Ni atoms have more Al neighbors. This factor may favor mobility of the boundary Ni atoms. Indeed, interfacial Ni atoms possessing a greater number of Al atoms in the environment probably to occur in a wider potential well.

Acknowledgments. This study was supported by the Russian Foundation for Basic Research, project no. 02-02-17875.

REFERENCES

1. B. S. Bokshteĭn, *Diffusion in Metals* (Metallurgiya, Moscow, 1978).
2. Ya. E. Geguzin, *Diffusion Zone* (Nauka, Moscow, 1979).
3. H. Gleiter and B. Chalmers, *High-Angle Grain Boundaries* (Pergamon, Oxford, 1972; Mir, Moscow, 1975).
4. A. I. Tsaregorodtsev, N. V. Gorlov, B. F. Dem'yanov, *et al.*, Fiz. Met. Metalloved. **58**, 336 (1984).

Translated by P. Pozdeev

Technical Physics Letters, Vol. 29, No. 6, 2003, pp. 456–458. Translated from Pis'ma v Zhurnal Tekhnicheskoĭ Fiziki, Vol. 29, No. 11, 2003, pp. 35–40.

Ion-Exchange Waveguides Formed in Glasses Using Silver-Containing Melts

A. A. Podvyaznyĭ and D. V. Svistunov

Vavilov Optical Institute, State Scientific Center of the Russian Federation, St. Petersburg, 190164 Russia

e-mail: svistunov@hotmail.com

Received November 6, 2002; in final form, January 31, 2003

Abstract—The activation energy has been determined and the concentration dependence of the diffusion coefficient have been studied for ion-exchange diffusion from silver-containing salt melts into K8 optical glass. The dependence of the refractive index at the surface of a gradient waveguide, formed by diffusion, on the melt composition is experimentally measured. Using these data, it is possible to model the optical parameters of the waveguides and to optimize the diffusion process parameters. © *2003 MAIK "Nauka/Interperiodica".*

Optical glasses are widely used for creating passive integral optical devices, in particular, passive elements of fiber optic systems and planar sensors monitoring various physical parameters. One of the main methods for the obtaining of waveguides in glasses is based on the ion exchange process conducted in melts containing silver salts, typically silver nitrate. This process is applicable to various optical glasses, including both commercial grades and special compositions, of which the most convenient is a commercial glass of the K8 grade. This glass contains a sufficient amount of alkaline components, which can serve as effusants during the ion exchange process. In addition, these glasses are readily available, possess sufficiently high chemical stability, and are well known from the standpoint of processing and obtaining high-quality surfaces.

The formation of optical waveguides (OWGs) in K8 glass by ion exchange with silver-containing melts was previously studied by many researchers (see, e.g., [1–4]). The resulting OWGs were characterized with respect to the mode spectra, refractive index profiles in the OWG cross section (restored from the mode spectra), optical losses, etc. At the same time, many questions concerning the kinetics of the waveguide layer formation remained unanswered. For example, the shape of the refractive index profiles in K8 is indicative of the concentration-dependent diffusion. At the same time, the problems pertaining to variation of this profile and the related mode composition in the course of diffusion were only qualitatively discussed. On this basis, it is impossible to select (a priori) technological regimes of ion exchange (temperature, diffusion time, salt bath composition) so as to obtain OWGs with required optical properties (propagation constants, mode penetration depth, surface refractive index).

Below, we report on the results of determination of the diffusion parameters which provide a basis for a priori modeling the refractive index profile in OWGs formed by ion exchange in silver-containing melts.

The values of the refractive index increments obtained by Ag^+–Na^+ exchange in K8 glass are proportional to the diffusant ion (Ag^+) concentration in the glass [4]. This fact allows us to use an approach developed in [5, 6], which is based on the interrelation between normalized profiles of the relative diffusant concentration (C/C_{max}) and the refractive index ($\Delta n/\Delta n_{max}$). According to [6], the ion exchange diffusion coefficient D can be presented in the following form:

$$D(T, C) = D_0 f(T) g(\Delta n),$$

where $f(T) = \exp[-H/(kT)]$, H is the diffusion activation energy, D_0 = const, and $g(\Delta n)$ is a factor accounting for the concentration dependence of the diffusion coefficient. The form of the $g(\Delta n)$ function is determined by applying the Boltzmann method to a refractive index profile restored by a standard calculation procedure [7] from experimental data on the waveguide mode propagation constants. The procedure of application of the Boltzmann method is described, for example, in [5, 8]. Note that the diffusant concentration in the Boltzmann formula also has to be replaced by Δn.

We have manufactured OWGs by treating K8 glass in a KNO_3–$NaNO_3$ eutectic melt with $AgNO_3$ added to a concentration of 5 mol %. The ion exchange time was varied from 20 to 70 h, and the process temperature, from 260 to 350°C.

1063-7850/03/2906-0456$24.00 © 2003 MAIK "Nauka/Interperiodica"

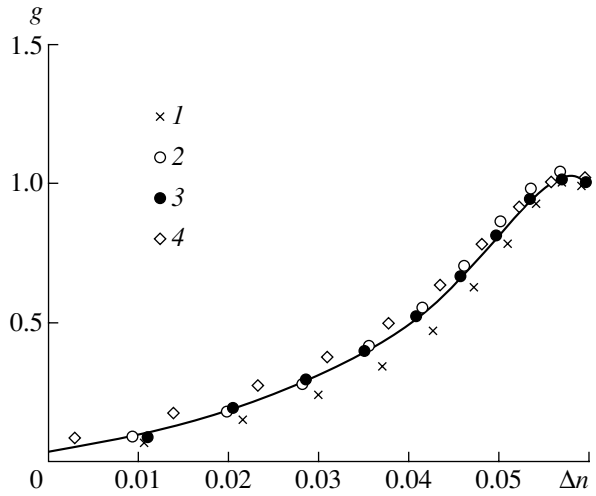

Fig. 1. Concentration-dependent component of the diffusion coefficient for the Ag^+–Na^+ ion exchange process in K8 glass; diffusion temperature, T = 263 (*1*), 300 (*2*), 329 (*3*), and 351°C (*4*); diffusion time, t = 66 (*1*), 67.5 (*2*), 40.5 (*3*), and 20 h (*4*).

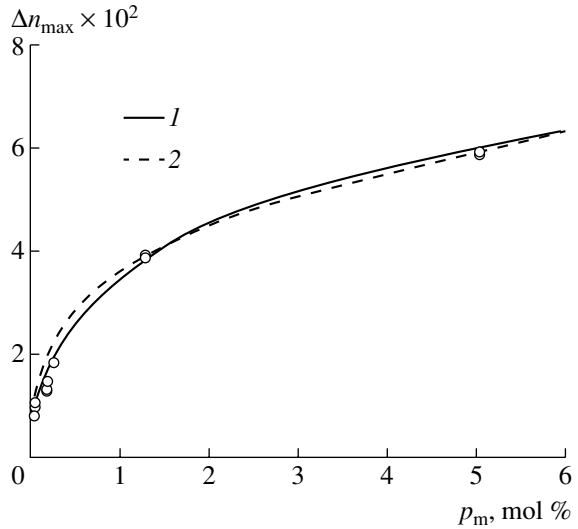

Fig. 2. Plots of the maximum refractive index increment in K8 glass versus silver nitrate content in the melt: open circles represent experimental data from [10]; curves *1* and *2* show the logarithmic and cubic approximation, respectively.

Figure 1 shows the plot of $g(\Delta n)$ constructed by data for several OWG samples. As can be seen, the experimental points fit the same curve, which can be approximated by the polynomial

$$g(\Delta n) = a_0 + a_1\Delta n + a_2(\Delta n)^2 + a_3(\Delta n)^3 + a_4(\Delta n)^4 + a_5(\Delta n)^5 + a_6(\Delta n)^6 + a_7(\Delta n)^7,$$

where $a_0 = 0.03$, $a_1 = 6.036$, $a_2 = 51.642$, $a_3 = -1.247 \times 10^4$, $a_4 = 1.811 \times 10^6$, $a_5 = -8.214 \times 10^7$, $a_6 = 1.585 \times 10^9$, and $a_7 = -1.087 \times 10^{10}$. Applying the standard calculation procedure to the values of the diffusion coefficient at T = 263, 300, 329, and 351°C, we obtain $H = 1.67 \times 10^{-19}$ J and $D_0 = 7.87 \times 10^{-3}$ cm^2/s.

As was proposed in [6], the refractive index profile obtained by ion exchange can be a priori modeled by solving an equation analogous to the diffusion equation:

$$\partial(\Delta n)/\partial t = \mathrm{div}[D(\Delta n)\mathrm{grad}(\Delta n)].$$

According to [9], the refractive index profile at the OWG surface is established in the course of Ag_m^+–Na_g^+ ion exchange (Ag_m^+ and Na_g^+ denoting ions in the melt and glass, respectively) during a period of time on the order of several tens of seconds and then remains virtually unchanged. At the same time, the time required for the formation of OWGs with required parameters amounts to tens of minutes. Therefore, in solving the above equation, the boundary condition can be formulated by setting a maximum refractive index increment at the waveguide surface, Δn_{max}, which can be achieved for a given salt bath composition.

In order to estimate a priori the Δn_{max} value, we used supplemented experimental data [10] concerning the dependence of the refractive index increment on the silver nitrate content. Presented in Fig. 2, this supplemented dependence can be described by the expression

$$\Delta n_{max} \times 10^2 = 1.8\ln(p_m + 0.3) + 3,$$

where p_m is the content of silver nitrate in the melt expressed in mol %, or alternatively as

$$\Delta n_{max} \times 10^2 = 1.8\ln(p_w + 0.4) + 2,$$

where p_w is the content of silver nitrate in the melt expressed in wt %. A rough estimate is provided by a simpler cubic formula:

$$\Delta n_{max} \approx 3.5 \times 10^{-2}(p_m)^{1/3}.$$

As can be seen from Fig. 2, the experimental data fit the proposed approximating functions well.

Using the above results, it is possible to model the process of OWG formation in K8 glass by ion exchange and predict the refractive index profile depending on the technological regime employed. This allows the process conditions to be a priori optimized so as to obtain OWGs with parameters close to required values.

Acknowledgments. The authors are grateful to D.K. Tagantsev for the fruitful discussion of data.

REFERENCES

1. Yu. S. Kuz'minov, N. M. Lyndin, A. M. Prokhorov, *et al.*, Kvantovaya Élektron. (Moscow) **2**, 2309 (1975).
2. G. T. Petrovskiĭ, K. A. Agafonova, A. V. Mishin, and N. V. Nikonorov, Fiz. Khim. Stekla **7**, 98 (1981).
3. A. V. Tomov, Pis'ma Zh. Tekh. Fiz. **17** (14), 60 (1991) [Sov. Tech. Phys. Lett. **17**, 517 (1991)].
4. K. A. Landa and G. T. Petrovskiĭ, *Amorphous Planar Waveguides* (Krasnoyarsk. Univ., Krasnoyarsk, 1987).
5. K. K. Evstrop'ev, *Diffusion Processes in Glasses* (Stroĭizdat, Leningrad, 1970).
6. G. O. Karapetyan, V. V. Zhurikhina, A. A. Lipovskiĭ, *et al.*, Fiz. Khim. Stekla **26**, 179 (2000).
7. K. S. Chiang, J. Lightwave Technol. **3**, 385 (1985).
8. R. Sh. Malkovich, *Mathematics of Diffusion in Semiconductors* (Nauka, St. Petersburg, 1999).
9. N. M. Lyndin, D. Kh. Nurligareev, V. A. Sychugov, and A. V. Tishchenko, Kvantovaya Élektron. (Moscow) **19**, 379 (1992).
10. A. A. Vetrov, V. B. Volkonskiĭ, and D. V. Svistunov, Opt. Zh. **66** (5), 57 (1999) [J. Opt. Technol. **66** (5), 428 (1999)].

Translated by P. Pozdeev

Technical Physics Letters, Vol. 29, No. 6, 2003, pp. 459–460. Translated from Pis'ma v Zhurnal Tekhnicheskoĭ Fiziki, Vol. 29, No. 11, 2003, pp. 41–44.

Peculiarities of the Current–Voltage Characteristics of Oxidized Porous Silicon

M. S. Ablova, M. V. Zamoryanskaya, V. I. Sokolov, and R. I. Khasanov

Ioffe Physicotechnical Institute, Russian Academy of Sciences, St. Petersburg, 194021 Russia

Received December 15, 2002; in final form, January 24, 2003

Abstract—Oxidized porous silicon is a nanocomposite material. The current–voltage characteristics of MOS structures based on this material exhibit some special features (large plateau, oscillations), which can be considered as manifestations of quantum size effects. © *2003 MAIK "Nauka/Interperiodica".*

Metal–oxide–semiconductor (MOS) structures in which the oxide layer is formed by oxidizing single crystal silicon substrate are the basis of modern microelectronics. However, analogous structures based on oxidized porous silicon remain virtually unstudied. Considering this oxide as a nanocomposite material, we may expect that MOS structures based on this substrate will exhibit certain quantum size effects. This study aimed at searching for such effects.

The samples were prepared from (100)-oriented *p*-type silicon single crystal (c-Si) plates of KDB-10 grade. The porous oxide film containing silicon nanoclusters was formed using the following procedure. A c-Si plate was electrochemically etched in an aqueous solution of hydrofluoric acid (30% HF) for 5 min at a current density of 10 mA/cm^2, which resulted in a porous silicon (por-Si) layer formation. A part of the plate remained unetched to serve as a control region in subsequent measurements. After etching, the material was oxidized by exposure to water vapor at 1000°C for 20 min. The oxide film thickness in the control (c-Si) region was 190 nm, while that on por-Si was 300 nm. The conditions of oxidation were specially selected so that the entire por-Si layer would be oxidized together with some part of the underlying single crystal substrate material.

For comparison, we have also studied analogous samples prepared elsewhere, in which transmission electron microscopy indicated the presence of silicon nanoclusters (nc-Si). The presence of such nanoclusters in our samples was detected indirectly, by measuring their cathodoluminescence (CL) spectra. As is known [1, 2], the appearance of a green emission line in the CL spectrum is evidence of the presence of nc-Si (approximately 5 nm in size) in silicon oxide. Since the current–voltage characteristics of MOS structures based on samples of both types coincided as well, we took this as sufficient evidence of the presence of silicon nanograins in our samples.

The current–voltage (*J–U*) characteristics of MOS structures were measured in the dark, in a dynamic regime using a sinusoidal probing signal at a frequency of 20 or 400 Hz. The measurements were performed under standard conditions in a vacuum chamber, which eliminated the influence of adsorption. In order to expand the range of conditions studied, the *J–U* curves were measured at two significantly different temperatures, 300 and 77 K (the quantum size effects are most probably manifested at lower temperatures).

The current–voltage characteristics of all samples with oxidized porous films (Figs. 1 and 2) exhibited the following common features (for the convenience of analysis and comparison with other published data, the *J–U* curves are plotted on a linear scale):

(i) irrespective of the frequency and temperature, all *J–U* curves are nonlinear, which is evidence of the diode effect;

(ii) in all *J–U* curves, the current through the structure at a zero bias voltage has a finite nonzero value;

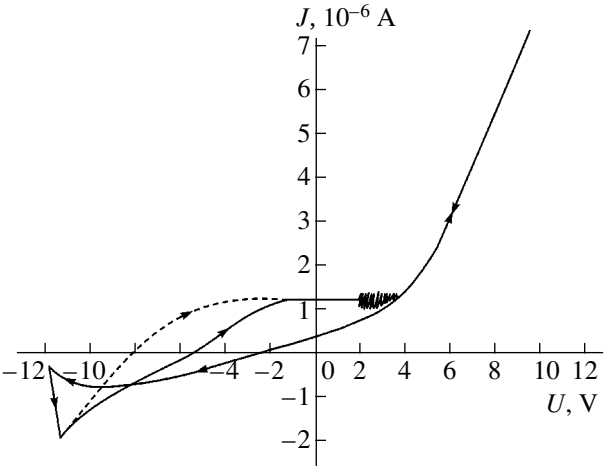

Fig. 1. A room temperature current–voltage characteristic of sample no. 4 measured at 20 Hz (amplitude, 12 V), showing oscillations on the plateau at a positive polarity of c-Si substrate. Dashed curve shows the plateau extended upon the "field treatment."

1063-7850/03/2906-0459$24.00 © 2003 MAIK "Nauka/Interperiodica"

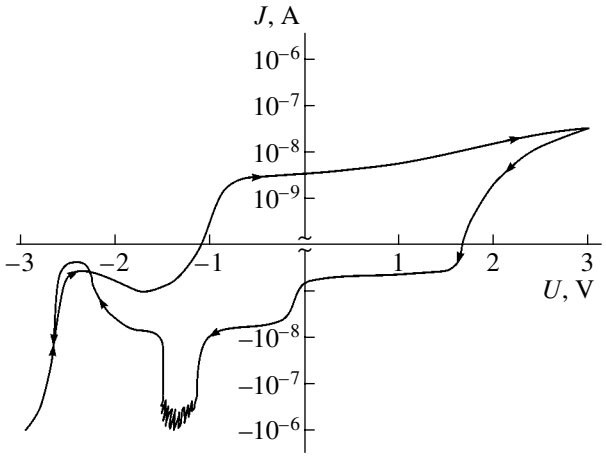

Fig. 2. A low-temperature (77 K) current–voltage characteristic of sample no. 1 (kept for two months in a vacuum chamber) measured at 20 Hz (amplitude, 3 V), showing oscillations on the plateau at a negative polarity of c-Si substrate. No such oscillations were observed for this sample at 300 K and before keeping in vacuum.

(iii) the *J–U* curves of all samples exhibit hysteresis.

At the same time, the control samples exhibited neither diode properties nor a finite zero-bias current and hysteresis. The hysteresis behavior, as well as a plateau on the *J–U* curves (Fig. 1) seem to reflect the accumulation of charge at the oxide–semiconductor interface in biased samples with minus on c-Si, which is due to nc-Si grains possessing the properties of slow traps. The charge carrier trapping is determined by the amplitude of the measuring signal, which is confirmed by the fact that a short (12 s) "field treatment" (whereby a higher bias voltage amplitude 40 V instead of the initial 12 V, is used during this period) leads to extension of the plateau on the *J–U* curve (as indicated by the dashed curve in Fig. 1).

Another important feature of the *J–U* curves of the samples studied is the presence of a packet of high-frequency oscillations on one of the branches. The amplitude of these oscillations with respect to current probably reflects some internal properties of the MOS structure, which is differently modified during the "field treatment" and during measurement at various frequencies of the measuring signal. Figures 1 and 2 show current oscillations of different types observed on the *J–U* curves. Figure 1 illustrates the oscillations appearing on the plateau in the region of positive bias (plus on c-Si) for sample no. 4. Most of the samples studied showed *J–U* curves close to that presented in Fig. 1.

Figure 2 presents a *J–U* curve of another kind, which may be called "atypical." This curve was obtained at liquid nitrogen temperature for a sample kept for two months in a vacuum chamber (sample no. 1). Here, the oscillations are observed on the branch corresponding to minus on c-Si. As can be seen, the level of currents measured in this case dropped sharply as compared to that at 300 K and revealed oscillations not detected at room temperature. The amplitude of oscillations in Figs. 1 and 2 is virtually the same. In all cases, the oscillations were observed only at 20 Hz and disappeared at 400 Hz. It should be emphasized that an increase in the frequency, as well as exposure to white light, eliminated the fine structure of the current–voltage characteristics.

The observed peculiarities of the current–voltage characteristics are probably indicative of the presence of shallow quantum wells in MOS structures based on oxidized porous silicon. These quantum wells are structurally related to the aforementioned slow traps. This is evidenced by the result presented in Fig. 1, where the current oscillations are observed immediately on the plateau. More detailed investigation of these features is now in progress.

REFERENCES

1. V. N. Bogomolov, S. A. Gurevich, M. V. Zamoryanskaya, *et al.*, Fiz. Tverd. Tela (St. Petersburg) **43**, 357 (2001) [Phys. Solid State **43**, 373 (2001)].
2. V. G. Baru, M. I. Elinson, V. A. Zhitov, *et al.*, Mikroélektronika **27** (1), 45 (1998).

Translated by P. Pozdeev

Technical Physics Letters, Vol. 29, No. 6, 2003, pp. 461–463. Translated from Pis'ma v Zhurnal Tekhnicheskoĭ Fiziki, Vol. 29, No. 11, 2003, pp. 45–50.

Nonexponential Current Relaxation on a Solid Surface

V. I. Batkin and O. Ya. Savchenko

Institute of Solid State Chemistry and Mechanochemistry, Siberian Division, Russian Academy of Sciences, Novosibirsk, Russia

Institute of Chemical Kinetics and Combustion, Siberian Division, Russian Academy of Sciences, Novosibirsk, Russia

e-mail: Batkin@solid.nsc.ru

Received November 18, 2002; in final form, January 10, 2003

Abstract—Experimental data on the relaxation of currents due to ion emission, charge leak from a dielectric surface, and polarization of electrodes in various electrolytes are reported. It is shown that the same nonexponential law of the current relaxation, $I(t) \sim \exp(-\alpha\sqrt{t})$, is applicable in all these cases. A common mechanism of these phenomena is discussed. © *2003 MAIK "Nauka/Interperiodica".*

Many relaxation processes in condensed media obey a nonexponential law of the type $\sim\exp(-\alpha t^p)$. Originally, such a relaxation was observed about one and a half centuries ago by Cohlrausch [1]. Despite a large body of experimental data and extensive theoretical investigation, there is still no commonly accepted opinion about the factors leading to time dependences of the above type. Below, we will demonstrate that the surface phenomena of three classes, including ion emission, charge leak on a dielectric surface, and electrode polarization in the course of low-current electrolysis, are also characterized by nonexponential relaxation behavior.

Previously [2], we studied the process of ion emission from heated metal wires and established that the emission current exhibits a regular but nonexponential relaxation. From an initial level above 1 μA/cm^2, the current dropped according to the law

$$I = A\exp(-\alpha\sqrt{t}) + B/\sqrt{t}. \quad (1)$$

This behavior was observed especially clearly, without any spurious current pulses, provided that the emitter was preliminarily annealed in vacuum and activated by treating with distilled water. The exponent with a fractional power of t entering into formula (1) is a particular case of the Cohlrausch function $\sim\exp(-\alpha t^p)$ [1, 3], which is widely used in the physics of noncrystalline materials. The ion emission proved to be a rather complicated phenomenon. To better understand this phenomenon, it would be helpful to study analogous but more controllable surface processes. This possibility is offered by observations of low-current electrolysis and leak currents on a dielectric surface.

The experiments with electrolysis were performed as follows. Two electrodes placed in electrolyte were connected to an external circuit comprising a resistor (R = 50 MΩ), an emf source, and a current meter. A special feature of this scheme is the large R value. The emf (200 V) was switched on for 3 s, after which a discharge current was monitored. Typical current oscillograms are presented in Fig. 1. The process was studied in various electrolytes, including dimethyl sulfoxide (points *2*), 0.5 M aqueous NaCl solution (*3*), and ethanol (*4*). The anode was made of gold and the cathode, of a doped *n*-type silicon. For comparison, points *1a* and *1b* in Fig. 1 show the kinetics of a different process representing K^+ ion emission from a heated nichrome

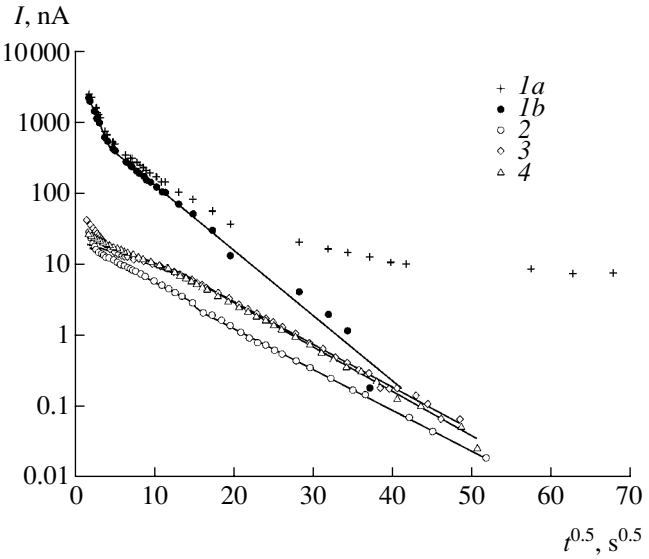

Fig. 1. The kinetics of K^+ ion emission from a nichrome wire (*1a*, ×10) and the current (measured in a 50 MΩ resistor) between preliminarily polarized Au and Si electrodes in dimethyl sulfoxide (points *2*), 0.5 M aqueous NaCl solution (*3*), and ethanol (*4*). Points *1b* are obtained from *1a* by subtracting the value of $10B\sqrt{t}$ as in formula (1). Line segments represent the plots of $\sim\exp(-\alpha\sqrt{t})$.

1063-7850/03/2906-0461$24.00

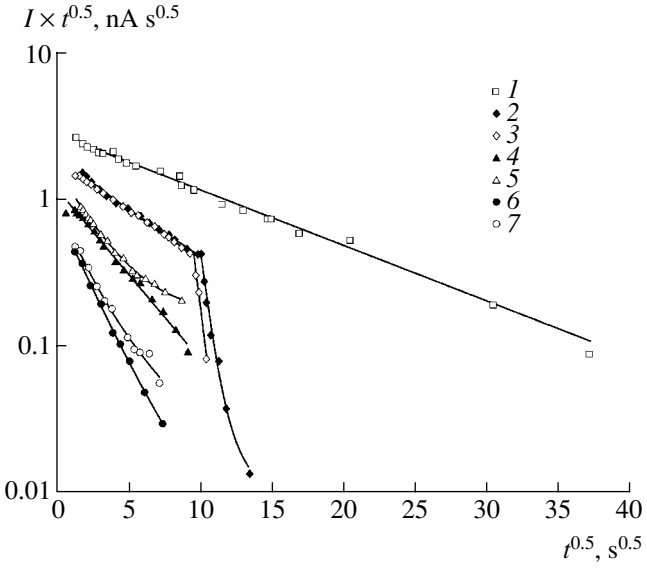

Fig. 2. The kinetics of charge leakage from glass surface in air (*2*, *4*, *6*) and in squalane (*1*, *3*, *5*, *7*). The ordinate is $I\sqrt{t}$, where I is the current and t is the time measured after emf switch off (points *1–7* correspond to the emf switched on for 206, 29, 25.5, 7, 7.1, 2.6, and 2.8 s, respectively). Line segments represent the plots of $A\exp(-\alpha\sqrt{t}) + B$.

wire (points *1a* show the total emission current and points *1b* are obtained by subtracting the $B/\sqrt{t}$ value as in formula (1)).

The approximating curves are constructed so that the function $A\exp(-\alpha\sqrt{t})$ is represented by a straight line. The approximation of $I(t)$ by segments of such lines implies that the A and α values change in a jumplike manner. The change is so sharp that the bending cannot be excluded by using the Cohlrausch function with $p \approx 0.5$. The parameters of approximation in various $I(t)$ regions differently depend on the experimental conditions. The emf amplitude was selected so as to correspond to saturation of the effect with respect to the amplitude. This region begins at an amplitude of ≈20 V, for which the charge transferred in the circuit during the current pulse is close to the charge of residual current and is on the order of a charge corresponding to a monolayer electrode coverage. In the experiments under consideration, the Au electrode area was much smaller than that of the Si electrode. Replacing the large Si electrode with a metal electrode did not change the behavior of $I(t)$, while the changing the small electrode material significantly modified this function.

The experiments with the current relaxation on a dielectric surface differed from the case of electrolysis in that, instead of an electrolyte, the medium connecting the electrodes was the dielectric surface. Two ring electrodes were put on a rod made of some dielectric material (ceramics, teflon, or glass). The electrodes were connected for some time t_a to a voltage source (290 V) inducing a leak current on the rod surface. Then the source was disconnected, the electrodes were shorted by a conductor, and the decaying relaxation current in this conductor was monitored.

Figure 2 shows typical diagrams of the leak current measured for a glass rod. The ordinate represents the values of current multiplied by $\sqrt{t}$. As a result, the experimental points fit straight lines, which implies that the behavior of $I(t)$ is well described by the function

$$I(t) \sim \exp(-\alpha\sqrt{t})/\sqrt{t}, \qquad (2)$$

representing a derivative of the function $I(t) \sim \exp(-\alpha\sqrt{t})$. The glass rod occurred in air (points *2*, *4*, *6*) or in squalane $C_{30}H_{62}$ (points *1*, *3*, *5*, *7*). The approximating lines correspond to the functions $I = A\exp(-\alpha\sqrt{t}) + B$. The experiments presented in Fig. 2 were performed with glass of the 3S-5 grade and the electrodes spaced by 2.5 mm.

The form of the approximating function (2) suggests that a process in the insulated regions (probably near the electrodes) is generally the same as that during the electrolysis, but the capacitive coupling between these regions results in $I = C\frac{dU}{dt}$, where C is the capacitance and U is the polarization voltage. For $U = 1$ V and a sufficiently large t_a, the capacitance must reach 64 nF. This value is significantly greater than geometric estimates and is evidence of a high polarization of the dielectric surface. Replacing air by squalane changed the $I(t)$ curve rather slightly, despite a significant change in the layer of adsorbate on the glass surface. When the glass rod was removed and the electrodes were allowed to hang freely, no current between electrodes was observed in squalane (or in other anhydrous hydrocarbons). The results of experiments with other dielectrics were similar to those described above.

Thus, the processes of relaxation of the ion emission current, the charge leakage from a dielectric surface, and the discharge current of electrodes polarized in various electrolytes are described by time functions of close shapes. Not only are the analytical expressions close, but the jumplike changes in the parameters of these functions are similar as well. Among the phenomena described above, the most thoroughly studied is electrolysis. The laws of electrochemical processes have been calculated and the results of such calculations are successfully used in analytical chemistry [4, 5]. Unfortunately, the problem of specific current relaxation according to the law $\sim\exp(-\alpha\sqrt{t})$ has never been considered in this field. Phenomena involved in the polarization of dielectrics are closer to our observations. In this field, the nonexponential (non-Debye) relaxation of polarization in condensed media has been known for a long time [6], but this process takes place in low-molecular-weight media and is many orders of

magnitude faster than the relaxation observed in our case.

A special feature of our experiments is the very small magnitude of currents. Upon going from discharge currents $I \approx 1$ nA to the case of $I \approx 1$ mA by decreasing the discharge resistance R, the anomalous time dependence $I(t) = I_0\exp(-\sqrt{t/RC})$ changes to the normal behavior $\approx I_0\exp(-t/RC)$, where C is the effective capacitance. Small currents at a large charge carrier density on the surface can probably lead to limitation of the transport of ions, provided that their motion has a cooperative character. These conditions are typical of diffusion in glassy materials. Described by the Cohlrausch function $\sim\exp(-\alpha t^p)$, the relaxation in glasses [3] appears to be similar to the phenomena observed in our experiments.

The experiments with electrolysis involve two controllable parameters, namely, the current and the potential drop near electrodes. Therefore, by changing the effective electric field, it is possible to pass from the state of independent ion motion to the state of correlated motions. Such a transition from an ergodic to nonergodic state takes place with decreasing temperature in glassy materials. Apparently, the emission of impurity ions and the leak currents on the surface of dielectrics are based on the same mechanism of charge carrier transport as that in the case of low-current electrolysis.

The results of our experiments provide for a new standpoint in the basic problem of the kinetics of processes in condensed media and probably outline new ways to elucidating the nature of these processes.

Acknowledgments. This study was supported by the Russian Foundation for Basic Research, project no. 01-02-17535.

REFERENCES

1. R. Kohlrausch, Prog. Ann. Phys. **91**, 179 (1954).
2. V. I. Batkin and O. Ya. Savchenko, Zh. Tekh. Fiz. **72** (5), 91 (2002) [Tech. Phys. **47**, 604 (2002)].
3. *Disorder Effects on Relaxation Processes*, Ed. by R. Richert and A. Blumen (Springer-Verlag, Berlin, 1994).
4. R. R. Salem, *Theoretical Electrochemistry* (Vuz. Kniga, Moscow, 2001).
5. B. B. Damaskin and V. A. Safonov, Electrochim. Acta **42**, 737 (1997).
6. A. K. Jouscher, *Dielectric Relaxation in Solids* (Chelsea, London, 1983).

Translated by P. Pozdeev

Technical Physics Letters, Vol. 29, No. 6, 2003, pp. 464–466. Translated from Pis'ma v Zhurnal Tekhnicheskoĭ Fiziki, Vol. 29, No. 11, 2003, pp. 51–55.

Nonequilibrium Nonstoichiometry in Ionic Compounds

V. N. Gurin*, M. M. Korsukova, S. P. Nikanorov, A. P. Nechitaĭlov, L. I. Derkachenko, Z. I. Uspenskaya, and I. N. Zimkin

Ioffe Physicotechnical Institute, Russian Academy of Sciences, St. Petersburg, 194021 Russia

** e-mail: vladimir.gurin@mail.ioffe.ru*

Received December 29, 2002

Abstract—Ionic substances under normal conditions are stoichiometric compounds with phase diagrams featuring no homogeneity regions. Crystals grown under nonequilibrium conditions, in particular, under significant centrifugal acceleration, are characterized by nonstoichiometric compositions (e.g., $K_{1-x}Br_{1.07}$). In this way, it is possible to obtain nonequilibrium nonstoichiometric ionic compounds possessing certain homogeneity regions. Nonstoichiometric crystals of KCl, KBr, and KI grown under various accelerations ranging within $(1.3–100.0) \times 10^3 g$ exhibit insignificant variations in the lattice constants and a significant increase in microhardness with acceleration. © *2003 MAIK "Nauka/Interperiodica".*

The problem of nonstoichiometry in chemical compounds has been studied for a long time [1, 2]. Most of these investigations were devoted to so-called equilibrium stoichiometry, whereby the experiments are performed so as to establish the presence or absence of a homogeneity region for a given compound grown under equilibrium conditions. Once such a region does exist, its shape is determined under conditions of variable temperature. The arrangement of various types of the homogeneity regions with respect to the stoichiometry line in the temperature interval of the existence of such regions has been classified [3].

Under nonequilibrium conditions, such as ultrahigh pressures, ultrarapid cooling, and centrifuging, it is possible to obtain nonstoichiometric compounds possessing nonequilibrium homogeneity regions [4, 5].

We have grown nonequilibrium crystals of KCl, KBr, and KI under conditions of centrifuging at (1.3, 6.2, 11.8, and 15.0) $\times 10^3 g$ in a K24D centrifuge (arm length, 70 mm) and at $100 \times 10^3 g$ in a Hitachi preparative ultracentrifuge (model, CP80β; rotor, P70AT2; arm length, 82.5 mm). The samples were grown for 30 min by crystallization from supersaturated aqueous solutions cooled from +80 to –10°C. The crystals were studied by gravimetry, titrimetry, flame spectrometry, and spectrophotometry according to standard procedures. In a special case of determining K and I in small amounts of crystallized substance, we employed inductively coupled plasma (ICP) optical emission spectrometry. The lattice periods of sample crystals were determined by X-ray diffraction measurements performed on a DRON-2 diffractometer. The microhardness was measured on a PMT-3 device under various loads (P) on the indenter.

The as-grown crystalline deposits were dried in a thermal box at 90–100°C and then characterized with respect to chemical composition, crystallographic parameters, microhardness, etc. The results of chemical analyses and microhardness measurements are presented in the table.

According to the experimental data, the chemical composition of crystals grown in a centrifuge always differed, albeit slightly, from that obtained under normal gravity conditions. However, even this small change led to a very significant change in microhardness (which drastically increased with the acceleration). This is evidence of the considerable influence of the centrifuging on the properties of solid crystal deposits.

Representing the results of chemical analyses (virtually always indicative of the lack of stoichiometry in the centrifuged samples) in the form of a homogeneity region of a given compound on the temperature versus composition plane, we obtain a left- or right-hand region within a relatively narrow temperature interval. This interval is determined by conditions corresponding to the onset and termination of the solid crystal formation in a supersaturated aqueous solution in the course of centrifuging. A schematic diagram showing such homogeneity regions for nonstoichiometric KCl and KBr crystals is depicted in the figure. Of course, these regions are nonequilibrium and, to a certain extent, conditional and approximate. This is related to many factors, primarily to the need in obtaining statistically reliable (stable) data on the composition of centrifuged samples. Such data are obtained under strictly determined experimental conditions (special centrifuge regimes; the certain type, form, and composition of the initial compound; the same procedure of extracting from tubes and subsequent treatments; the accuracy of chemical analyses, etc.).

1063-7850/03/2906-0464$24.00 © 2003 MAIK "Nauka/Interperiodica"

As can be seen from the experimental data obtained in this study (see table), the results of chemical analyses of the crystalline powders obtained in a centrifuge sometimes differ from what could be reasonably anticipated. This discrepancy can be related to the conditions of experiments with centrifuges, whereby preheated aqueous solutions were balanced for a relatively long time, closed with stoppers, and placed in a rotor, after which the centrifuge was accelerated to a preset rotation speed. This period of time was sufficient for a deposit to form in some tubes, whose composition remained unchanged in the course of the subsequent growth. Thus, the sample extracted from the centrifuge after the growth cycle represented a mixture of crystalline powders formed before and in the course of centrifuging, which was reflected by the results of chemical analyses. This circumstance was confirmed by the data on microhardness: the samples of some compounds (e.g., KI and $Ba(NO_3)_2$) grown under the conditions of ultracentrifuging exhibited significantly different H_K values, which was evidence of the presence of crystals of two types, formed before and in the course of centrifuging. Since these crystals are practically indistinguishable, this circumstance unavoidably leads to uncertainties in the chemical analysis and to a scatter in the values of microhardness. This difficulty can probably be eliminated by centrifuging solutions with a lower degree of supersaturation, but this requires additional investigations.

In concluding, it should be emphasized that we have employed for the first time the ultracentrifuging of supersaturated aqueous solutions of ionic compounds. We also suggest for the first time to consider the formation of a nonstoichiometric composition of crystals in a centrifuge as the phenomenon of nonequilibrium nonstoichiometry or as the existence of a nonequilibrium homogeneity region for such ionic compounds. As is well known, under normal conditions these compounds always possess strictly stoichiometric compositions and exhibit no homogeneity regions.

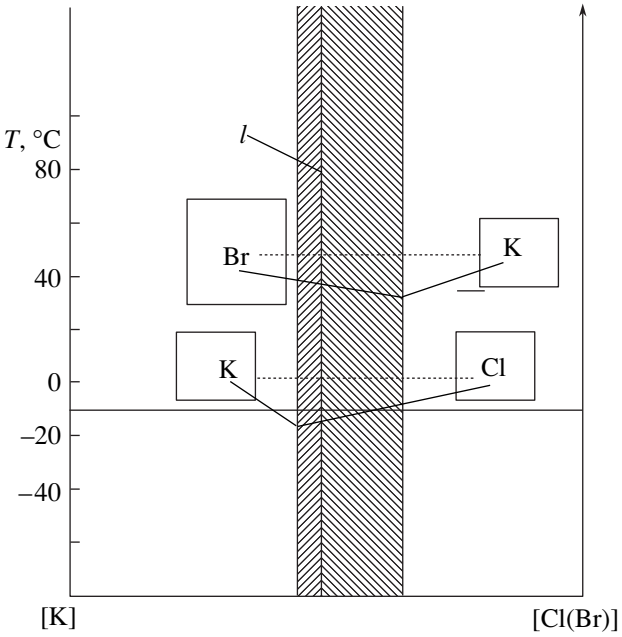

The schematic diagram of nonequilibrium homogeneity regions (l is the stoichiometry line) of potassium halides ($K_{1+x}Cl_{0.96}$; $K_{1-x}Br_{1.07}$) deposited from supersaturated aqueous solutions in a centrifuge (the contents of chlorine and bromine in atomic fractions, as determined by chemical analyses corresponds to formulas in the table; in the figure, [K] and [Cl(Br)] are given in at. %). In the lack of some component in a compound (e.g., K in KBr or Cl in KCl) against stoichiometry, the boundary of the nonequilibrium homogeneity region with shift away from the stoichiometry line with respect to the ordinate of the given component (K or Cl(Br)), while in the excess of a component (Br in KBr or K in KCl), the boundary is closer to this line (for Cl(Br) or K). Temperature limits are indicated conditionally.

Compositions of initial and centrifuged compounds and microhardness of the crystals grown in a centrifuge

Compound	Centrifugal acceleration, g					
	0	1.3×10^3	6.2×10^3	11.8×10^3	15.0×10^3*	100×10^3*
KCl; [K], mass %	52.4	52.0	<u>56.8 (43.2)</u>	51.8	–	48.8
H_K, MPa	172	182	214	219	–	–
KBr; [K], mass %	32.7	33.1	<u>28.2 (71.8)</u>	32.8	–	34.1
H_K, MPa	123	176	266	297	–	345
KI; [K], mass %	25.1	25.0	24.6	25.1	24.9	24.3
H_K, MPa	–	100	109	133	235; 115	136
$Ba(NO_3)_2$; [Ba], mass %	51.5	52.1	52.4	52.5	–	52.7
H_K, MPa	703	867	1016	1255		1369; 1266

* Data of this study; compositions (mass %) are taken from [6]; indenter load P = 19.62 mN (for $Ba(NO_3)_2$) and 98.1 mN (all other compounds); accuracy of microhardness measurements, 5–7%; underlined data correspond to the homogeneity regions presented in the figure.

Acknowledgments. The authors are grateful to Ulrique Schmidt (Max Planck Institute of the Chemical Physics of Solid State, Dresden, Germany) for conducting chemical analyses and to Yu.G. Nosov and Yu.M. Chernov for their help in work.

This study was supported by the Russian Foundation for Basic Research, project no. 01-03-32822.

REFERENCES

1. R. Collongues, *La Non-stoechiometrie* (Masson, Paris, 1971; Mir, Moscow, 1974).
2. *Problems of Nonstoichiometry*, Ed. by A. Rabenau (North Holland, Amsterdam, 1970; Metallurgiya, Moscow, 1975).
3. V. N. Gurin, M. M. Korsukova, E. V. Kalashnikov, and S. P. Nikanorov, Fiz. Tverd. Tela (St. Petersburg) **26**, 1091 (1984) [Sov. Phys. Solid State **26**, 663 (1984)].
4. V. N. Gurin, Z. Anorg. Allg. Chem. **628**, 2182 (2002).
5. V. Gurin, M. Korsukova, S. Nikanorov, *et al.*, *Progr. Abstr. 14th Int. Symp. "Boron, Borides, and Related Compounds," St. Petersburg, June 9–14, 2002*, p. 31.
6. V. N. Gurin, S. P. Nikanorov, A. P. Nechitaĭlov, *et al.*, Fiz. Tverd. Tela (St. Petersburg) **43**, 1196 (2001) [Phys. Solid State **43**, 1241 (2001)].

Translated by P. Pozdeev

Technical Physics Letters, Vol. 29, No. 6, 2003, pp. 467–470. Translated from Pis'ma v Zhurnal Tekhnicheskoĭ Fiziki, Vol. 29, No. 11, 2003, pp. 56–64.

Signal Amplification in a Gyro-Backward-Wave Tube

A. E. Khramov

Saratov State University, Saratov, Russia
State Scientific Center "College", Saratov, Russia
e-mail: ach@cas.ssu.runnet.ru

Received November 25, 2002

Abstract—The process of signal amplification in an active medium of the helical electron beam–backward electromagnetic wave type (gyro-backward-wave tube) has been theoretically analyzed. The same process has been studied in a gyro-backward-wave tube with an electrodynamic structure representing coupled waveguide systems. © *2003 MAIK "Nauka/Interperiodica".*

Gyroamplifiers and gyrooscillators employing fast electromagnetic waves are now considered as a promising class of high-power microwave devices for the millimeter wavelength range [1]. Of special interest among these devices are gyro-backward-wave tubes (gyro-BWTs) [2–7], in which a helical (polyhelical) electron beam interacts with the counterwave in a waveguide system under cyclotron resonance conditions $\hat{\omega} + \beta_0(\hat{\omega})v_\parallel \approx \omega_c$, where $\hat{\omega}$ is the synchronism frequency, ω_c is the cyclotron frequency, and $v_\parallel$ is the longitudinal electron velocity (i.e., the velocity component along the applied magnetic field B_0), and $\beta_0(\hat{\omega})$ is the wave propagation constant in a waveguide without an electron beam. An important advantage of such systems is the possibility to effectively control the working frequency by varying the longitudinal electron velocity $v_\parallel$ or the guiding magnetic field strength B_0.

The amplification of signals in such systems can be described within the framework of a self-consistent model, including the equation of motion of electrons in a weakly-relativistic helical beam and a steady-state equation describing excitation of the backward wave by the electron beam [8, 9]:

$$\frac{d\beta}{d\xi} - j\mu(1-|\beta|^2)\beta = F, \quad \frac{\partial F}{\partial \xi} - jbF = \frac{1}{2\pi}\int_0^{2\pi}\beta d\theta_0. \quad (1)$$

Here, $\beta = r\exp(j\theta)$ is the complex trajectory radius of electrons in the ensemble with initially homogeneous distribution with respect to phase relative to the high-frequency (HF) field; $F = F(\xi)$ is the complex dimensionless field amplitudes in the beam cross section; ξ is the dimensionless longitudinal coordinate; $\mu = (v_\parallel/c)/\varepsilon$ is the parameter of nonisochronism characterizing the degree of inertia of the system (i.e., the rate of variation of the phase of electrons in response to a change in their velocity); $\varepsilon \ll 1$ is the interaction parameter (analogous to the Pierce gain parameter in the theory of *O*-type devices with prolonged interaction [10, 11]); $b = (\omega + \beta_0 v_\parallel - \omega_c)/k\varepsilon v_\parallel$ is the parameter of nonsynchronism (proportional to a detuning between the working frequency ω and the cold synchronism frequency $\hat{\omega}$); and $k = \omega/c$. The main assumptions underlying model (1) are considered in detail in [2, 10, 12].

For description of the process of signal amplification, the boundary and initial conditions for Eqs. (1) are set as

$$F(\xi = A) = F_0, \quad \beta(\xi = 0) = \exp(j\theta_0), \quad \theta_0 \in [0, 2\pi], \quad (2)$$

where the first condition indicates that an external field F_0 is applied to the system input ($\xi = A$, collector end), while the second condition reflects the fact that a helical electron beam enters the interaction space in the unmodulated state (oscillating electrons in the helical beam are homogeneously distributed with respect to their phases relative to the HF field phase).

Iterative analysis of the interaction of a helical electron beam with the backward electromagnetic wave yields, in the first (linear) approximation, the following expression for the field strength at the end of the waveguide system ($\xi = 0$):

$$F(0) = F_0 e^{j\beta_0 A}[(1 + A^2\mathrm{Re}\Psi(\Phi_0) + \mu A^3\mathrm{Re}\Theta(\Phi_0))^2 + (A^2\mathrm{Im}\Psi(\Phi_0) + \mu A^3\mathrm{Im}\Theta(\Phi_0))^2]^{1/2} \times \exp(\psi_1(\Phi_0, A, \mu)), \quad (3)$$

where $\psi_1(\Phi_0, \xi, \mu)$ is a function describing the field phase in the gyro-BWT (the explicit form can be found in [12]); $\Psi(\Phi_0)$ and $\Theta(\Phi_0)$ are the functions

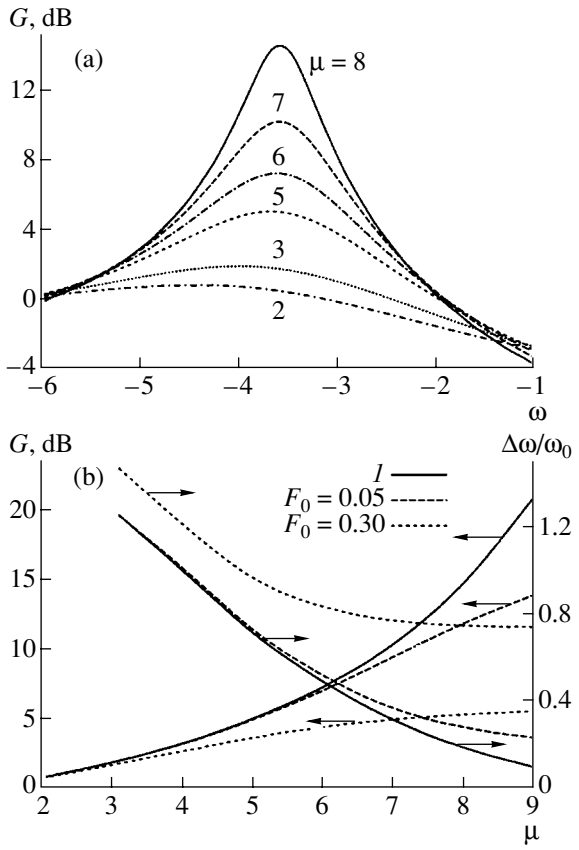

Fig. 1. Backward-wave gyroamplifier: (a) amplitude–frequency characteristics in the small signal regime at various values of the nonisochronism parameter μ; (b) plots of the maximum gain G_{max} and the relative width $\Delta\omega/\omega_0$ of the transmission band versus the parameter of nonisochronism μ (solid curves *1* show the results obtained using a linear approximation).

characterizing the linear and quadratic groups, respectively [13],

$$\Psi(\Phi_0) = \frac{1 - e^{-j\Phi_0} - j\Phi_0}{\Phi_0^2},$$
$$\Theta(\Phi_0) = \frac{2(e^{-j\Phi_0} - 1) + j\Phi_0(e^{-j\Phi_0} + 1)}{\Phi_0^3}, \quad (4)$$

and $\Phi_0 = (b + \mu)A$ is the relative angle of flight of oscillating electrons of the helical beam in the interaction space.

Using expression (3), one can readily determine the gyro-BWT gain G as dependent on the relative angle of flight Φ_0 and, hence, on the frequency ω of the external signal. Note that this calculation yields the gyro-BWT gain in the regime of amplification of small signals ($|F_0| \ll 1$), since the field distribution (3) was obtained in a linear approximation.

Figure 1a shows plots of the gain G versus frequency ω calculated using expression (3) for various values of the nonisochronism μ. The negative frequency values are possible because ω is determined as a correction to the synchronism frequency $\hat{\omega}$. As can be seen from these data, the maximum gain increases with the parameter of nonisochronism.

Figure 1b (solid curves) shows plots of the relative width $\Delta\omega/\omega_0$ of the transmission band and the maximum gain G_{max} in the regime of small signal amplification versus the parameter of nonisochronism μ. Here, the band width is determined at a level of 3 dB and the frequency ω_0 corresponds to the maximum gain (G_{max}). As can be seen from these data, the gain rapidly grows with the parameter of nonisochronism μ to reach a level on the order of 20 dB. At the same time, the $\Delta\omega/\omega_0$ value decreases with increasing μ. The transmission band can be quite readily shifted within a broad frequency interval by varying the longitudinal electron velocity $v_\parallel$ or the magnetic field strength B_0. Taking into account the small width of the transmission band, a backward-wave gyroamplifier can be considered as an active narrow-band filter for the millimeter wavelength range.

In the regime of amplification of signals with sufficiently large amplitudes F_0, expression (3) is no longer valid and the amplification process has to be described using the initial system of equations (1) and (2). Figure 1b (dashed curves) shows the characteristics of a backward-wave gyroamplifier as functions of the nonisochronism μ in the regime of finite-amplitude signal amplification constructed by data of the numerical solution of Eqs. (1) and (2) for two values of the signal amplitude, $F_0 = 0.05$ and 0.3. In the former case, the curves of $\Delta\omega(\mu)/\omega_0$ and $G_{max}(\mu)$ significantly differ from the results obtained using the linear theory only for large values of the parameter ($\mu > 6.0$). This is related to the fact that the parameter of nonisochronism determines the phase nonlinearity of a gyro-BWT ($\sim\mu(1 - |\beta|)^2\beta$). For greater μ, the nonlinear effects are manifested at a smaller amplitude of the HF field. In the latter case ($F_0 = 0.3$), the results of numerical calculations significantly differ from small-signal theory predictions: the gain drops sharply and the transmission band of the gyro-BWT width significantly increases. Thus, by varying the signal amplitude at the input within sufficiently wide limits, it is possible to effectively control the transmission band width of a gyroamplifier (active filter).

A promising modification of the gyro-BWT consists in using an electrodynamic structure in the form of coupled waveguide systems (CWSs) [14]. As was demonstrated previously, such a system provides for a significant increase in both efficiency and output power given an optimal adjustment of the coupling between waveguide systems. In connection with this, it is interesting to analyze the gain of a backward-wave gyroamplifier with CWSs. A system of nonlinear steady-state equations describing signal amplification in such an

amplifier with a helical electron beam and CWSs can be written as [14] (see also [15, 16])

$$d\beta/d\xi - j\mu(1 - |\beta|^2)\beta = F_1, \tag{5}$$

$$\frac{\partial F_1}{\partial \xi} - jbF_1 + j\alpha F_2 = \frac{1}{2\pi}\int_0^{2\pi} \beta d\theta_0,$$
$$\frac{\partial F_2}{\partial \xi} - jbF_2 + j\alpha F_1 = 0, \tag{6}$$

$$F_1(\xi = A) = F_0, \quad F_2 = (\xi = A) = 0,$$
$$\beta(\xi = 0) = \exp(j\theta_0), \quad \theta_0 \in [0, 2\pi], \tag{7}$$

where the helical beam is assumed to propagate through the first waveguide system. In Eqs. (5)–(7), $F_{1,2}$ are functions proportional to HF field amplitudes in the corresponding waveguide system and α is the parameter of coupling between these waveguide systems. The initial condition (7) indicates that the signal is applied to the input ($\xi = A$) of the first waveguide system.

Figure 2a shows plots of the relative width $\Delta\omega/\omega_0$ of the transmission band and the gain G versus coupling coefficient α calculated within the framework of the mathematical model (5)–(7) for a gyro-BWT with CWSs in the case of small signal amplitude. As can be seen, the gain drops with increasing coupling (parameter α) between the waveguide systems. This behavior is related to the fact that, as α grows, an increasing part of the power enters the coupled waveguide system and, hence, a helical electron beam interacts with an HF field of smaller amplitude, which results in lower gain G. Note that a decrease in the gain is equally well pronounced for both large (solid curve in Fig. 2a) and small (dashed curve) coupling coefficient α.

Now let us consider how the variation of coupling between waveguide systems in the gyro-BWT the relative width influence the width $\Delta\omega/\omega_0$ of the transmission band. For small values of the nonisochronism (see Fig. 2a, the dashed curve for $\mu = 5.0$), the band width monotonically increases with growing coupling between the waveguide systems. A different behavior is observed for large values of the nonisochronism. In this case, as can be seen from Fig. 2a (solid curve for $\mu = 8$), the band width slightly decreases (with an insignificant decrease in the gain) at small values of the coupling coefficient and starts increasing only at large values of the coupling parameter; the relative increase in $\Delta\omega/\omega_0$ is smaller than that for small μ values.

It is possible to use a backward-wave gyroamplifier as an active tunable power divider, since the HF power at the output can be distributed between waveguide systems in a certain ratio depending on the coupling coefficient α. This is illustrated in Fig. 2b, where the ratio of the output field amplitudes $\kappa = |F_2(\xi = 0)|/|F_1(\xi = 0)|$ for the two waveguide systems is plotted versus the coupling coefficient α for various values of the nonisochronism μ. As can be seen, the character of the curves remains qualitatively the same, irrespective of the μ value. For $\alpha < 0.6$–0.8, the $\kappa(\alpha)$ value almost linearly varies from 0 to 1, which implies that the power can be divided in an arbitrary ratio between the two waveguide systems in this interval of the coupling parameter. For $\alpha > 1.0$, the power is predominantly pumped to the waveguide system without an electron beam. In this case, the field amplitude $|F_2|$ rapidly grows with the coupling coefficient but, as demonstrated above, the gain of the backward-wave gyroamplifier sharply drops.

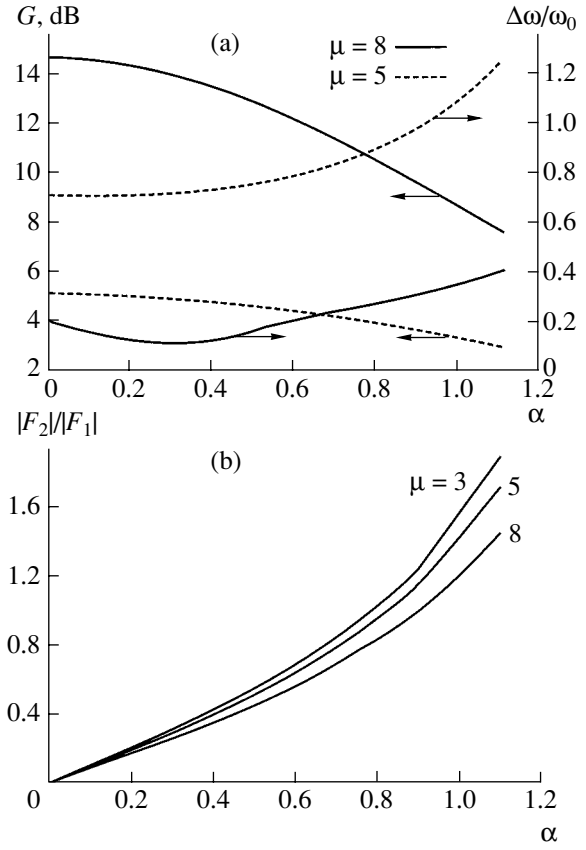

Fig. 2. Backward-wave gyroamplifier with coupled waveguide systems: (a) plots of the maximum gain G and the relative width $\Delta\omega/\omega_0$ of the transmission band in the small signal regime versus coupling coefficient α; (b) plots of the ratio of the output field amplitudes $\kappa = |F_2(\xi = 0)|/|F_1(\xi = 0)|$ for the two waveguide systems versus coupling coefficient α for various values of the nonisochronism μ.

Acknowledgments. This study was supported by the Russian Foundation for Basic Research (project no. 02-02-16531) and by the Federal Program "Russian Universities–Basic Research" (project UR.01.01.065).

REFERENCES

1. K. L. Felch, B. G. Danly, H. R. Jory, *et al.*, Proc. IEEE **87**, 752 (1999).

2. A. Yu. Dmitriev, D. I. Trubetskov, and A. P. Chetverikov, Izv. Vyssh. Uchebn. Zaved., Radiofiz. **34**, 595 (1991).
3. C. S. Kou, S. H. Chen, L. R. Barnett, *et al.*, Phys. Rev. Lett. **70**, 924 (1993).
4. K. R. Chu, H. Y. Chen, C. L. Hung, *et al.*, Phys. Rev. Lett. **81**, 4760 (1998).
5. G. S. Nusinovich, A. N. Vlasov, and T. M. Antonsen, Phys. Rev. Lett. **87**, 218301 (2001).
6. D. I. Trubetskov and A. E. Khramov, Pis'ma Zh. Tekh. Fiz. **28** (18), 34 (2002) [Tech. Phys. Lett. **28**, 767 (2002)].
7. A. A. Koronovskiĭ, I. S. Rempen, D. I. Trubetskov, and A. E. Khramov, Izv. Ross. Akad. Nauk, Ser. Fiz. **66**, 1754 (2002).
8. V. K. Yulpatov, Vopr. Radioélektron., Ser. 1, Élektron., No. 12, 15 (1965).
9. D. I. Trubetskov and A. P. Chetverikov, Izv. Vyssh. Uchebn. Zaved., Prikl. Nelin. Din. **2** (5), 3 (1994).
10. A. Yu. Dmitriev, A. E. Konevets, L. A. Pishchik, *et al.*, in *Lectures on Microwave Electronics and Radiophysics: Proceedings of the 7th Winter School-Workshop for Engineers* (Saratov. Univ., Saratov, 1986), Part 3, p. 61.
11. L. A. Vaĭnshteĭn and V. A. Solntsev, *Lectures on Microwave Electronics* (Sov. Radio, Moscow, 1973).
12. D. I. Trubetskov and A. E. Khramov, Izv. Ross. Akad. Nauk, Ser. Fiz. **66**, 1761 (2002).
13. V. N. Shevchik and D. I. Trubetskov, *Analytical Calculation Methods in Microwave Electronics* (Sov. Radio, Moscow, 1970).
14. A. A. Koronovskiĭ and A. E. Khramov, Pis'ma Zh. Tekh. Fiz. **29** (4), 63 (2003) [Tech. Phys. Lett. **29**, 160 (2003)]; A. A. Koronovskiĭ, D. I. Trubetskov, and A. E. Khramov, Zh. Tekh. Fiz. **73** (6), 110 (2003) [Tech. Phys. **48**, 768 (2003)].
15. W. H. Louisell, *Coupled Mode and Paramagnetic Electronics* (Wiley, New York, 1960; Inostr. Lit., Moscow, 1963).
16. D. I. Trubetskov, in *Lectures on Microwave Electronics and Radiophysics: Proceedings of the 3rd Winter School-Workshop for Engineers* (Saratov. Univ., Saratov, 1978), p. 89.

Translated by P. Pozdeev

Technical Physics Letters, Vol. 29, No. 6, 2003, pp. 471–473. Translated from Pis'ma v Zhurnal Tekhnicheskoĭ Fiziki, Vol. 29, No. 11, 2003, pp. 65–71.

The Photomagnetic Effect Detected by Nuclear Magnetic Resonance

I. V. Pleshakov

Ioffe Physicotechnical Institute, Russian Academy of Sciences, St. Petersburg, 194021 Russia

e-mail: vp.shuv@pop.ioffe.rssi.ru

Received November 25, 2002; in final form, February 5, 2003

Abstract—The results of experiments with transparent easy-plane antiferromagnetic iron borate ($FeBO_3$) show that nuclear magnetic resonance (NMR) offers an effective tool for the study of photomagnetism in magnetically ordered materials. It is established that illumination of a $FeBO_3$ sample leads to a shift of the ^{57}Fe NMR frequency due to a change in the electron magnetization and significantly increases the nuclear induction signal intensity in the range of existence of the domain boundaries. *© 2003 MAIK "Nauka/Interperiodica".*

Photomagnetic phenomena in magnetically-ordered materials, by which are implied any changes in the magnetic characteristics of samples under the action of light, are very interesting from the standpoint of basic physics and have been continuously studied since their discovery in the late 1960s [1]. From a practical standpoint, important results of these investigations are the prospects for magnetooptical data recording and the search for most promising recording media.

As is well known, the method of nuclear magnetic resonance (NMR) is sensitive to rather fine features (frequently not detected by other methods) in the behavior of ordered magnetic materials, because the main NMR characteristics are determined by the magnetic properties of the material studied [2]. The NMR frequencies depend on the electron magnetization of sublattices, while the signal amplitude is determined by the anisotropic fields, susceptibility of the domain boundaries, etc. Since the properties of a photomagnetic material change under the action of light, it can be expected that NMR can serve as an effective indicator of photomagnetism and may reveal new sides of this phenomenon. This study aimed at determining and demonstrating the wide possibilities of NMR in the study of photomagnetism.

The experiments were performed with iron borate ($FeBO_3$), a compound representing the group of the few materials capable of retaining magnetic order and optical transparency in the visible spectral range at relatively high temperatures. The photomagnetic effect in $FeBO_3$ has been studied in considerable detail [3–10] and it is reliably established that the observed phenomena are related to the properties of this substance as such, rather than to some impurities (which are only capable of increasing the photosensitivity). At the same time, the narrow and intense NMR signal in iron borate make this compound virtually the only candidate as a model object for solving the aforementioned problem.

We used a sample of pure $FeBO_3$ in the form of a thin rectangular single crystal with dimensions $2 \times 2 \times 0.2$ mm and the large plane coinciding with the easy magnetization plane. The sample was enriched with ^{57}Fe up to 80%. The NMR on these nuclei, excited by RF pulses at a carrier frequency of $f \cong 75.4$ MHz, was detected as a free induction signal. The domain structure in the sample was controlled by application of a constant magnetic field with the induction B varied from 0 to 10 mT. The RF and constant fields were mutually perpendicular and oriented in the plane of the sample.

The photomagnetic response was induced by the light of an incandescent lamp possessing a wide emission spectrum. The light flux was transmitted to a measuring cell via an optical fiber bundle and directed to the sample surface via a diffuser ensuring uniform illumination at a radiant power density of ~0.1 W/cm^2. The NMR measurements were performed at liquid nitrogen temperature.

At a small constant magnetic field, the NMR spectrum exhibited a signal split into two peaks, which merged together only at a field strength of 5–6 mT (Fig. 1). The appearance of several lines in the NMR spectrum of $FeBO_3$ was also reported previously [11–13], but the signal behavior in the applied magnetic field showed a different character because the experiments were performed under essentially different conditions. Indeed, the samples were excited by pulses of rather high power and the configuration of applied fields in some variants was different, so that the NMR signals were received from nuclei occurring in differently oriented domains. In this study, the signal was received from nuclei in the domain walls which could be excited at a significantly lower RF pulse power as compared to that required in the saturated state.

1063-7850/03/2906-0471$24.00 © 2003 MAIK "Nauka/Interperiodica"

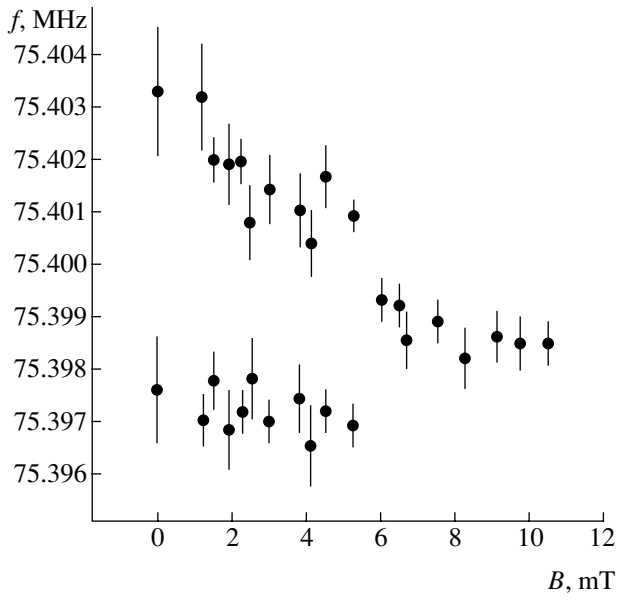

Fig. 1. A plot of the frequencies of NMR peaks versus applied magnetic field strength.

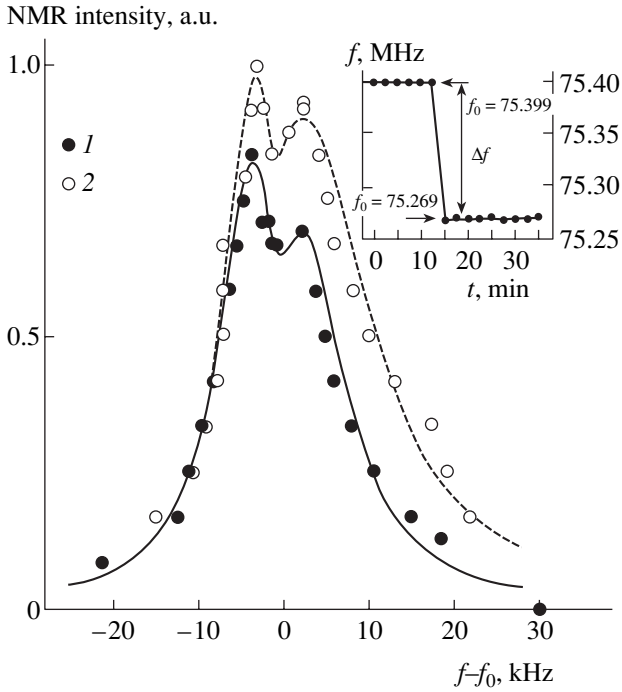

Fig. 2. A comparison of the NMR spectra of iron borate measured at $B = 2.5$ mT (*1*) without and (*2*) with illumination of the sample. The inset shows a time variation in the NMR peak frequency after switching on the illumination ($B = 7.5$ mT).

As is known, the domain structure of a completely demagnetized iron borate may feature both Bloch and Néel domain walls [4, 14–16], but the latter disappear even in a very small external magnetic field (on the order of a few tenths of millitesla). Therefore, both peaks in the NMR spectrum are most likely related to the Bloch walls, which is confirmed by the same level of optimum excitation (equal 90° pulses). Factors accounting for the NMR signal splitting in domain boundaries of the same type are still incompletely clear, but it can be suggested that this effect is related to the existence of Bloch walls of two types differing by the magnetization rotation angles [4, 14]. Complete magnetization of $FeBO_3$ was observed at $B_{sat} = 1.6$ mT [16], but this value may depend on the conditions and vary from one sample to another. For the iron borate crystal used in this study, the saturation field was previously estimated at $B_{sat} \approx 5$ mT (at $T = 77$ K) [17], which agrees well with the data in Fig. 1. The main experiments on the NMR detection of the photomagnetic effect were performed at $B = 2.5$ and 7.5 mT, that is, in the states referred to as multidomain and single-domain, respectively.

After switching on the light, the NMR frequency decreased with a characteristic time not exceeding 2.5 min (see the inset in Fig. 2). The frequency change Δf is conventionally evaluated as a shift of the central frequency determined, in the case of a complex spectrum, as an average of the component frequencies. This Δf value corresponds to a decrease in the sublattice magnetization by 0.17%, which coincides in the order of magnitude with the data [10] obtained using laser radiation with $\lambda = 0.63$ μm and approximately the same power density as that in the experiment described here. According to Patrin *et al.* [9, 10], the photoinduced change in the magnetization (caused by redistribution of the population of levels in photosensitive Fe^{2+} ions) amounts to not less than 35%, while theoretically it can be even higher. Using the numerical data from [8, 10], the thermal contribution to the Δf value (due to the sample heating) can be roughly estimated at 10%.

It should be noted that the action of light on the sample in the experiment described here was not only accompanied by a decrease in the NMR frequency but also led to a significant increase in the signal intensity. This fact qualitatively confirms that the mechanism of the observed phenomenon is essentially nonthermal, since thermal factors would only decrease the spin response of the system. Taking into account that Δf exhibited no significant dependence on B in the range of field strengths studied, one may conclude that photoinduced changes in the electron magnetization inside the domain and in the domain wall are the same.

It should also be emphasized that, since the NMR frequency is related to the magnetization of a particular sublattice (the crystal structure of $FeBO_3$ comprises two equivalent sublattices) rather than to the total magnetization of a sample, the results of radiospectroscopic investigations provide information about the photoinduced changes on a more local level than do the magnetometric data.

A convenient comparison of the features of NMR spectra measured with and without illumination of the sample is provided by constructing the two profiles on

the same plot as functions of the differential frequency $f–f_0$ (Fig. 2). Note the almost exact coincidence of peak positions in the multidomain range (B = 2.5 mT) and the increase in the NMR signal intensity under illumination (more pronounced for the right-hand wing of the spectrum). At B = 7.5 mT, the signal intensity also increases (approximately, by 25%), but the growth is more uniform over the spectrum and is probably due to a decrease in the effective anisotropic field in the basal plane (which is one of the photomagnetic effect manifestations in iron borate [5]). Since the NMR gain in the domain walls is determined b their susceptibility [2], one may suggest that the asymmetric effect of illumination on the NMR spectrum at B = 2.5 mT is related to the different action of light on the susceptibility of Bloch walls with various magnetization rotation angles.

Thus, this study has demonstrated for the first time the possibilities of NMR as a tool for studying photomagnetic phenomena in magnetically ordered crystals. Some new features of the photomagnetic process have been found, which are manifested in the NMR spectrum of iron borate and will be the subject of subsequent investigations.

REFERENCES

1. U. Enz, W. Lems, R. Metselaar, *et al.*, IEEE Trans. Magn. **MAG-5**, 467 (1969).
2. E. A. Turov and M. P. Petrov, *Nuclear Magnetic Resonance in Ferro- and Antiferromagnets* (Moscow, 1969).
3. D. E. Lacklison, J. Chadwick, and J. L. Page, J. Appl. Phys. **42**, 1445 (1971).
4. D. E. Lacklison, J. Chadwick, and J. L. Page, J. Phys. D **5**, 810 (1972).
5. M. H. Seavey, Solid State Commun. **12**, 49 (1973).
6. M. Borovets, A. A. Garmonov, S. G. Rudov, *et al.*, Pis'ma Zh. Éksp. Teor. Fiz. **50**, 431 (1989) [JETP Lett. **50**, 466 (1989)].
7. G. A. Petrakovskii, G. S. Patrin, and N. V. Volkov, Phys. Status Solidi A **87**, K153 (1985).
8. G. S. Patrin, G. A. Petrakovskii, and V. V. Rudenko, Phys. Status Solidi A **99**, 619 (1987).
9. G. S. Patrin, D. A. Velikanov, and G. A. Petrakovskii, Zh. Éksp. Teor. Fiz. **103**, 234 (1993) [JETP **76**, 128 (1993)].
10. G. S. Patrin, D. A. Velikanov, and G. A. Petrakovskii, Fiz. Tverd. Tela (St. Petersburg) **37**, 1214 (1995) [Phys. Solid State **37**, 659 (1995)].
11. R. A. Bagautdinov, Kh. G. Bogdanova, V. A. Golenishchev-Kutuzov, *et al.*, Fiz. Tverd. Tela (Leningrad) **28**, 924 (1986) [Sov. Phys. Solid State **28**, 518 (1986)].
12. Kh. G. Bogdanova, V. A. Golenishchev-Kutuzov, L. I. Medvedev, *et al.*, Fiz. Tverd. Tela (Leningrad) **33**, 379 (1991) [Sov. Phys. Solid State **33**, 219 (1991)].
13. Kh. G. Bogdanova, V. E. Leont'ev, and M. M. Shakirzyanov, Fiz. Tverd. Tela (St. Petersburg) **41**, 290 (1999) [Phys. Solid State **41**, 259 (1999)].
14. J. Haisma and W. T. Stacy, J. Appl. Phys. **44**, 3367 (1973).
15. G. B. Scott, J. Phys. D **7**, 1574 (1974).
16. N. M. Salanskiĭ, E. A. Glozman, and V. N. Seleznev, Zh. Éksp. Teor. Fiz. **68**, 1413 (1975) [Sov. Phys. JETP **41**, 704 (1975)].
17. M. P. Petrov, A. V. Ivanov, A. P. Paugurt, *et al.*, Fiz. Tverd. Tela (Leningrad) **29**, 1819 (1987) [Sov. Phys. Solid State **29**, 1044 (1987)].

Translated by P. Pozdeev

Technical Physics Letters, Vol. 29, No. 6, 2003, pp. 474–476. Translated from Pis'ma v Zhurnal Tekhnicheskoĭ Fiziki, Vol. 29, No. 11, 2003, pp. 72–78.

Magnesium Outdiffusion from Porous Silicon Carbide Substrates during Autodoping of Gallium Nitride Epilayers

M. G. Mynbaeva, A. A. Lavrent'ev, A. V. Fomin, K. D. Mynbaev, and A. A. Lebedev

Ioffe Physicotechnical Institute, Russian Academy of Sciences, St. Petersburg, 194021 Russia

e-mail: mgm@mail.ioffe.ru

Received December 10, 2002

Abstract—We have studied the outdiffusion of magnesium from silicon carbide substrates during autodoping of gallium nitride epilayers. The autodoping effect was observed in the case of porous substrates obtained by surface anodization of 6H-SiC wafers. It is established that the magnesium distribution profiles can be controlled by post-growth annealing. The fact of doping is confirmed by the results of photoluminescence measurements at 77 K. © *2003 MAIK "Nauka/Interperiodica".*

Gallium nitride (GaN) is a promising material for optoelectronics and high-temperature electronics, which is related to a large bandgap width (3.4 eV) and the stability of material properties at high temperatures and in contact with reactive environment. An important problem encountered in the development of GaN-based device structures is related to the obtaining of *p*-type material, which is usually achieved by doping GaN with magnesium [1]. Since bulk GaN substrates are not available, the epitaxial layers (epilayers) for device structures are grown on foreign substrates, in particular, on silicon carbide wafers [2].

One possible way to obtaining GaN epilayers with a required dopant concentration is offered by the process of autodoping from a substrate preliminarily saturated with the corresponding element (by analogy with the process used in silicon technology) [3]. The autodoping process requires additional annealing for the dopant diffusion and activation. In GaN/SiC system, this circumstance leads to a certain problem, because the temperature of GaN epitaxy is usually about 1000°C [2] and the post-growth annealing temperature does not exceed 900°C [1], whereas effective diffusion in SiC requires a temperature about twice as large [4].

Recently [5], we established that high diffusion coefficients of impurities at temperatures on the order of ~1000°C can be achieved in porous silicon carbide (PSC) [5]. Taking into account that previously we also demonstrated that the quality of GaN epilayers can be improved by growth on porous substrates [6], it was also of interest to study the possibility of GaN autodoping from PSC substrates.

Here we report on the magnesium autodoping of GaN epilayers grown of PSC substrates. The porous structure of silicon carbide served as a matrix for magnesium, which could diffuse from the substrate into a growing film during the epitaxial growth of gallium nitride. The distribution of Mg in GaN epilayer was controlled by post-growth annealing. The GaN doping was confirmed by the results of photoluminescence (PL) measurements at 77 K.

The experiments were performed on on- and off-axis (0001) 6H-SiC wafers. Layers of PSC with a thickness of about 3 μm were obtained by surface anodization of the initial wafers in an HF solution using a procedure similar to that described in [7]. Prior to anodizing, half of each wafer was coated with a protective mask, so that the porous layer was formed only on the unprotected part of the wafer. Then the protective mask was removed and the entire wafer surface was subjected to implantation with 70-keV Mg ions at room temperature (T = 300 K) to a total ion dose of 5×10^{14} or 1.5×10^{15} cm^{-2}.

Both before and after the ion implantation, the surface of wafers was characterized by reflection high-energy electron diffraction (RHEED). The RHEED measurements were performed using the electron beam oriented parallel to ⟨11–20⟩ direction and reflected from the surface at an angle of about 2°. The results of measurements performed after anodization showed that the surface protected by the mask during etching was structurally more perfect. The implantation of magnesium led to amorphization of both parts of the wafer, but the thickness of an amorphized layer on the unanodized surface was about 20 Å, while the thickness of amorphized layer on PSC was about one-fourth of this value.

GaN epilayers were obtained by the method of chloride hydride vapor phase epitaxy (HVPE) under conditions similar to those reported in [8]. The thickness of a GaN epilayer obtained by this method was typically ~600 nm. A fraction of wafers was then subjected to an

additional annealing at 900°C for 20 min in a nitrogen atmosphere.

The distribution of magnesium in SiC upon implantation and in the GaN/SiC structures upon growth and annealing was determined by secondary-ion mass spectrometry (SIMS) profiling in a setup with a quadrupole mass analyzer. The primary beam of 9.5-keV oxygen ions with a beam current density of 100 mA/cm^2 provided for the target sputtering at a rate of 5 nm/s. The secondary current was taken from a 70-nm-diam spot at the center of a 300×300 nm raster area. The detection limit of Mg in SiC was 2×10^{16} cm^{-3}.

Figures 1 and 2 show typical depth–concentration profiles of elements in a GaN/SiC structure, measured on the unanodized and porous parts of the sample surface, respectively. For the sake of clarity, also presented are the profiles of implanted Mg in SiC and PSC substrates measured before epitaxial growth (dashed curves *1*). The shapes of these profiles were similar for both parts of the sample wafer, but the concentration of magnesium in PSC was slightly lower than in the unanodized material (1.6×10^{20} against 2.6×10^{20} cm^{-3}, respectively) and the profile width in the former case was slightly wider due to a deeper (about 20 nm) penetration of Mg atoms at the tail of the distribution (on a level of Mg concentrations ~10^{17} cm^{-3}). For both implantation doses studied, the profiles of magnesium in unanodized SiC possessed Gaussian shapes. A model curve fitted by least squares to the experimental profile for the ion dose of 1.5×10^{15} cm^{-2} gave the mean projected ion rage R = 84.8 nm at a straggling of ΔR = 25.8 nm.

An analysis of Fig. 2 reveals a significantly more blurred substrate–film interface in the case of GaN epilayer grown on PSC substrate, which is probably related to a more pronounced interdiffusion of components in the growth stage, that is, to their higher diffusion rates near the GaN/PSC interface. The same conclusion is valid for the diffusion of Mg in this structure. As can be seen from Figs. 1 and 2, the behavior of the dopant in differently treated parts of the wafer in the course of the growth process was also different. In the unanodized part (Fig. 1), the redistribution of magnesium in SiC is manifested by a loss of the dopant (decrease in the peak height) at the expense of insignificant diffusion of Mg both into SiC bulk and toward the GaN/SiC interface. The post-growth annealing additionally reduced the concentration of Mg at the distribution peak, with a weakly pronounced diffusion of Mg inward silicon carbide. At the same time, it is obvious that the interface becomes an obstacle for the diffusion of Mg from SiC into GaN: no autodoping of the epilayer takes place in this system.

In contrast, the profile of magnesium distribution in PSC (Fig. 2) exhibits significant broadening already in the epitaxial growth stage. The post-growth annealing of the GaN/PSC structure leads to still more significant changes in the distribution of Mg. In particular, there is

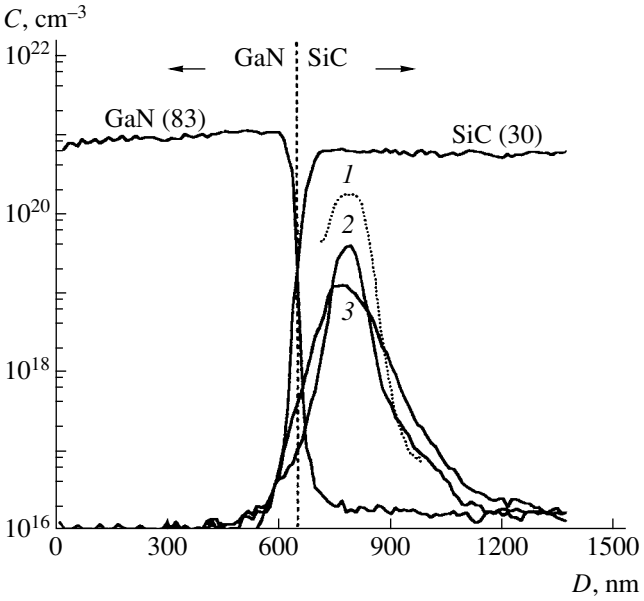

Fig. 1. Typical SIMS profiles of a GaN/SiC structure (unanodized part of the substrate): (*1*) Mg(24) in the substrate upon ion implantation; (*2*) Mg(24) upon GaN epitaxy; (*3*) Mg(24) upon post-growth annealing. Vertical dashed line shows relative boundary between substrate and epilayer.

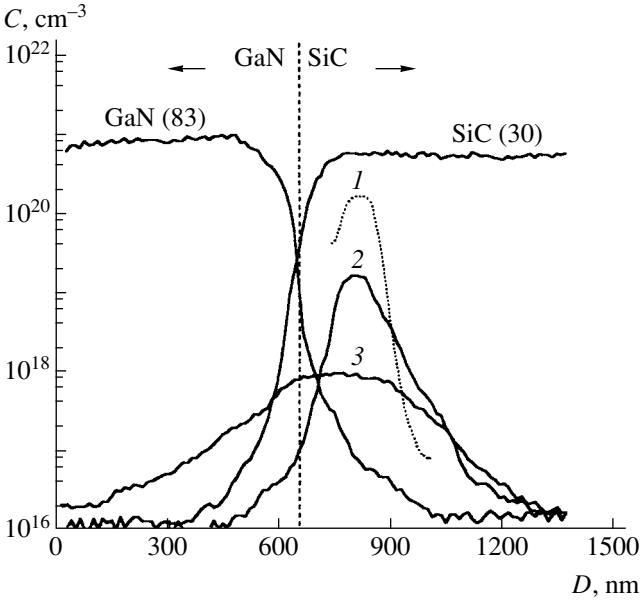

Fig. 2. Typical SIMS profiles of a GaN/PSC structure (anodized part of the substrate). Notations are the same as in Fig. 1.

evidence of Mg outdiffusion from PSC toward the interface (Fig. 2, curve *3*). Note that a similar outdiffusion was previously observed during the post-implantation annealing of SiC, in particular in structures of the AlN/SiC type [4]. In the case of PSC substrate, the outdiffusion of Mg is accompanied by its penetration into the GaN epilayer, so that the profile of Mg in this structure has a nearly symmetric shape. The concentration of

Mg in the GaN epilayer drops from ~5×10^{17} cm^{-3} at the interface to 2×10^{16} cm^{-3} at the outer surface. Since a small shift in the Mg peak position was observed in the unanodized part of the substrate as well (Fig. 1), this effect is probably a consequence of the radiation damage caused by ion implantation.

Since the dopant profiles upon annealing were well described by the Gaussian distribution curves, the estimates of the diffusion coefficients of Mg in GaN and PSC were obtained with an allowance for the above shift. This correction was provided by an additional term describing the motion of the distribution maximum at a velocity v, so that the expression in the Gaussian exponent takes the form $-(x - vt)^2/4Dt$ (D is the diffusion coefficient and t is the diffusion time) [9]. The results of fitting gave $D_{Mg} \approx 1.0 \times 10^{-13}$ cm^2/s at $v = 3.8 \times 10^{-9}$ cm/s. Note that this estimate of the diffusion coefficient of Mg at 900°C is significantly greater than the values for GaN available in the literature [10]. As for the diffusion in PSC, the D_{Mg} value has also proved to be significantly higher, for example, than the value for V at 1100°C [5]. For comparison, an estimate of the diffusion coefficient of Mg in the unanodized part of the SiC wafer (Fig. 1) is $D \approx 2.0 \times 10^{-14}$ cm^2/s. This value, albeit five times smaller than D_{Mg} in PSC, is still significantly higher than that anticipated for the diffusion of Mg in SiC at 900°C. Similar estimates were obtained using the profiles of magnesium distribution in the samples implanted to the initial dose of 5×10^{14} cm^{-2}. Thus, we may ascertain that the system under consideration features accelerated diffusion of magnesium, probably caused both by radiation defects and by certain features of the GaN/PSC structure near the interface. It should be noted that the miscut of the initial SiC wafer surface relative to the c axis did not influence the results.

In order to verify the fact of doping, both parts of a SiC wafer with GaN epilayers were characterized by measuring photoluminescence (PL) at 77 K. The emission was excited by a beam of a 2-kW nitrogen laser incident on the sample at an angle of 45°. The PL signal was detected by a photomultiplier. The PL spectra of GaN epilayers grown on PSC exhibited a broad emission band in the blue spectral range, peaked at 450 nm. Such bands are typically observed in Mg-doped GaN and attributed to the electron transitions to an acceptor level created by Mg impurity [1]. No such emission bands were observed in the PL spectrum of GaN epilayers grown on unanodized SiC substrates. Thus, the PL data confirm the diffusion of Mg from PSC into GaN epilayers.

Acknowledgments. The authors are grateful to A.S. Zubrilov for conducting PL measurements.

REFERENCES

1. J. K. Sheu and G. C. Chi, J. Phys.: Condens. Matter **14**, R657 (2002).
2. M. Kamp, Opt. Quantum Electron. **32**, 227 (2000).
3. P. Jerier and D. Dutartre, J. Electrochem. Soc. **146**, 331 (1999).
4. E. M. Handy, M. V. Rao, K. A. Jones, *et al.*, J. Appl. Phys. **86**, 746 (1999).
5. M. G. Mynbaeva, A. V. Lavrent'ev, A. N. Kuznetsov, *et al.*, Fiz. Tekh. Poluprovodn. **37** (5), 612 (2003) [Semiconductors **37**, 594 (2003)].
6. M. Mynbaeva, A. Titkov, A. Kryganovskii, *et al.*, MRS Internet J. Nitride Semicond. Res. **4**, 14 (1999).
7. M. Mynbaeva and D. Tsvetkov, Inst. Phys. Conf. Ser. **155**, 365 (1997).
8. Yu. Mel'nik, I. Nikitina, A. Zubrilov, *et al.*, Inst. Phys. Conf. **142**, 863 (1995).
9. S. S. Gorelik and M. Ya. Dashevskiĭ, *Materials Science of Semiconductors and Insulators* (Moscow, 1988).
10. C. J. Pan and G. C. Chi, Solid-State Electron. **43**, 621 (1999).

Translated by P. Pozdeev

Technical Physics Letters, Vol. 29, No. 6, 2003, pp. 477–479. Translated from Pis'ma v Zhurnal Tekhnicheskoĭ Fiziki, Vol. 29, No. 11, 2003, pp. 79–85.

Fullerene-Containing C_{60}–CdTe(CdSe) Composite Nanostructures

S. O. Kognovitskiĭ, A. V. Nashchekin, R. V. Sokolov, I. P. Soshnikov, and S. G. Konnikov

Ioffe Physicotechnical Institute, Russian Academy of Sciences, St. Petersburg, 194021 Russia
e-mail: nashchekin@mail.ioffe.ru

Received December 24, 2002; in final form, February 6, 2003

Abstract—We have developed a technology for obtaining homogeneous films based on fullerene-containing C_{60}–CdTe and C_{60}–CdSe composites. The surface morphology of the initial films is characterized by an average lateral roughness size of about 150 nm. Annealing in a vacuum of 10^{-5} Torr for 3 h showed that C_{60}–CdSe films are stable at temperatures up to $T = 180$°C, while the same treatment of films of the $(C_{60})_{1-x}(CdTe)_x$ system with $x < 0.5$ leads to the appearance of surface clusters of the semiconductor component with an average size of about 500 nm. The cluster density and size increase with the content of CdTe in the initial composite powder. The photoluminescence spectrum of a $(C_{60})_{1-x}(CdTe)_x$ film with $x = 0.5$ upon annealing displays a dominating peak at 730 nm, which is indicative of a significant modification of the film structure as a result of this post-growth treatment. It is demonstrated that fullerene-containing composite network nanostructures with a lateral resolution up to 250 nm can be created by direct electron-beam lithography. *© 2003 MAIK "Nauka/Interperiodica".*

Introduction. The optical properties of fullerene-based composites strongly depend on both the elemental composition and structure of the material. This opens wide possibilities in the synthesis of novel composite materials with desired optical properties.

The interest in materials of the $(C_{60})_{1-x}(CdA)_x$ system, where A = Se or Te and x varies from 0 to 1, is related to the fact that the absorption edges of these compounds fall in the visible and near UV spectral range that is most important for optoelectronic applications. Good prospects of fullerene-containing resists are also related to the fact that the theoretical resolution limit for the electron-beam lithography, as determined by the size of resist molecules, is about ten times smaller for fullerenes (~7 Å) in comparison to the standard polymeric electron resists. Possessing good masking properties, fullerene-based compositions can be used as electron resists (with subsequent dry reactive etching) for semiconductors [1, 2], either independently or as additives to standard resists. However, to the best of our knowledge, no methods were developed for obtaining network nanostructures using thin fullerene-containing composite films.

Technology of $(C_{60})_{1-x}(CdA)_x$ films. The main purpose of this study was to develop a technology for obtaining thin films of $(C_{60})_{1-x}(CdA)_x$ composites, where A = Se or Te and x varies from 0 to 1. The first stage is the synthesis of materials with desired stoichiometric compositions. To this end, thoroughly mixed powders of CdTe or CdSe with fullerene (99.98% C_{60}) in a certain proportion are sintered and then mechanically ground to obtain a granulated composite with an average particle size of about 1 μm.

Thin films of desired composition on a selected substrate were obtained by thermal deposition in vacuum. In our experiments, the substrates were specially prepared GaAs(100) and Si(100) plates. Immediately before film application, the initial composite was kept in vacuum for 2 h for degassing and eliminating organic solvent residues. During deposition, the residual pressure in the vacuum chamber did not exceed 10^{-5} Torr. The substrate temperature was maintained about 160°C.

Using this technology, we obtained C_{60}–CdTe and C_{60}–CdSe composite films with compositions sufficiently close to the initial stoichiometry. The film thickness were varied from 0.2 to 1 μm.

Morphology and optical properties of C_{60}–CdTe(CdSe) films. The surface morphology of the

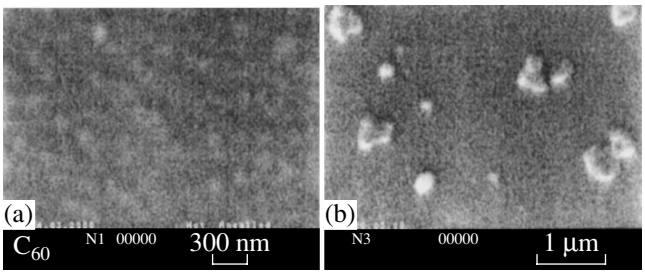

Fig. 1. SEM images showing the surface morphology of (a) C_{60} and (b) $(C_{60})_{1-x}(CdTe)_x$ composite ($x = 0.5$) films after annealing.

1063-7850/03/2906-0477$24.00 © 2003 MAIK "Nauka/Interperiodica"

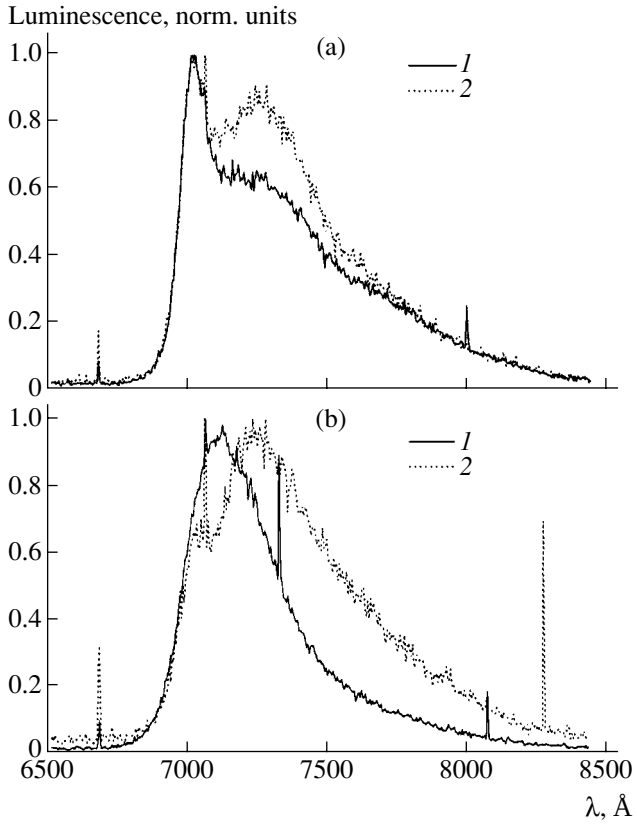

Fig. 2. Photoluminescence spectra of fullerene-based films (*1*) before and (*2*) after annealing: (a) C_{60}; (b) $(C_{60})_{1-x}(CdTe)_x$ composite with $x = 0.5$.

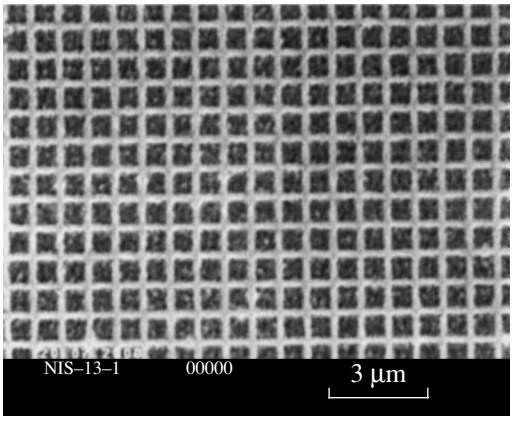

Fig. 3. A periodic lattice structure obtained by electron-beam lithography with a fullerene–semiconductor $(C_{60})_{0.8}(CdTe)_{0.2}$ composite resist (lattice period, 780 nm).

films was studied by scanning electron microscopy (SEM) on a CamScan Series 4-88 DV100 instrument. It was established that the films of pure C_{60} fullerene, as well as the films of $(C_{60})_{1-x}(CdA)_x$ fullerene–semiconductor composites (with A = Te or Se), possess relatively smooth surfaces with a characteristic lateral roughness size of about 150 nm (Fig. 1a).

We have also studied the effect of annealing on the surface morphology of these films. It was established that annealing of the C_{60} and $(C_{60})_{1-x}(CdSe)_x$ films in a vacuum of 10^{-5} Torr for 3 h at $T = 180°C$ does not lead to visible changes in the surface morphology. At the same time, analogous treatment of the $(C_{60})_{1-x}(CdTe)_x$ film with $x = 0.5$ leads to the appearance of bulky clusters of the semiconductor component on the sample surface, with characteristic dimensions of about 500 nm (Fig. 1b). The density of these clusters increases with the content of CdTe in the initial composite. This fact shows that the formation of large clusters is related to the presence of a semiconductor component (CdTe) in the film composition. Previously, we have observed an analogous phenomenon in films of a $(C_{60})_{1-x}Te_x$ composite.

The films with clusters were also characterized by optical methods. We have studied photoluminescence (PL) of the films of various compositions. The emission was excited by a He–Cd laser operating at a wavelength of 441.6 nm and an average power density in the beam spot of about 10 mW/cm^2. The PL measurements were performed at a sample temperature of about 2 K. The spectra were measured using a double grating spectrophotometer of the DFS-24 type and a photon count system with a cooled photoelectron multiplier. The shape of the PL spectrum was analyzed in the region of a red emission line characteristic of fullerenes.

It was found that annealing in the indicated regime virtually did not influence the shape of the PL spectra of $(C_{60})_{1-x}(CdSe)_x$ films. At the same time, the spectra of $(C_{60})_{1-x}(CdTe)_x$ films exhibit significant changes upon annealing of the samples, whereby a dominating emission band appears at 730 nm and the spectrum becomes like that of an annealed C_{60} fullerene film (cf. Figs. 2a and 2b). This variation of the PL spectra correlates with the annealing-induced changes in the surface morphology of $(C_{60})_{1-x}(CdTe)_x$ films described above. Therefore, we may suggest that annealing induces significant spatial separation of components in the $(C_{60})_{1-x}(CdTe)_x$ composite. This leads to the formation of large macroscopic clusters based on CdTe, which occur in a matrix composed predominantly of the fullerene.

Thus, we have established that thermal treatment (annealing) differently influences the morphology of fullerene-based composite films, the effect being dependent on the type of semiconductor component of the system.

The possibility of modification of the surface morphology of the composite films under consideration was used for creating surface nanostructures. We have developed a method of direct electron-beam lithography for the formation of two-dimensional network nanostructures with a preset geometry, based on the films of fullerene-containing $(C_{60})_{1-x}(CdA)_x$ compos-

ites with A = Te or Se. The negative electron resist is represented by the film proper.

The best results were obtained for the electron-beam lithography at $E = 20$ keV and $I = 10^{-9}$ A, followed by etching of the exposed regions in toluene for 25 s (Fig. 3). It was found that the electron-beam lithography with composite films has certain distinctions from the case of pure fullerene films studied previously [3]. In particular, the composite films are more sensitive to the electron beam action due to the increased average atomic number of the resist and, hence, higher efficiency of the electron energy absorption in the film [4]. However, an increase in the semiconductor content above 20 mass % makes the film insoluble in toluene and hinders its use in the electron-beam lithography. Thus, we have developed a method for the formation of two-dimensional ordered network nanostructures.

Conclusions. (1) The films of $(C_{60})_{1-x}(CdTe)_x$ composite with $x < 0.5$ are thermally unstable, which is manifested by the formation of surface clusters of the semiconductor component with an average size of about 500 nm on annealing at a temperature of $T = 180$°C. The number density and size of these clusters increase with the content of CdTe in the initial mixture. This change in the film surface morphology correlates with variations in the photoluminescence spectrum, where a dominating emission band appears at 730 nm and makes the spectrum like that of a C_{60} fullerene film upon annealing.

(2) The structure of $(C_{60})_{1-x}(CdSe)_x$ films with $x < 0.5$ is stable with respect to the thermal treatment at temperatures up to $T = 180$°C. The photoluminescence spectra of these films also exhibit no significant changes upon annealing.

(3) A combination of thermal vacuum deposition of fullerene-based $(C_{60})_{1-x}(CdTe)_x$ composite films with $x = 0.2$, followed by electron-beam lithography, may offer a promising technology for obtaining regular nanodimensional structures with controlled optical properties. Increasing the semiconductor content above 20 mass % makes the film insoluble in toluene.

Acknowledgments. The authors are grateful to M.É. Gaevskiĭ for useful advice and the discussion of results.

This study was supported in parts by the Federal Program “Integration” (project B-0101), the State Scientific-Technological Program “Currently Important Directions in Physics of Condensed Media” (Fullerenes and Atomic Clusters, Beam-2 project, no. 3-7-98), and the Joint Russian–Ukrainian Scientific-Technological Program “Creation and Study of Nonlinear Optical Switching Structures Based on Fullerene-Containing Composite Materials” (project no. 2000-5F, 2000).

REFERENCES

1. T. Tada and T. Kanayama, Jpn. J. Appl. Phys. **35**, L63 (1996).
2. A. Matsutani, F. Koyama, and K. Iga, Jpn. J. Appl. Phys. **37**, 4211 (1998).
3. M. E. Gaevski, S. O. Kognovitskiĭ, S. G. Konnikov, *et al.*, Nanotechnology, No. 11, 270 (2000).
4. A. V. Nashchekin, M. E. Gaevskii, S. O. Kognovitskiĭ, *et al.*, Inst. Phys. Conf. Ser. **169**, 119 (2001).

Translated by P. Pozdeev

Technical Physics Letters, Vol. 29, No. 6, 2003, pp. 480–484. Translated from Pis'ma v Zhurnal Tekhnicheskoĭ Fiziki, Vol. 29, No. 11, 2003, pp. 86–94.

Energy Band Diagram of a Photosensitive Sn–*p*-InSe Structure

S. I. Drapak, V. B. Orletskiĭ, Z. D. Kovalyuk, V. V. Netyaga, and V. D. Fotiĭ

Frantsevich Institute for Problems of Materials Science (Chernivtsy Department), National Academy of Sciences of Ukraine, Chernivtsy, Ukraine

e-mail: chimsp@unicom.cv.ua

"Photon-Quartz" Central Engineering Design Bureau, Chernivtsy, Ukraine

e-mail: photon@unicom.cv.ua

Revised manuscript received February 7, 2003

Abstract—Photosensitive Sn–*p*-InSe structures obtained by thermal deposition of Sn in vacuum onto thermally pretreated *p*-InSe substrates are well described within the framework of a MIS model with the insulating layer represented by a film of wide-bandgap γ-In_2Se_3 with E_g = 2.0 eV formed as a result of thermal treatment of the base semiconductor. *© 2003 MAIK "Nauka/Interperiodica".*

Indium monoselenide (InSe) belongs to a broad class of layered $A^{III}B^{VI}$ semiconductors. An important special feature of these materials is the possibility to obtain atomically smooth mirror substrates with a low number of dangling bonds on the surface by cleavage in air. This circumstance, together with increased stability with respect to irradiation, makes InSe an attractive base material for various photosensitive devices. Reported applications include photodiodes and polarized radiation sensors with a photopleochroism coefficient ≥90% [1, 2].

Despite a relatively large resistivity of the base material, the efficiency of InSe-based photoconverters reaches ≈6% for the *n*-type semiconductor (e.g., in Pt–InSe structures) [1] and up to 10–12% for the *p*-type material (in In_2O_3:Sn–InSe–Au structures) [3]. The latter values are only slightly lower as compared to the efficiency level achieved in the best elements based on currently popular Cu(InGa)Se_2 (CIGS) [4]. Extensive research now is aimed at reducing the cost of production of the photosensitive device structures based on InSe.

Below we report for the first time on the possibility of obtaining a rectifying photosensitive Sn–*p*-InSe junction. Previously, tin (possessing the same electron work function as that of *p*-InSe) has usually been employed as an ohmic contact formed by fusion or by some other application techniques different from the proposed technology [3, 5].

The experiments were performed on samples of InSe:Zn with a room-temperature majority carrier density of $p = 5 \times 10^{13}$ cm^{-3}. It was found that the current–voltage (*J–U)* characteristic of a Sn–*p*-InSe junction, prepared by thermal deposition of Sn in vacuum onto thermally pretreated semiconductor substrates, changes the character from ohmic to diode (Fig. 1, plots *1–3*). At a bias voltage of 1.5–2 V, the forward current exceeds the reverse current in this structure by a factor of about ten. The maximum current is observed when the bias voltage is applied with plus on the base semiconductor. In the region of forward bias $U > 2$ V, the *J–U* curve obeys the relation $U = U_0 + IR$. The cutoff voltage U_0 (frequently considered as the metal–semiconductor barrier height φ_B) at T = 293 K amounts to ~0.6 V. The barrier formation in this junction is confirmed by the character of noise: a reverse biased structure exhibits additional current noise, which is more than ten times higher than the noise in the same forward biased structure. At the same time, the barrier height determined by a photoelectric method amounts to ~1.07 eV (Fig. 2, curve *4*). Note that the Sn–*p*-InSe junction prepared by fusing metal into freshly cleaved semiconductor substrates in air retains the ohmic character at current densities up to $J \approx 2.5–5 \times 10^{-3}$ A/cm^2 (Fig. 1, curve *4*).

According to [6], the electron affinity of InSe (χ_{InSe}) cleaved in air decreases by 0.3 eV for the first 4 min and then only slightly varies within 1.5–2.5% during subsequent 72 h. Allowance for this "surface aging" does not elucidate the problem of obtaining a *J–U* curve with diode character, since a decrease in the electron work function of a *p*-type semiconductor during a period of time required for preparing a series of samples and conducting the experiment must be sufficient for the formation of an enriched layer in the Sn–*p*-InSe junction prepared by thermal deposition in vacuum.

As was noted above, junctions with rectifying properties (i.e., with a barrier layer) were observed between *p*-InSe and materials possessing greater electron work functions [3]. However, in that case, we could expect the forward current to pass under different conditions

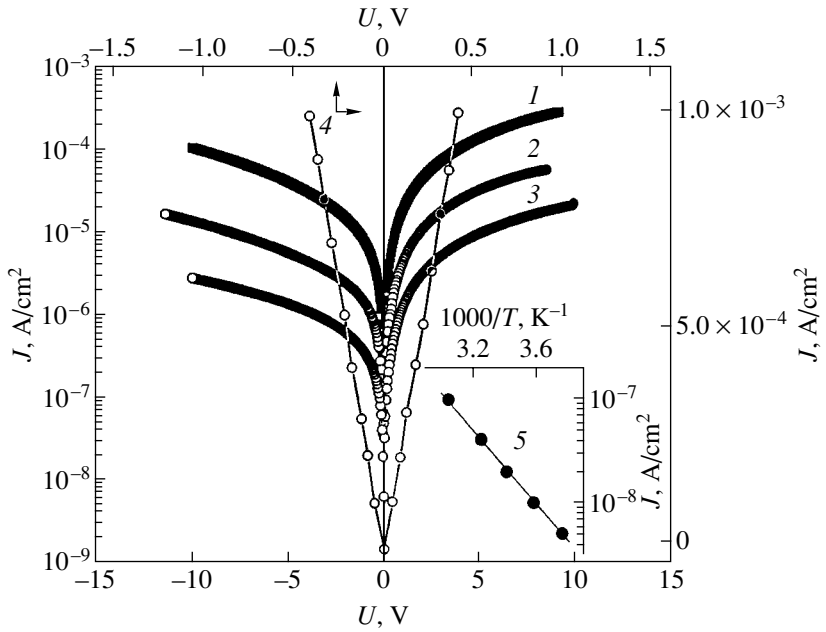

Fig. 1. Current–voltage characteristic of Sn–*p*-InSe junction prepared (*1–3*) by depositing Sn in vacuum onto thermally pretreated semiconductor substrates and (*4*) by fusing Sn into freshly cleaved semiconductor surface at $T = 328$ (*1*), 293 (*2*, *4*), and 266 K (*3*); the inset (*5*) shows the temperature dependence of a saturation beam current density for the former junction under forward bias conditions.

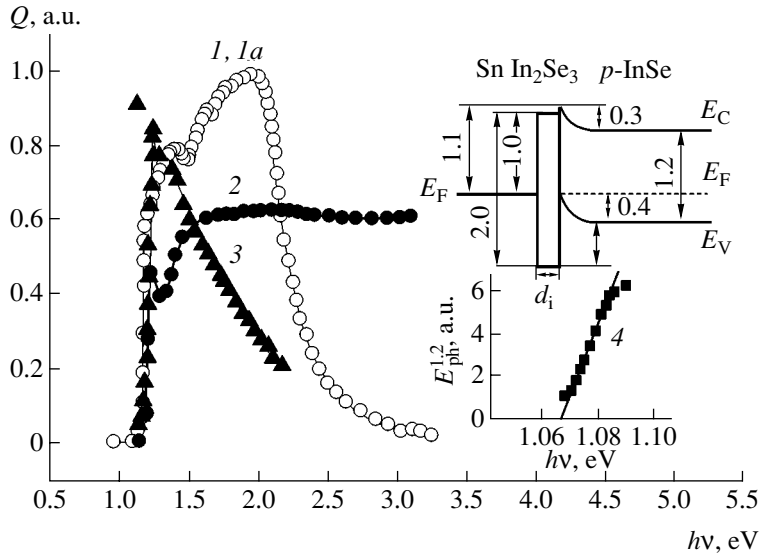

Fig. 2. Relative photoconversion quantum efficiency spectra of (*1*) Sn–*p*-InSe junction prepared by depositing Sn in vacuum onto thermally pretreated semiconductor substrates, (*1a*) Sn–In_2Se_3–*p*-InSe structure prepared by sequentially depositing In_2Se_3 and Sn onto *p*-InSe substrates; (*2*) single crystal *p*-InSe, and (*3*) InSe-based *p–n* junction. The bottom inset (curve *4*) shows a plot of the square root of the photoresponse per photon versus photon energy for the first junction; the top inset shows an energy band diagram of the Sn–*p*-InSe junction under equilibrium conditions (all energy differences are expressed in electronvolts).

(with minus on *p*-InSe), which contradicts the experiment.

The capacitance–voltage (*C–U*) characteristics of the junction under consideration are close to linear when plotted as $1/C^2 = f(U)$, but the capacitance cutoff reaches unreasonable values corresponding to a barrier height of 4–5 eV. This character of the *C–U* curves is typical of the structures with a high-ohmic layer at the interface [7]. A depleted layer with the capacitance independent of the applied voltage is also characteristic of the Mott diodes [5]. According to [8], Sn diffusion into layered semiconductors leads to the formation of a high-ohmic defect layer in the subsurface region, with

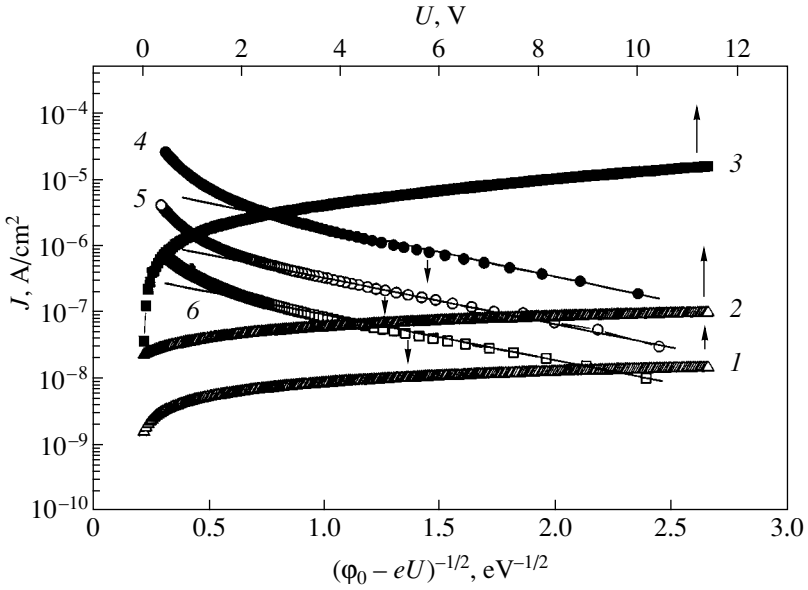

Fig. 3. Reverse branches of the current–voltage characteristic of Sn–*p*-InSe junction prepared by depositing Sn in vacuum onto thermally pretreated semiconductor substrates at T = 293 (*1–3*, *5*), 328 (*4*), and 266 (*6*): (*1*) calculation by formula (2) taking into account only the generation and recombination processes; (*2*) calculation by formula (3) taking into account diffusion processes leading to the formation of a Mott diode; (*3*) real current; (*4–6*) experimental reverse branches plotted in terms of expression (*4*).

a carrier density close to the intrinsic level. This accounts for the phenomenon of space-charge-limited current in the structures involving SnO_2. Indeed, taking into account the differential serial resistance, the forward branches of the *J–U* characteristic of the Sn–*p*-InSe junction under consideration must obey the relation $I \sim U^2$. However, the thickness of the high-ohmic layer estimated by the formula $J = \frac{9}{8}\varepsilon\varepsilon_0\mu_n\frac{S^2}{d^3}$ [5] (all notations are conventional) amounts to 30–40 μm which is more than ten times greater as compared to published data (1.5–2 μm) [8]. Since our junctions were prepared at temperatures lower than those reported in the literature (420–500°C), one may expect that d would decrease rather than increase.

If the Mott barrier were formed in the junction as a result of Sn diffusion, one would expect the charge transfer be determined by the process of diffusion and described by the equation

$$J = e\mu_p E p_0 \exp(-e\varphi_B/kT)(\exp(eU/kT) - 1), \quad (1)$$

where E is the electric field strength in the barrier and φ_B is the barrier height (other notations are as commonly accepted). The results of calculations of the reverse current density as a function of the applied voltage is presented in Fig. 3 (curve *2*). As can be seen, this dependence significantly differs from the behavior of a current really passing in the structure studied (Fig. 3, curve *3)*. In the calculation, φ_B was taken equal to U_0. In addition, the slope of the temperature dependence of U_0 differs from that of the temperature dependence of E_g in InSe by a factor of almost ten. finally, if the diffusion of Sn were responsible for the formation of an inversion layer with a thickness sufficient for localization of a space charge region on the *p*-InSe surface, one would expect the formation of two reverse switched barriers. However, this assumption contradicts the linearity of the *J–U* characteristic observed for the forward bias $U > 2$ V.

Recently Savchuk and Kytsay [9] reported that a thermal treatment of InSe at $T \le 300$°C led to the formation of a surface layer of In_2Se_3. The films of In_2Se_3 formed under such conditions (in contrast to a material used for the creation of In_2Se_3–InSe heterojunctions [10]) possessed a significantly greater resistivity than that of the base semiconductor [11]. Taking into account the difference between the room-temperature bandgaps of InSe and α (γ) modifications of In_2Se_3 (E_g = 1.2 eV against 1.45 (2.0) eV, respectively [12]), the film of In_2Se_3 formed in the Sn–*p*-InSe junction can be considered as insulating [5].

Additional evidence for the formation of a γ-like modification of In_2Se_3 on the InSe surface is provided by the short-wavelength boundary of photosensitivity of the junction under consideration, as can be seen in Fig. 2 (curve *1*) showing the photosensitivity spectrum measured in a sample structure illuminated from the side of a semitransparent Sn film and the insulating layer. In addition, Fig. 2 shows plots of the relative quantum efficiency $Q(h\nu)$ of a *p*-InSe single crystal (curve *2*) and a *p–n* junction in InSe (curve *3)* obtained by creating a temperature gradient between opposite surfaces of a *p*-type plate [1] (the sample was illumi-

nated from the side of a thin inversion layer). In order to check for the possibility that a thin In_2Se_3 film is formed on the surface of *p*-InSe as a result of heating, we have prepared a model sample by depositing an In_2Se_3 layer of controlled thickness onto the base semiconductor substrate. The $Q(h\nu)$ spectra of such model structures (Fig. 2, curve *1a*) fully coincided with those of the junction under consideration (curve *1*). Insignificant distinctions in the electrical properties are probably related to a difference in the density of charge carriers in the deposited films and those formed as a result of thermal treatment.

Thus, the Sn–*p*-InSe junction obtained by thermal deposition of Sn in vacuum onto a thermally pretreated *p*-InSe substrate can be considered as a metal–insulator–semiconductor (MIS) structure. According to [5], the current density in MIS structures is described by an expression

$$J = A^*T^2\exp(-e\varphi_B/kT) \times \exp(-\alpha_T\varphi_T^{1/2}d_i)\exp(eU/nkT), \quad (2)$$

where φ_B is the barrier height (i.e., the energy difference between the metal surface and the conduction band bottom of the insulator), φ_T is a tunneling barrier equal to the energy difference between the conduction bands of the base semiconductor and the insulator, and d_i is the insulator thickness; the term $\exp(-\alpha_T\varphi_T^{1/2}d_i)$ represents the tunneling probability (other notations are as commonly accepted). According to Eq. (1), the reverse current in structures with a small barrier height φ_B (whereby the semiconductor bands are bent downward and minority carriers are accumulated at the surface) is limited by the rate of electron production in the semiconductor bulk and behaves similarly to the current in a reverse biased *p*–*n* junction.

Figure 3 shows a theoretical dependence of the reverse current density on the applied voltage (curve *1*), which was calculated for $T = 293$ K taking into account only the generation and recombination processes and assuming that the levels are localized at the middle of the bandgap of the base semiconductor. The calculation was performed using the formula for a sharply asymmetric junction [13],

$$J_{gen} = \frac{en_i d}{\tau}\frac{\sqrt{E_g/2 - eU} - \sqrt{E_g/2}}{\sqrt{\varphi_0 - eU}}, \quad (3)$$

where $d = [2\varepsilon\varepsilon_0(\varphi_0 - eU)/e^2(N_a - N_d)]^{1/2}$ is the width of the space charge region, φ_0 is the barrier height (assumed equal to U_0), and τ is the minority carrier lifetime (this value was taken from [1, 3]).

As can be seen from Fig. 3, the real reverse current (curve *3*) significantly exceeds the result of theoretical calculation, which is evidence in favor of the tunneling character of the reverse current in the structure under consideration. Indeed, the reverse branches of the *J*–*U* curve in a sufficiently wide interval of reverse bias values can be described by the expression [5]

$$J = \frac{1}{s}a_1(-b_1/\exp\sqrt{\varphi_0 - eU}), \quad (4)$$

where b_1 is a parameter independent of the applied voltage U (this quantity depends on the junction parameters and the type of tunneling transitions) and a_1 is a parameter determined by the degree of occupation of the energy levels involved in the tunneling process. At high voltages, a steeper growth of the reverse current as compared to the values given by formula (4) can be related to the avalanche amplification of carriers as a result of the impact ionization [5]. Therefore, the junction under consideration corresponds to the case when holes are accumulated on the semiconductor surface.

An equilibrium band diagram of the Sn–*p*-InSe junction featuring the accumulation on the semiconductor surface is schematically depicted in the inset in Fig. 2. This diagram is constructed with an allowance of the "aging" of the InSe surface [6]; the position of the Fermi level in the base semiconductor was taken from [1, 3]. In our case (in contrast to Si-based MIS structures) the barrier height φ_B is equal to the energy difference between the metal surface and the conduction band bottom on the semiconductor surface. Under the assumption that the charge carrier density in the In_2Se_3 film is close to the intrinsic level, this barrier height well agrees with the value determined from the results of photoelectric measurements (Fig. 2, curve *4*). The energy difference between the valence bands of InSe and In_2Se_3 coincides with the cutoff voltage U_0 determined from the forward branch of the room-temperature *J*–*U* curve.

According to the proposed energy band diagram, the main contribution to the forward current is due to the majority carriers tunneling from semiconductor to metal [5], which is described by the second exponent in Eq. (1). The saturation current density in the forward biased junction depends on the temperature as $J_0 \sim \exp(-e\varphi_B/kT)$ (Fig. 1, curve *5*), while the barrier height estimated from the slope of this dependence amounts to ~0.58 eV, in good agreement with the U_0 value. The thickness of an In_2Se_3 layer, formed in the Sn–*p*-InSe junction obtained by thermal deposition in vacuum, as estimated using Eq. (1) was 153 Å. In the calculation, it was assumed that (i) φ_T in the structure studied (in contrast to that in Si-based structures [5]) corresponds to the energy difference between the conduction band bottom in the semiconductor bulk and on the surface and (ii) the probability of tunneling under this rectangular barrier is $P_T \cong \exp[-2(m^*/2\pi^2h^2)^{1/2}(e\varphi_T)^{1/2}d_i]$ [5]. Note that the tunneling transparency of relatively thick In_2Se_3 layers provides for a flexible control of parameters of the InSe-based MIS structures.

In conclusion, it should be also noted that the Sn–*p*-InSe junctions, even with nonoptimized thicknesses of

Sn and the base semiconductor, were characterized by a signal to noise ratio of not less than 300. This makes the proposed Sn–In_2Se_3–*p*-InSe structure a promising base for manufacturing cheap and technologically simple photodetectors for the visible and near IR spectral ranges.

REFERENCES

1. A. Segura, J. P. Guesdon, J. M. Besson, and A. Chevy, J. Appl. Phys. **54**, 876 (1983).
2. V. N. Katerinchuk and M. Z. Kovalyuk, Pis'ma Zh. Tekh. Fiz. **23** (10), 1 (1997) [Tech. Phys. Lett. **23**, 377 (1997)].
3. J. Martinez-Pastor, A. Segura, J. L. Valdes, and A. Chevy, J. Appl. Phys. **62** (4), 1477 (1987).
4. *E-MRS Spring Meeting 2002: Book of Abstracts* (Strasburg, 2002), pp. B2–B46.
5. S. Sze, *Physics of Semiconductor Devices* (Wiley, New York, 1981; Mir, Moscow, 1984), Vols. 1, 2.
6. V. L. Bakumenko and V. F. Chishko, Fiz. Tekh. Poluprovodn. (Leningrad) **11** (10), 2000 (1977) [Sov. Phys. Semicond. **11**, 1171 (1977)].
7. A. A. Lebedev and D. V. Davydov, Fiz. Tekh. Poluprovodn. (St. Petersburg) **34** (1), 113 (2000) [Semiconductors **34**, 115 (2000)].
8. C. Tatsuyama and S. Ichimura, Nuovo Cimento **38** (123), 352 (1977).
9. V. P. Savchuk and V. B. Kytsay, Thin Solid Films **361–362**, 124 (2000).
10. S. I. Drapak, Z. D. Kovalyuk, V. V. Netyaga, and V. B. Orletskiĭ, Pis'ma Zh. Tekh. Fiz. **28** (17), 1 (2002) [Tech. Phys. Lett. **28**, 707 (2002)].
11. S. I. Drapak, V. B. Orletskiĭ, Z. D. Kovalyuk, and V. V. Netyaga, Fiz. Tekh. Poluprovodn. (St. Petersburg) **37** (2), 196 (2003) [Semiconductors **37**, 187 (2003)].
12. C. Julien, M. Eddrief, M. Balkanski, *et al.*, Phys. Status Solidi A **88**, 687 (1985).
13. L. A. Kosyachenko, I. M. Rarenko, O. A. Bodnaruk, and Sun Veigura, Fiz. Tekh. Poluprovodn. (St. Petersburg) **33** (12), 1438 (1999) [Semiconductors **33**, 1293 (1999)].

Translated by P. Pozdeev

Technical Physics Letters, Vol. 29, No. 6, 2003, pp. 485–487. Translated from Pis'ma v Zhurnal Tekhnicheskoĭ Fiziki, Vol. 29, No. 12, 2003, pp. 1–6.

The Parameters of Laser Plasmas Formed Using Polycrystalline $CuInS_2$, Copper, and Indium Targets

A. K. Shuaibov and M. P. Chuchman

Uzhgorod National University, Uzhgorod, Ukraine

Received December 16, 2002

Abstract—We have studied the electron temperature (T_e) and density (N_e) of laser plasmas formed under the action of a neodymium laser in a polycrystalline $CuInS_2$ target, as well as in pure copper and indium targets. At a laser beam power density of ~10^8 W/cm^2, the average electron temperature of a laser plasma at a distance of r = 1 mm from the $CuInS_2$ target falls within 0.55–0.77 eV, while the laser plasmas of copper and indium are characterized by T_e(Cu) = 0.4–1.8 eV and T_e(In) = 0.58–2.4 eV, respectively. The average electron density at the core of the laser torch (r = 1 mm) at the $CuInS_2$ target reaches $N_e = 2.2 \times 10^{16}$ cm^{-3}. The results obtained for the polycrystalline target can be used in microelectronics for optimization of the process of laser deposition of thin films for solar cell elements. © *2003 MAIK "Nauka/Interperiodica".*

Previously [1–3], we studied the characteristics of laser plasmas formed under the action of a moderate-power neodymium laser upon Cu, In, Al, Ga, Sb, and some other metals and semiconductor targets, which allowed us to pass to the investigation of laser plasmas of more complex compositions [4, 5]. Plasmas generated by laser ablation of $CuInS_2(Se_2)$, $CuSbS_2(Se_2)$, $PbGa_2S_4$ and some other crystal targets are employed for the obtaining of thin-film elements of high-efficiency solar cells [6] and other photoelectron devices [7, 8]. In order to optimize the laser beam deposition technology [1, 2] for high-quality thin films of complex compositions, it is necessary to know the main parameters of the laser plasma—the electron density (N_e) and electron temperature (T_e)—in the region where the substance is deposited from the laser torch onto a substrate. The laser plasma characteristics can be determined by monitoring of the laser torch formed at a polycrystalline target. This quantitative diagnostics has to be performed by methods of optical spectroscopy with high temporal and spatial resolution.

Here we report the results of investigation of the electron temperature and density in a laser plasma formed during moderate-power laser ablation of a $CuInS_2$ target, as well as pure copper and indium targets.

The experiments were performed with $CuInS_2$ (polycrystalline charge), copper, and indium targets placed into a metal vacuum chamber evacuated to a residual pressure not exceeding 5–7 Pa. The laser plasma was generated by the beam of a pulsed-periodic laser focused on a target surface so as to provide for a laser radiation power density of (5–7) × 10^8 W/cm^2. The optical emission from the laser plasma was collected with the aid of a lens from two regions on the axis of a laser plasma torch, spaced by r = 1 and 7 mm from the target surface. The experimental conditions, setup, and procedure are described in more detail elsewhere [9, 10].

Figure 1 presents the energy distribution of the time-averaged populations of the excited states of atoms formed during the laser ablation of polycrystalline $CuInS_2$ and pure copper targets. Using the maximum likelihood method [11], we have drawn several lines passing through the experimental points. These lines exhibit several close slopes and reflect the energy conservation law: the higher the electron temperature, the lower the atomic energy level. The average electron temperature in a laser plasma for the polycrystalline target is T_e = 0.55–0.77 eV, while the plasmas obtained from pure metal targets are characterized by T_e(Cu) = 0.4–1.8 eV and T_e(In) = 0.58–2.4 eV. The lower electron temperature in the copper plasma as compared to that in the indium plasma can be explained by a more effective energy transfer from the surface to bulk in the former case due to the higher thermals conductivity of copper. The relatively low value and the narrow range of the $T_e(CuInS_2)$ values are probably related to a porous structure of the polycrystalline target.

Figure 2 shows the time variation of the electron temperature (in the copper plasma) and the electron density (in the indium plasma). The $T_e(t)$ curve for the copper plasma exhibits two peaks at which the electron temperature reaches T_e = 3 and 7 eV (Fig. 2a). The laser

1063-7850/03/2906-0485$24.00 © 2003 MAIK "Nauka/Interperiodica"

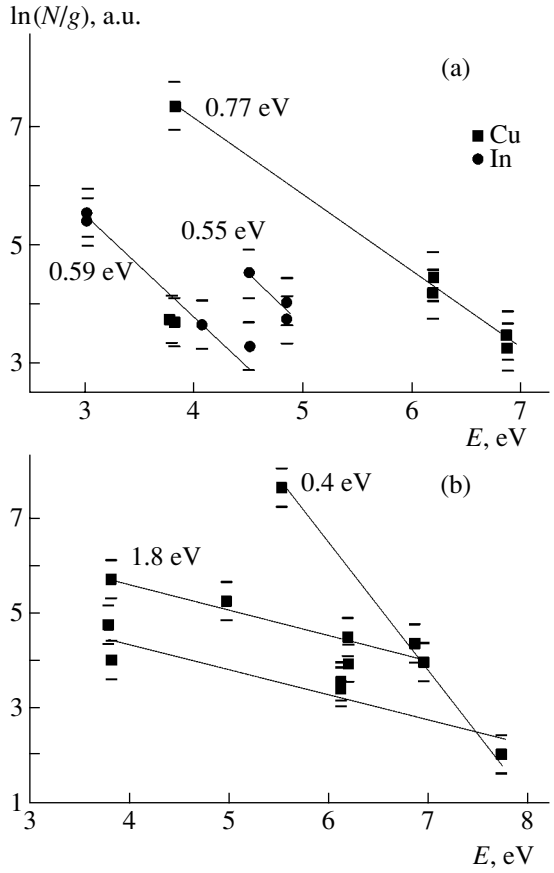

Fig. 1. The energy distribution of the time-averaged populations of the excited states of atoms formed during the laser ablation of (a) polycrystalline $CuInS_2$ and (b) pure copper targets (r = 7 mm).

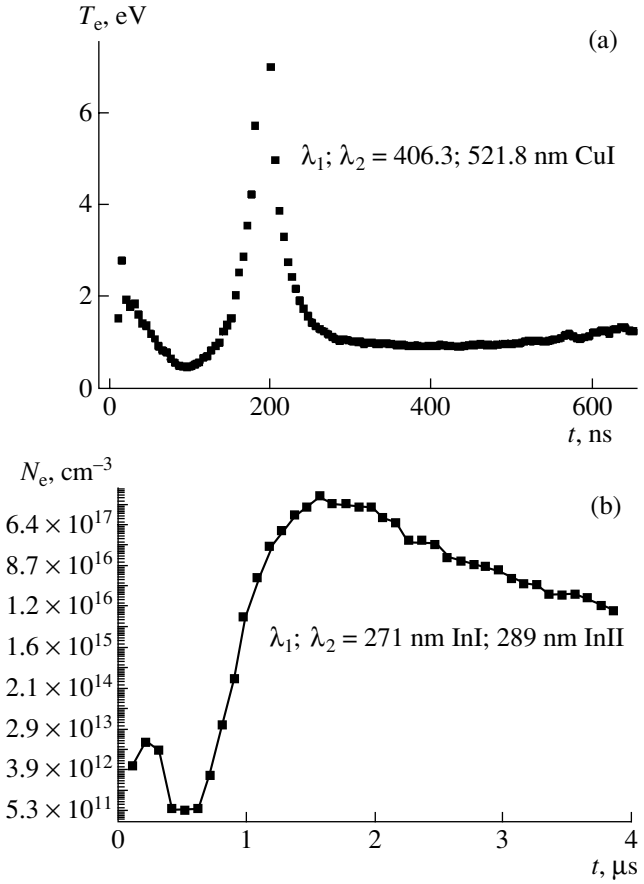

Fig. 2. Time variation of the (a) electron temperature T_e in the copper plasma for r = 1 mm and (b) the electron density in the indium plasma for r = 7 mm.

torch exhibited inversion of the level population at t = 300–500 ns for copper and t = 2–5 μs for indium. Estimates of the electron density, based on the average values of T_e (by data of Fig. 1), showed that $N_e(\text{In}) = 9.4 \times 10^{16}$ cm^{-3} (r = 1 mm) and 1.9×10^{16} cm^{-3} (r = 7 mm); $N_e(\text{Cu}) = 4.4 \times 10^{16}$ cm^{-3} (r = 7 mm); and $N_e(CuInS_2) = 2.2 \times 10^{16}$ cm^{-3} (r = 1 mm). On the $N_e(t)$ curve for the laser plasma of indium (Fig. 2b), the first peak in the electron density occurs between the fast front and the main fraction of ions. At the other maximum, appearing immediately behind the first ion emission peak, the electron density varies in the range from 10^{11} to 10^{18} cm^{-3}.

Thus, we have studied the parameters of laser plasmas formed during laser ablation of a polycrystalline $CuInS_2$ target and the targets of pure copper and indium. The data obtained by methods of optical spectroscopy with high temporal and spatial resolution showed that the average electron temperature in the plasma obtained by laser ablation of the $CuInS_2$ target is sufficiently homogeneous and falls within 0.55–0.77 eV; for pure metal targets, $T_e(\text{Cu}) = 0.4$–1.8 eV and $T_e(\text{In}) = 0.58$–2.4 eV, respectively (for r = 7 mm). The electron density in the laser plasma of the polycrystalline target is 2.2×10^{16} cm^{-3} (r = 1 mm), which is about half the value for the plasma at the copper torch center and is lower by a factor of 4.3 than the electron density in the indium plasma. The value of $N_e(\text{In})$ at r = 7 mm varies within 4 μs in the range from 10^{11} to 10^{18} cm^{-3}. These results can be used for optimization of the process of thin film deposition by laser ablation of polycrystalline $CuInS_2$ targets.

Acknowledgments. The authors are grateful to A.I. Dashchenko for his help in the study of optical emission from laser plasmas.

REFERENCES

1. A. K. Shuaibov, L. L. Shimon, A. I. Dashchenko, and M. P. Chuchman, Uzhgorod. Univ. Sci. Herald., Ser. Phys., No. 2, 348 (2000).
2. A. K. Shuaibov, L. L. Shimon, A. I. Dashchenko, *et al.*, Fiz. Plazmy **27**, 85 (2001) [Plasma Phys. Rep. **27**, 82 (2001)].

3. A. K. Shuaibov, A. I. Dashchenko, and I. V. Shevera, Teplofiz. Vys. Temp. **39**, 357 (2001).
4. A. K. Shuaibov, A. I. Dashchenko, and I. V. Shevera, Fiz. Plazmy **27**, 658 (2001) [Plasma Phys. Rep. **27**, 619 (2001)].
5. A. K. Shuaibov, L. L. Shimon, A. J. Dashchenko, *et al.*, J. Phys. Stud. **6** (2), 168 (2002).
6. T. Nakabayashi, T. Miyazawa, and K. J. Hashimoto, Solar Energy Mater. Solar Cells **49**, 375 (1997).
7. H. Sano, H. Hirasawa, S. Nakamura, *et al.*, Jpn. J. Appl. Phys., Part 1 **37**, 1760 (1998).
8. S. A. Kukushkin and A. V. Osipov, Usp. Fiz. Nauk **168** (10), 1083 (1998) [Phys. Usp. **41**, 107 (1998)].
9. A. K. Shuaibov, L. L. Shimon, A. I. Dashchenko, and M. P. Chuchman, Ukr. Fiz. Zh. **46** (11), 1144 (2001).
10. I. É. Kacher, A. K. Shuaibov, and A. I. Dashchenko, Prib. Tekh. Éksp. **44** (5), 152 (2001).
11. G. A. Korn and T. M. Korn, *Mathematical Handbook for Scientists and Engineers* (McGraw-Hill, New York, 1961; Nauka, Moscow, 1977).

Translated by P. Pozdeev

Technical Physics Letters, Vol. 29, No. 6, 2003, pp. 488–490. Translated from Pis'ma v Zhurnal Tekhnicheskoĭ Fiziki, Vol. 29, No. 12, 2003, pp. 7–13.

Local Migration of Grain Boundaries in Polycrystalline Materials under Plastic Deformation Conditions

A. L. Kolesnikova, I. A. Ovid'ko*, and A. A. Fedorov

Institute for Problems of Mechanical Engineering, Russian Academy of Sciences, St. Petersburg, Russia

** e-mail: ovidko@def.ipme.ru*

Received December 18, 2002; in final form, February 7, 2003

Abstract—We propose a theoretical model describing the local migration of grain boundaries (GBs) near triple junctions according to the new mechanism stimulated by the GB slip. Within the framework of this model, a driving force for the local migration is due to the interaction between sliding and structural GB dislocations responsible for the GB slip and misorientation, respectively. *© 2003 MAIK "Nauka/Interperiodica".*

The triple junctions of grain boundaries (GBs) in polycrystalline materials possess a structure and properties different from those of the adjacent GBs (see, e.g., [1–8]). In plastically deformed materials, such triple junctions act as the sources of lattice dislocations [6, 8], provide for enhanced diffusion creep [4, 5], stimulate the nucleation of microcracks [2, 3], and hinder the motion of lattice and GB dislocations [7, 8]. In particular, the behavior of triple junctions produces a determining influence on the superplasticity of polycrystalline materials. Indeed, the superplastic straining takes place primarily through the GB slip, that is, through the motion of GB dislocations (GBDs) for which the triple junctions act as obstacles [7, 8].

Recently [9], Astanin *et al.* [9] discovered the phenomenon of local migration of GBs near triple junctions, which is stimulated by the GB slip and, in turn, significantly facilitates this slip. This effect is considered as one of the dominating factors for the superplasticity in polycrystalline materials [9, 10] and for the localization of deformation in nanocrystalline materials [7]. According to the model proposed in [9], the driving force for this migration is the elastic energy released due to increased distances between sliding GBDs in their pileups formed at the triple junctions. However, the above model [9] does not take into account the effect of structural GBDs (geometrically necessary to provide for the GB misorientation) on the local migration. The latter dislocations can play a very important role in the process of GB transformations (see. e.g., [1, 11–14]).

The main purpose of this study was to construct a theoretical model describing the local migration of GBs stimulated by the GB slip, with allowance for the elastic interaction between the sliding and immobile GBDs.

Consider a triple junction formed by three radial walls of structural dislocations (with the Burgers vectors perpendicular to the corresponding GB planes) in an infinite cylinder of radius R (Fig. 1a). Each wall contains N_i dislocations occurring at a distance of h_i from each other and possessing the Burgers vectors $\mathbf{b}_{(i)}$, $i = 1$, 2, 3 (here and below, the indices in parentheses refer to the wall number). Thus, the nearest dislocations occur at a distance of $h_{(i)}/2$ ($i = 1, 2, 3$) from the triple junction. The dihedral angles $\alpha_{(1–2)}$, $\alpha_{(2–3)}$, and $\alpha_{(3–1)}$ between the corresponding GB (see Fig. 1a) in the initial state are assumed to be the same and equal to 120°. In order to simplify calculations and the analysis of results, the triple junction of tilt boundaries is assumed to be compensated, whereby $\sum_{i=1}^{3} \varphi_i = 0$, where $b_{(1)} = b_{(2)} = b$, $b_{(3)} = 2b$ and the misorientation angle is $\varphi_{(i)} \approx b_{(i)}/h_{(i)} \le 0.2$. Here, the sense of dislocations in wall 3 is opposite to that in walls 1 and 2.

The elastic energy of the system of dislocations per unit length of the cylinder (Fig. 1a) is given by the formula [15]

$$E^{el} = -\frac{1}{2} \int\limits_{S_{cyl}/S_{core}} \beta_{kl}^{*} \sigma_{kl} dS', \qquad (1)$$

where β_{kl}^{*} is the total plastic distortion of dislocations, σ_{kl} is the elastic stress field of dislocations in the system, and the integration is performed over the cross section area of the cylinder (S_{cyl}) bypassing the dislocation core (S_{core}).

The plastic distortion of an individual dislocation was determined using the well-known Mura relation [15],

$$\beta_{kl}^{*disl} = -b_l \delta_k(S), \qquad (2)$$

where b_l is the Burgers vector of the lth dislocation and $\delta_k(S)$ is the Dirac delta on the surface of the displacement jumps (S) [15].

1063-7850/03/2906-0488$24.00

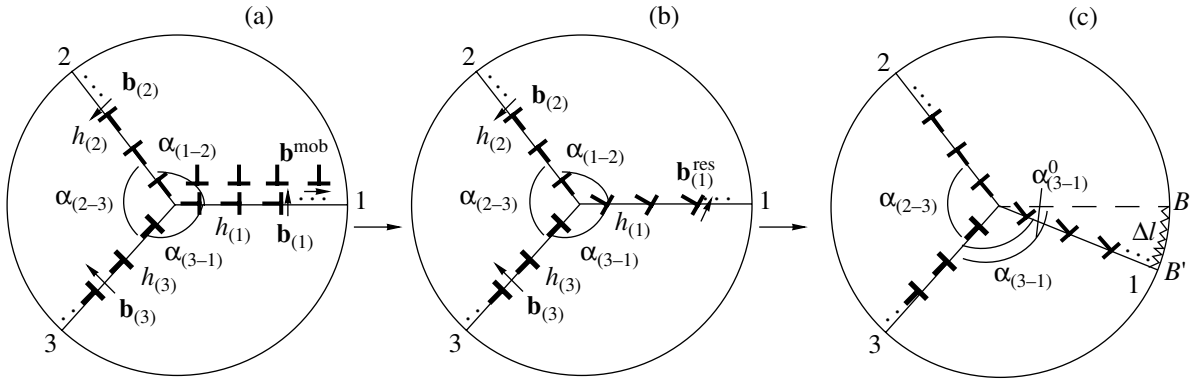

Fig. 1. Schematic diagram illustrating the triple junction of GBs in a cylinder: $\alpha_{(1-2)}$, $\alpha_{(2-3)}$, and $\alpha_{(3-1)}$ are the dihedral angles between GBs; h_i (i = 1, 2, 3) is the distance between immobile (structural) GBDs in the ith GB; (a) a pileup of sliding GBDs stopped by the triple junction at GB1; (b) the ensemble of sliding and structural GBDs is equivalent to the ensemble of dislocations with the Burgers vectors $\mathbf{b}_1^{\mathrm{res}}$; (c) local migration of GB1.

The elastic stress field $\sigma_{kl}^{\mathrm{disl}}$ of an edge dislocation in the cylinder with the *Oz* axis can be expressed in terms of the stress function χ^{disl} using the following relations:

$$\sigma_{xx} = \frac{\partial^2\chi^{\mathrm{disl}}}{\partial^2 y}, \quad \sigma_{yy} = \frac{\partial^2\chi^{\mathrm{disl}}}{\partial^2 x}, \quad \sigma_{xy} = -\frac{\partial^2\chi^{\mathrm{disl}}}{\partial y\partial x}. \quad (3)$$

For a dislocation with the Burgers vector $\mathbf{b} = b\mathbf{e}_x$, situated at the point x_0 on the *Ox* axis, the stress function (in the linear approximation) is

$$\chi^{\mathrm{disl}}(\mathbf{b} = b\mathbf{e}_x) = -\frac{Gby}{4\pi(1-\nu)}$$
$$\times\left[\frac{-(R^2-x_0^2)(x_0^2(x^2+y^2)+R^2(x^2-2xx_0+y^2))}{R^2((R^2-x_0x)^2+x_0^2y^2)}\right. \quad (4)$$
$$\left. + \ln\frac{R^2((x-x_0)^2+y^2)}{(R^2-x_0x)^2+x_0^2y^2}\right].$$

For a dislocation with the Burgers vector $\mathbf{b} = b\mathbf{e}_y$, situated at the point x_0 on the *Ox* axis, the stress function in the same approximation is

$$\chi^{\mathrm{disl}}(\mathbf{b} = b\mathbf{e}_y) = -\frac{Gb}{4\pi(1-\nu)}$$
$$\times\left[\frac{x_0(x^2+y^2)}{R^2}\right.$$
$$-\frac{(R^2-x^2-y^2)((x_0^2+R^2)x-x_0(R^2+x^2+y^2))}{(R^2-x_0x)^2+x_0^2y^2} \quad (5)$$
$$\left. + (x_0-x)\ln\frac{R^2((x-x_0)^2+y^2)}{(R^2-x_0x)^2+x_0^2y^2}\right].$$

Here, G is the shear modulus and ν is the Poisson ratio. Note that expressions (4) and (5) are obtained through a limiting transition from the stress function for a dipole of the edge disclinations [16] oriented along *Oy* or *Ox* axis. Using relations (3)–(5), one can determine elastic stresses for a dislocation situated at the point with the coordinates (x_0, y_0) and the Burgers vector oriented arbitrarily in the *xOy* plane of the cylinder cross section.

Let us consider the process of GB slip along GB1 through the motion of GBDs with the Burgers vectors $\mathbf{b}^{\mathrm{mob}}$ parallel to the GB1 plane (Fig. 1a). Since the triple junction is an obstacle to the motion of dislocations, the GBDs stop to form a planar pileup at this junction. In order to analyze the influence of these dislocations on the behavior of GB1, let us assume in the first approximation that the GBDs are stopped exactly at the positions of structural dislocations of GB1. Then the total stress field of all dislocations in GB1 is described as a superposition of the stress fields of $N_{(1)}$ dislocations with the Burgers vectors $\mathbf{b}_{(1)}^{\mathrm{res}} = \mathbf{b}_{(1)} + \mathbf{b}^{\mathrm{mob}}$ occurring in the positions of structural dislocations (Fig. 1b).

The elastic energy of a model dislocation configuration on GB1 is minimized upon the GB displacement to a position in which the Burgers vector $\mathbf{b}_{(1)}^{\mathrm{res}}$ is perpendicular to the GB plane. However, we must also take into account the elastic interactions of the dislocations in GB1 with the structural dislocations in GB2 and GB3, as well as the restrictions imposed on the GB motions in real materials. In our model, the latter factor is described as the pinning of point *B* in GB1 on the free cylinder surface, with an increase in the GB length by Δl (the length of segment *BB*' on the cylinder surface) in the course of GB1 migration (Fig. 1c).

In order to determine the angle $\alpha_{(3-1)}^{\mathrm{opt}}$ characterizing the local migration, let us calculate the elastic energy E

Dihedral angles $\alpha^{opt}_{(3-1)}$ characterizing the local migration of GB1 for various numbers of dislocations $N_{(1)}$ ($\alpha^{wall}_{(3-1)}$ is the angle at which a mobile GB becomes the ideal dislocation wall)

$N_{(1)}$	$\alpha^{opt}_{(3-1)}$, deg	$\alpha^{wall}_{(3-1)}$, deg
3	120 ± 1	75
4	112 ± 1	
5	100 ± 1	
6	95 ± 1	

of the system of dislocations as a function of the angle of deviation of the modified wall 1 ($\alpha_{(3-1)}$ in Fig. 1b) at a given initial angle ($\alpha^{0}_{(3-1)}$) and the initial system parameters (N, h, $\alpha_{(2-3)}$). Then, the optimum angle $\alpha^{opt}_{(3-1)}$ is determined from the condition

$$E(\alpha^{opt}_{(3-1)}) = \min\{E(\alpha_{(3-1)}) + \Delta E\}, \quad (6)$$

where $\Delta E = \gamma \Delta l$ is a change in the GB energy related to the increase in the GB length due to the local migration (γ is the specific surface energy of the GB).

We have used formulas (1)–(6) to calculate the dihedral angles $\alpha^{opt}_{(3-1)}$ between GB1 and GB3 for the following characteristic values of the parameters (see table): the initial dihedral angles between GBs 1 and 2, 2 and 3, and 3 and 1, $\alpha_{(1-2)} = \alpha_{(2-3)} = \alpha^{0}_{(3-1)} = 120°$; the number of dislocations in immobile GBs, $N_{(2)} = N_{(3)} = 3$; the distance between dislocations in immobile GBs, $h_{(2)} = h_{(3)} = 5b$; the Burgers vectors of dislocations in GB1 and GB2 and in the pileup, $b_{(1)} = b_{(2)} = b^{mob} = 0.1$ nm; the Burgers vector of dislocations in GB3, $b_{(3)} = 0.2$ nm; the specific surface energy (for aluminum), $\gamma = 0.6$ J/m^2; and $G = 26.5$ GPa. The table also presents the values of $\alpha^{wall}_{(3-1)}$, the angle at which a mobile GB becomes the ideal dislocation wall.

As the dislocation density in GB1 increases, the elastic energy of the system becomes comparable with the surface energy and GB1 tends to occupy a position in which dislocations with the Burgers vectors $\mathbf{b}^{res}_{(1)}$ form the ideal dislocation wall. The GB rotation from the initial position, $\alpha^{0}_{(3-1)} - \alpha^{opt}_{(3-1)}$, amounts to ≈20° and 25° for the number of dislocations $N_{(1)} = 5$ and 6, respectively. These values are close to those observed in experiment [9] for aluminum tricrystals.

Thus, the GB slip stimulates the local migration of GBs near the triple junctions. The driving force for this migration is the decrease in the elastic energy of the ensemble of structural GBDs and sliding GBDs stopped at the triple junctions.

Acknowledgments. This study was supported by the Russian Foundation for Basic Research (project no. 01-02-16853), the Volkswagen Foundation (project no. 05019225), and the Office of US Naval Research (grant N00014-01-1-1020).

REFERENCES

1. V. V. Rybin, *Large Plastic Deformation and Fracture of Metals* (Metallurgiya, Moscow, 1986).
2. I. M. Zhukovskiĭ and V. V. Rybin, Fiz. Tverd. Tela (Leningrad) **20** (6), 1829 (1987) [Sov. Phys. Solid State **20**, 1056 (1987)].
3. M. Yu. Gutkin and I. A. Ovid'ko, Philos. Mag. A **70**, 561 (1994).
4. A. A. Fedorov, M. Yu. Gutkin, and I. A. Ovid'ko, Scr. Mater. **47**, 51 (2002).
5. V. V. Rabukhin, Poverkhnost, No. 7, 126 (1986).
6. K. Owusu-Boahen and A. H. King, Acta Mater. **49**, 237 (2001).
7. H. Hahn and K. A. Padmanabhan, Philos. Mag. **76**, 559 (1997).
8. A. A. Fedorov, M. Yu. Gutkin, and I. A. Ovid'ko, Acta Mater. **51**, 887 (2003).
9. V. V. Astanin, A. V. Sisanbaev, A. I. Pshenichnyuk, and O. A. Kaibyshev, Scr. Mater. **36**, 117 (1997).
10. O. A. Kaibyshev, Mater. Sci. Forum **304-206**, 21 (1999).
11. M. Yu. Gutkin and I. A. Ovid'ko, Phys. Rev. B **63**, 064515 (2001).
12. S. V. Bobylev, I. A. Ovid'ko, and A. G. Sheinerman, Phys. Rev. B **64**, 224507 (2001).
13. V. V. Rybin and A. A. Zisman, Probl. Prochn. **3**, 70 (1985).
14. M. Yu. Gutkin, I. A. Ovid'ko, and N. V. Skiba, Pis'ma Zh. Tekh. Fiz. **28** (10), 78 (2002) [Tech. Phys. Lett. **28**, 437 (2002)].
15. T. Mura, *Micromechanics of Defects in Solids* (Martinus Nijhoff, Boston, 1987), p. 587.
16. V. I. Vladimirov and A. E. Romanov, *Disclinations in Crystals* (Nauka, Leningrad, 1986), p. 224.

Translated by P. Pozdeev

Technical Physics Letters, Vol. 29, No. 6, 2003, pp. 491–493. Translated from Pis'ma v Zhurnal Tekhnicheskoĭ Fiziki, Vol. 29, No. 12, 2003, pp. 14–20.

Nanosecond Pressure Pulses Propagating at Anomalously High Velocities in Metal Foils

Yu. V. Sud'enkov and A. I. Pavlishin

St. Petersburg State University, St. Petersburg, Russia

Received December 23, 2002

Abstract—We have studied the process of nanosecond compression pulse propagation in metal (aluminum, copper, and steel) foils. It was found that the compression pulse velocity in the foil may significantly exceed the longitudinal sound velocity in the corresponding bulk material. The results emphasize the necessity of very carefully interpreting the data for submicrosecond and shorter impact loading. The presence of a sufficiently long nonstationary shock wave process at the surface subjected to a short impact perturbation (with the wave characteristics significantly differing from those of a steady-state wave process) requires a more detailed analysis of the mechanism of shock wave formation in solids taking into account their discrete structures.

The past two decades showed increased interest in investigations of the behavior of materials under the action of intense energy fluxes. In particular, considerable effort is devoted to the study of shock wave processes in materials subject to the short-duration action of particle or electromagnetic radiation beams. For example, the effect of laser radiation pulses with durations of $\sim 10^{12}$–10^{-8} s was studied in [1–4]. Experiments of this kind are usually performed with thin film samples (10–100 μm thick), and the results are interpreted in terms of the Rankine–Hugoniot relations or within the framework of the acoustic approximation.

However, the correctness of this approach to analysis of the results of the aforementioned investigations is subject to serious doubt. There are sufficient grounds to believe that the parameters measured in these experiments (typically, the perturbation propagation velocity, less frequently, together with the free surface velocity) characterize rather a nonstationary shock wave process caused by a strongly nonequilibrium perturbation of the medium. This is related to the fact that the characteristic wavelengths of the impact pulses used in these cases are comparable with the scale of a material microstructure and, sometimes, with the sample dimensions. Moreover, it is known that the time of relaxation of a nonequilibrium spectrum can be on the same order of magnitude as the duration of perturbation or even exceed it [5].

In some experiments, the shock wave processes observed in thin layers and at the surface of samples subject to submicrosecond impact loading exhibited important peculiarities. In particular, it was found [6–8] that the velocity of propagation of short compression pulses may differ from equilibrium sound velocities, and it was established [9] that the time of relaxation of a nonequilibrium phonon spectrum may exceed $(2–4) \times 10^{-8}$ s.

The above peculiarities stimulated us to study the parameters of shock wave packets propagating in metal foils loaded by nanosecond compression pulses.

The nanosecond compression pulses were generated by a laser operating at $\lambda = 1.06$ μm, a pulse duration of 0.2 ns, and a pulse energy of ~0.25 mJ. The scheme of the experiment is depicted in Fig. 1. According to this scheme, a metal foil sample *2* was placed with an acoustic contact between piezotransducer *1* and the aluminum-coated side of a 5-μm-thick metallized Dacron film *3*. All this sandwich structure was pressed against plate *4* made of an optical glass. A depolished glass sheet in front of plate *4* ensured a relatively uniform illumination of the sample, with a laser spot diameter of about 6 mm. For the laser energy density deposited at the sample surface, the estimates based on the Mie–Grüneisen equation of state with allowance for the reflection and thermal conductivity coefficients showed that the level of pressures in the excitation zone is $p <$ 20 MPa, that is, below the elastic limits of the metals studied.

The laser-induced compression pulses were detected by piezotransducer *1* representing a 100-μm-thick PVDF film loaded on a wave impedance of $R =$ 50 Ω. The pressure sensor operated in a short-circuit regime ensuring a time resolution as high as ~0.5 ns. A part of the laser radiation was fed to a photodetector, whose output signal provided for the synchronization with a TDS-754C oscillograph (a 500-MHz bandwidth of which essentially determined the time resolution of the system).

Figure 1b shows typical oscillograms of the output signals of the photodetector and piezotransducer. In the time series of the pressure sensor, signal *1* represents

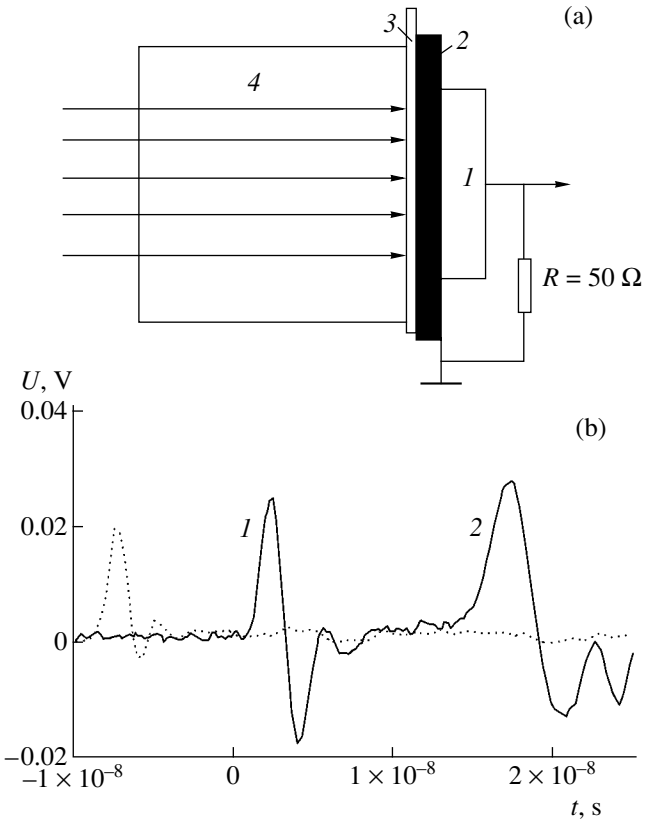

Fig. 1. (a) A scheme of the experiment; (b) typical oscillograms of the output signals from (solid profile) photodetector and (dashed profile) piezotransducer upon impact loading of an aluminum foil (h = 65 μm).

the compression pulse passing once through the sample and signal *2* corresponds to the compression pulse traveling two times across the sample. By measuring the delay time between these signals and using the known sample thickness h, it was possible to determine with sufficiently high accuracy the average velocity of the nanosecond pulse propagation in the materials studied. Note that these measurements involve no error related to the signal delay in the electronic circuitry; the error of measurements did not exceed 2.5%.

The values of the propagation velocity (c_{exp}) of a nanosecond compression pulse, calculated using the signal delay time, in comparison to the longitudinal sound velocities (c_1) in the metal foils studied are listed in the table. As can be seen from these data, the experimentally measured velocities of propagation of the nanosecond compression pulses significantly exceed the longitudinal sound velocities in all metals studied. Using these values of the pulse propagation velocity and the parameters of the shock wave adiabate for metals [10], we obtain the following estimates for pressures in the samples: $p \sim 82$ GPa (aluminum), ~72 GPa (copper), and ~46 GPa (steel). However, if these were real pressures, the mechanical energy in the wave would be three to four orders of magnitude greater than the laser radiation energy (even without reflection losses).

The nanosecond compression pulse propagation velocity (c_{exp}), the longitudinal sound velocities (c_1), and the characteristic transient process times in metal foils

	h, μm	c_{exp}, m/s	c_1, m/s	τ, ns
Al	65	9770 ± 230	6400	60
Cu	50	7140 ± 170	4700	35
Steel	20	6560 ± 160	5600	20

Thus, we have to admit that we are dealing with a nonstationary shock wave process featuring high pressure gradients at the surface subject to a nanosecond impact excitation. The parameters of this process cannot be described within the framework of a hydrodynamic or acoustic model. An analysis of the time series of the compression pulses presented in Figs. 2a–2c shows evidence of the strong influence of dispersion on these time profiles. Apparently, it is the dispersion that determines the character and the time of transition from a nonstationary process to the steady-state shock wave process with a constant longitudinal sound velocity c_1.

As in most other transient processes, the velocity of the pulse propagation as the function of time can be described by the equation

$$c(t) - c_1 = c(0)*\exp(-t/\tau) \quad \text{or}$$
$$c(t) - c_1 = -\tau*dc(t)/dt,$$

where c_0 is the initial value of the pulse propagation velocity upon a strongly nonequilibrium perturbation and τ is the characteristic time of the transient process. Assuming that the time shift of the compression pulse maximum (see Figs. 2a–2c) is determined by the change (Δc) in the propagation velocity during the time (Δt) required to travel across the sample, and taking approximately $dc(t)/dt \sim \Delta c/\Delta t$, we can estimate the characteristic times of transient processes in the metals studied. These estimates are given in the last column of the table. As can be seen, the characteristic times of transient processes in the system studied exceed 10^{-8} s. For these relaxation times, the nonstationary process in these metals will be manifested at distances on the order of $(0.1–0.5) \times 10^{-3}$ m from the surface subject to the impact loading.

It should be noted that these values of τ agree in the order of magnitude with the characteristic times reported for the manifestation of the shock wave processes in solids upon submicrosecond impact loading [7, 8], as well as with the time of the spontaneous decay of high-frequency phonons [9]. The results presented in this paper, together with the data reported in [7, 8], emphasize the necessity of very carefully interpreting the data for submicrosecond and shorter impact loading. The presence of a sufficiently long nonstationary

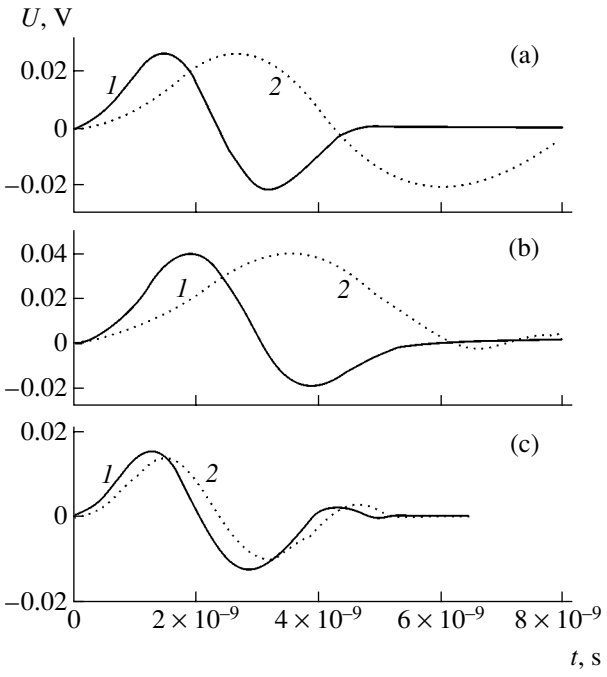

Fig. 2. Matched time series showing the first and second compression pulses in various foils: (a) Al (h = 65 μm); (b) Cu (h = 50 μm); (c) steel (h = 20 μm).

shock wave process at the surface subjected to a short impact perturbation with the wave characteristics significantly differing from those of a steady-state wave process requires a more detailed analysis of the mechanism of shock wave formation in solids taking into account their discrete structures.

We believe that the nonstationary character of the shock wave process at the impact surface is related to a strongly nonequilibrium anisotropic excitation of quasilongitudinal and quasitransverse modes in the oscillation spectrum of a solid subject to high-rate impact loading. The high perturbation propagation velocities are probably caused by the nonlinear response of these "overexcited" modes. At relatively low pressures, it is the dispersion (related to the energy redistribution between the oscillation modes) that determines the time of transition from a nonstationary to steady-state shock wave process descried within the framework of the acoustic approximation.

In the case of a high impact pressure, the dominating role of nonlinearity leads to the formation of a shock wave described by the hydrodynamic model. Here, the characteristic times of the transient process can be significantly smaller than the values obtained in our experiments. This can be related to an increase in the rate of energy redistribution caused by increasing anharmonicity of the intermode interaction. Naturally, these assumptions concerning the mechanism, driving forces, and character of the nonstationary shock wave process require additional investigation.

Acknowledgments. This study was supported by the Russian Foundation for Basic Research (project no. 01-02-00233) and by the Federal Program "Universities of Russia."

REFERENCES

1. L. M. Lyamshev, *Radiation Acoustics* (Nauka, Moscow, 1996).
2. K. J. Trainor and J. W. Shaner, Phys. Rev. Lett. **42**, 1154 (1979).
3. D. L. Paisley, D. C. Swift, R. P. Johnson, *et al.*, in *Proceedings of the Conference "Shock-Compression of Condensed Matter," Atlanta, Georgia, June 24–29, 2001*, p. 1343.
4. D. S. Moore, D. J. Funk, K. T. Gahagan, *et al.*, in *Proceedings of the Conference "Shock-Compression of Condensed Matter," Atlanta, Georgia, June 24–29, 2001*, p. 1333.
5. J. W. Tucker and V. W. Rampton, *Microwave Ultrasonics in Solid State Physics* (North-Holland, Amsterdam, 1972; Mir, Moscow, 1975).
6. G. Thomsen, I. Strait, Z. Vargeny, *et al.*, Phys. Rev. Lett. **53**, 989 (1984).
7. Yu. V. Sud'enkov, Pis'ma Zh. Tekh. Fiz. **9** (12), 1418 (1983) [Sov. Tech. Phys. Lett. **9**, 609 (1983)].
8. O. D. Baĭzakov and Yu. V. Sud'enkov, Pis'ma Zh. Tekh. Fiz. **11** (10), 1433 (1985) [Sov. Tech. Phys. Lett. **11**, 591 (1985)].
9. A. A. Maksimov and I. I. Tartakovskiĭ, Pis'ma Zh. Éksp. Teor. Fiz. **42** (11), 458 (1985) [JETP Lett. **42**, 568 (1985)].
10. *Shock Waves and High-Energy States of Substance*, Ed. by V. E. Fortov, L. V. Al'tshuler, R. F. Trunin, and A. I. Funtikov (Nauka, Moscow, 2000), p. 424.

Translated by P. Pozdeev

Technical Physics Letters, Vol. 29, No. 6, 2003, pp. 494–495. Translated from Pis'ma v Zhurnal Tekhnicheskoĭ Fiziki, Vol. 29, No. 12, 2003, pp. 21–24.

Dislocation Mechanism of Nanotube Formation

A. V. Pokropivny and V. V. Pokropivny

Institute for Problems of Materials Science, National Academy of Sciences of Ukraine, Kiev, Ukraine

e-mail: pokr@ipms.kiev.ua

Received December 25, 2002

Abstract—We propose a dislocation mechanism explaining the formation of multi- and single-sheet nanotubes and a disclination mechanism accounting for the formation of nanocones. According to the proposed mechanism, rolling up a graphite sheet gives rise to elastic stresses which are released through the slippage of dislocations with edge and screw components. Each closure of the sheet proceeds by a zipper mechanism and results in the formation of a single-sheet nanotube. The number of dislocation slippages is equal to the number of layers in a multisheet nanotube. © *2003 MAIK "Nauka/Interperiodica".*

The mechanisms responsible for the formation of nanotubes and nanocones are still unclear. There are several possible mechanisms for the formation of these structures, including the open- and closed-end growth, sequential and simultaneous growth of shells and nanotubes, rolling up of a graphite sheet, etc. (see reviews [1–4]). Amelinckx *et al.* [5] paid attention to the formation of dislocations in a multisheet nanotube and proposed a mechanism for the growth of nanotubes whereby graphite sheets are layered over the seeding nanotube and the dislocations only play the role of an energy stabilizer in this system.

Below, we propose an alternative, dislocation mechanism for the formation of nanotubes and a disclination mechanism for the formation of nanocones.

Previously [2], it was demonstrated that a nanotube can form as a result of rolling up an extended graphite sheet so as to connect the long edges. Probably, this mechanism can be operative during the formation of single-sheet nanotubes or cones in the presence of a metal, whereby metal atoms adsorbed on the surface would prevent the sheet from bending further.

According to the proposed mechanism, a graphite sheet is not closed immediately upon making one turn (Fig. 1a), but continues to roll further (Fig. 1b) as a result of heating or under the action of external stresses (e.g., during indentation). As a result, the graphite sheet forms a tubular spiral roll (Fig. 1c) held together by van der Waals forces. The essence of the mechanism is as follows. When the elastic stresses exceed the level necessary for the motion of dislocations (disclinations), the latter exhibits slippage, whereby the planes of graphite layers shift in the direction of vector $\bar{\mathbf{c}}$ (i.e., along the radius of the spiral, as indicated by the arrow in Figs. 1c–1e). Every motion of the dislocation (possessing in the general case both edge and screw components) leads to the formation of one nanotube (Fig. 1d). The closure of the rolled sheet probably proceeds by a zipper mechanism (Fig. 2a–2d). The number of dislocation slippages is equal to the number of sheets in the resulting nanotube. When the dislocation escapes at the surface of the roll, the slippage ceases and a multisheet nanotube is formed. (Fig. 1e).

If the dislocation ceases to move, but the inner edge of the sheet continues to roll, the conditions of dislocation slippage will arise again. Eventually, the dislocation will escape at the surface, but in a different place. When both the dislocation motion and the sheet rolling are terminated, the nanotube formation is finished. Upon cooling, such a nanotube will slide out of the unclosed part of the roll.

Let us make some numerical estimates. The elastic energy of a graphite layer rolled up into a nanotube can be estimated as $\Delta E = 0.25A(d/r)^2$, where $A \sim 10$ eV/atom, d is the spacing of sheets in a nanotube, and r is the nanotube radius [6]. The radial slippage of dislocations takes place provided that the tensile energy ΔE exceeds the Peierls energy: $\Delta E > U = (1/\pi)b^2\sigma$, where σ is the Peierls stress. In our case, the Burgers vector of the dislocation is equal to the sheet spacing in the roll ($b = d$). Therefore, the roll radius corresponding to the onset of dislocation slippage and the nanotube formation is on the order of 10 nm.

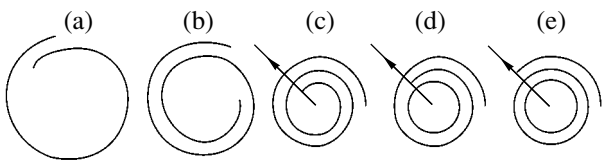

Fig. 1. Sequential stages (a–c) of graphite sheet rolling, illustrating the formation of (d) a single-sheet nanotube and (e) a multisheet nanotube as a result of (c–e) dislocation slippage.

1063-7850/03/2906-0494$24.00 © 2003 MAIK "Nauka/Interperiodica"

A multisheet nanotube formed by this mechanism may consist of sheets characterized by the same helicity and chirality. However, in case when the roll is extended along the rolling axis in the course of dislocation slippage, the shells may form with different helicities as observed in experiment [7].

The mechanism proposed for the cone formation differs from that described above in that only one end of the graphite sheet (namely, that subject to heating) is rolled. In this system, the rolling is accompanied by the slippage of disclinations (rather than dislocations) and the model is referred to as the disclination mechanism.

In selecting the optimum conditions for the formation of nanotubes according to the mechanism described above, it should be taken into account that a graphite sheet must be heated at a moderate rate. This will allow the van der Waals bonds between graphite layers to be broken and the separating sheets of graphite to be obtained, while not causing decomposition of the evaporated graphite into separate atoms. The controlled evaporation of graphite can proceed either under the action of ohmic heating of a graphite electrode or under laser irradiation of a graphite target [1, 2]. The formation of rolls and slippage of dislocations can also take place under the action of external mechanical stresses.

The proposed model probably describes the main mechanism for the formation of nanotubes from tubular spiral rolls. It should be noted that reviews [2] and [3] follow opposite points of view concerning the possibility of nanotube formation from graphite layers. This problem can be solved either by direct observation of the process of nanotube formation *in situ* in a microscope possessing high temporal resolution or by computer simulation methods [8].

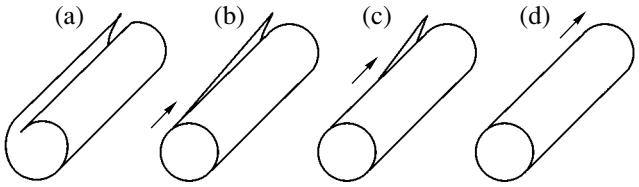

Fig. 2. Sequential stages of the zipper mechanism, with (a) the sheet edges approaching one another, (b, c) dislocation slippage, and (d) nanotube formation.

REFERENCES

1. A. V. Eletskiĭ and B. M. Smirnov, Usp. Fiz. Nauk **163** (2), 33 (1993).
2. A. V. Eletskiĭ and B. M. Smirnov, Usp. Fiz. Nauk **165** (9), 977 (1995) [Phys. Usp. **38**, 935 (1995)].
3. Yu. E. Lozovik and A. M. Popov, Usp. Fiz. Nauk **167** (7), 751 (1997) [Phys. Usp. **40**, 717 (1997)].
4. A. L. Ivanovskiĭ, Usp. Khim. **68** (2), 119 (1999).
5. S. Amelinckx, D. Bernaerts, X. B. Zhang, *et al.*, Science **267**, 1334 (1995).
6. M. Cote, M. L. Cohen, and D. J. Chadi, Phys. Rev. B **58**, R4277 (1998).
7. X. F. Zhang, X. B. Zhang, G. van Tendeloo, *et al.*, J. Cryst. Growth **130**, 368 (1993).
8. V. V. Pokropivny, V. V. Skorokhod, G. S. Oleinik, *et al.*, J. Solid State Chem. **154**, 214 (2000).

Translated by P. Pozdeev

Technical Physics Letters, Vol. 29, No. 6, 2003, pp. 496–499. Translated from Pis'ma v Zhurnal Tekhnicheskoĭ Fiziki, Vol. 29, No. 12, 2003, pp. 25–32.

Silicon Surface Reconstruction Lost upon Cobalt Adsorption

M. V. Gomoyunova, I. I. Pronin, N. R. Gall', S. L. Molodtsov, and D. V. Vyalykh

Ioffe Physicotechnical Institute, Russian Academy of Sciences, St. Petersburg, 194021 Russia

e-mail: Marina.Gomoyunova@mail.ioffe.ru

Received December 29, 2002

Abstract—We have studied the room-temperature adsorption of cobalt in the range of submonolayer coverages on a reconstructed Si(100)2 × 1 surface. The measurements were performed by methods of high-resolution (~140 meV) photoelectron spectroscopy using synchrotron radiation ($h\nu$ = 130 eV). An analysis of changes in the Si 2*p* line shape in the course of cobalt deposition showed that the metal adsorption leads to the loss of the initial substrate surface reconstruction. The results are interpreted using a model whereby adatoms arriving at the silicon surface are incorporated into the uppermost atomic monolayer, occupying positions between four Si atoms and forming rows parallel to the ⟨110⟩ directions in the substrate. © *2003 MAIK "Nauka/Interperiodica".*

The system of Co/Si(100) is of considerable interest from both basic and applied standpoints owing to the possibility of obtaining epitaxial structures with atomically sharp $CoSi_2$/Si interface and a combination of valuable properties inherent in $CoSi_2$ (high conductivity, thermal stability, etc.). Especially good prospects are related with using low-dimensional $CoSi_2$/Si structures in ultra-large-scale integrations. However, some questions concerning the early stages of $CoSi_2$ phase formation on Si(100)2 × 1 still remain unclear. In particular, there is no commonly accepted opinion as to whether cobalt atoms in the first adlayer are capable of chemically interacting with the substrate to form a $CoSi_2$-like compound at room temperature [1–6]. There are certain discrepancies in the assignment of adsorption sites of Co atoms on the Si(100)2 × 1 surface [6, 7].

An effective means of studying atomic processes on solid surfaces is offered by high-resolution photoelectron spectroscopy based on measuring the binding energies of core electrons, which are known to depend on the physicochemical state of the probed atoms [8]. The early stages of silicide formation in the Co/Si(100) system were studied by this method in only a few cases [1, 5, 9] and the level of resolution achieved in these experiments (~350 meV) was insufficient even for satisfactorily resolving the $2p_{1/2}$, $2p_{3/2}$ doublet of silicon.

This Letter, devoted to the adsorption stage of the interaction between cobalt atoms and Si(100)2 × 1 surface, describes the results of our experiments performed with a higher energy resolution. This allowed us to extract new information about the mechanism of the process studied.

The experiments were performed on a Russian–German synchrotron radiation channel recently set to operation at the BESSY II storage ring. The photoelectron spectra were measured at a primary photon energy of $h\nu$ = 130 eV, which corresponds to a maximum surface sensitivity for excitation of the Si 2*p* core electron levels. The overall energy resolution of the electron energy analyzer and monochromator was ~140 meV. The samples were prepared using single crystal silicon plates of the KEF-1 grade, with disorientation relative to the (100) crystal face not exceeding 0.1°. Prior to mounting samples in a vacuum chamber of the photoelectron spectrometer, the plates were chemically treated as described by Ishizaka and Shiraki [10] and then annealed under ultrahigh vacuum conditions; the time of exposure at a maximum temperature of 1200°C was 30 s and the cooling rate did not exceed 50 K/min. This pretreatment ensured the obtaining of a silicon surface with the Si(100)2 × 1 reconstruction, free of carbon- and oxygen-containing contaminations as confirmed by the low-electron energy diffraction patterns and by the photoelectron spectra. Cobalt atoms were deposited onto the substrate surface from a thoroughly outgassed evaporation source, in which a special-purity Co wire was heated by electron bombardment. Prior to each 30-s exposure, the source was heated for 2 min under conditions whereby the beam of cobalt atoms could not reach the silicon crystal surface. The rate of cobalt deposition was 1.2 monolayer (ML) per minute (one monolayer coverage of cobalt atoms corresponds to their surface density of 6.8×10^{14} cm^{-2}, which equals the density of silicon atoms on the substrate surface). The measurements were performed at room temperature in a vacuum of 1.2×10^{-8} Pa.

Figure 1 shows a typical Si 2*p* photoelectron spectrum of a pure silicon substrate. The spectrum is presented with subtracted background and compared to the results of computer modeling. Prior to proceeding with an analysis of the experimental data, we must note that, because of termination of the translation symmetry at

the crystal–vacuum interface, atoms of the uppermost surface layer occur under special conditions as compared to the bulk atoms. This results in a shift of the binding energies of the core electron levels and in the appearance of new (surface) components in the observed photoelectron spectrum [8]. In the case of a reconstructed crystal surface, where the number of atoms occurring in nonequivalent positions is increased, the number of such additional components still increases and the spectrum becomes even more complicated. As is known, reconstruction of the 2×1 type silicon surface consists in the formation of a system of rows of asymmetric dimers (schematically depicted in the inset in Fig. 1) oriented along $\langle 110 \rangle$ direction of the substrate [11].

The problem of interpretation of the Si 2*p* spectrum has been extensively studied for more than a decade, which resulted in the development of two close (but still somewhat different) models. In the basic work of Landemark *et al.* [12], it was demonstrated that the spectrum contains four surface components in addition to the bulk mode (*B*). Two surface modes—S_u and S_d, characterized by negative and positive energy shifts, respectively—are related to the upper and lower atoms of the asymmetric dimers. The third component (S_1) with a positive energy shift is assigned to atoms in the first monolayer situated immediately under the rows of dimers. Finally, the fourth component (S_2) characterized by a negative energy shift is attributed to atoms of a deeper (second) atomic layer. According to the alternative model of Pi *et al.* [13], the S_d mode is close to the bulk component and has a negative energy shift, while the S_2 mode splits into two components belonging to atoms of the second layer with (S_2) and without (S_2') above-lying atoms of dimers.

Our analysis of the spectrum in Fig. 1 was performed within the framework of the latter model. All modes of the spectrum were described by the Voigt functions [13] usually employed for these purposes. These functions represent convolutions of the Lorentz functions (with allowance of the hole lifetime on a core level) and the Gauss functions (reflecting phonon broadening of the lines and the instrumental energy resolution). In the course of decomposition of the Si 2*p* spectrum into components, we varied the width of components, their energy positions, and the relative intensities. The best agreement with experiment was obtained for the Lorentz and Gauss functions with the halfwidth of 70 and 300 meV, respectively. The splitting of components in the Si 2*p* doublet was assumed to be constant (608 meV) and the ratio of intensities of the $2p_{3/2}$ and $2p_{1/2}$ components was equal to two. The results of the mathematical modeling are illustrated by Fig. 1 showing the relative intensities of the $2p_{3/2}$ surface modes. As can be seen, the sum of these components fits the results of experimental measurements well. The energy shifts of the surface components relative to

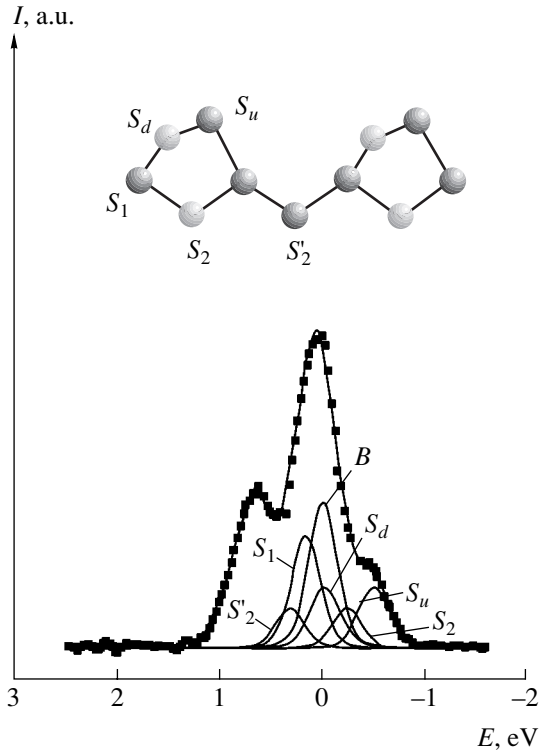

Fig. 1. Si 2*p* photoelectron spectrum of a Si(100)2×1 surface measured at $h\nu$ = 130 eV (black squares) and the results of its deconvolution (solid profiles) into bulk (*B*) and surface components (as indicated in the inset showing the surface dimers on the reconstructed silicon surface).

the bulk mode are –510 meV (S_u), –240 meV (S_2'), 90 meV (S_d), 180 meV (S_1), and 330 meV (S_2). These values satisfactorily agree with the results reported in [13], thus confirming the validity of the model chosen.

Figure 2 presents data characterizing the adsorption of cobalt atoms on the reconstructed single crystal silicon surface at room temperature. Here, the Si 2*p* spectrum measured after depositing 0.6 ML of cobalt is compared to the spectrum of a pure substrate. The first point to note is a significant change in the line shape observed on the right-hand wing of the profile, where a step characteristic of the Si(100)2×1 reconstruction completely disappears. In order to analyze the adsorption-induced changes, the new spectrum was also decomposed into bulk and surface components. The results of computer modeling are depicted by solid curves in Fig. 2. As can be seen, the aforementioned change is due to the disappearance of the surface components S_u and S_d, related to the asymmetric dimers present on the initial reconstructed silicon surface, and the appearance of a new surface mode *S* with an energy shift of –290 meV relative to the bulk mode.

The absence of components due to the asymmetric dimer indicates that the adsorption of cobalt has led to an atomic rearrangement on the silicon surface. The

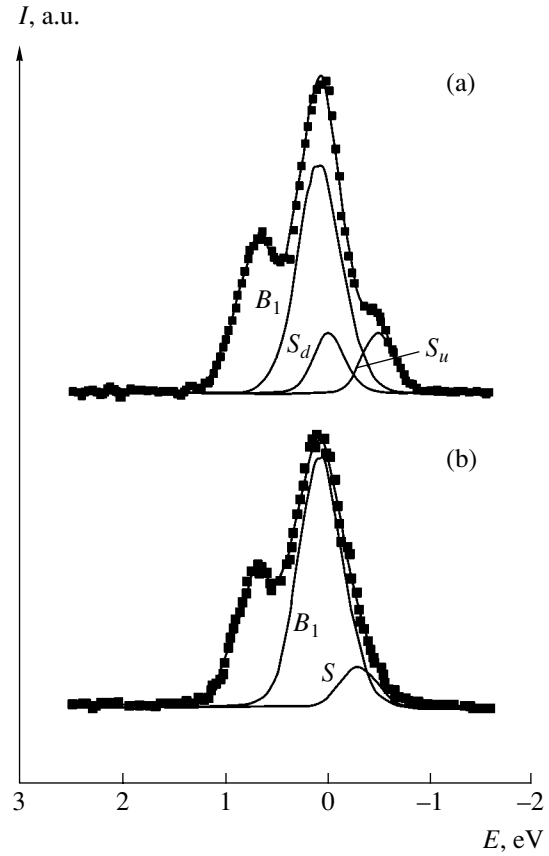

Fig. 2. Si 2*p* photoelectron spectra of (a) a pure silicon surface and (b) the same surface covered with 0.6 ML of cobalt. Solid profiles show the results of deconvolution into components according to the model adopted. For the sake of clarity, the modes S_1, S_2, S_2', and B (see Fig. 1) are combined into component B_1.

assumption that the adsorption merely transforms the dimers from asymmetric into symmetric (similarly to what takes place during the adsorption of alkali metals on Si(100)2 × 1 [14]) is unacceptable. Indeed, if such were the case, the intensity of the new mode would have to correspond to a monolayer of silicon atoms; however, this is not observed in experiment, where the new component has a much lower intensity. The results can be consistently explained only by assuming that the substrate surface has lost the initial reconstruction upon the adsorption of cobalt. It should be noted that this conclusion is also confirmed by data of Meyrheim *et al.* [4] obtained by measuring the extended X-ray absorption fine structure (EXAFS).

As for the adsorption sites, the results of recent theoretical calculations of the energies of interaction between Co and Si atoms [7], the energetically favorable sites for Co atoms on the Si(100)2 × 1 surface are those with the maximum number of interatomic bonds. This tendency is explained by the high valence of cobalt atoms. For these reasons, we believe (in agreement with [4]) that cobalt atoms are localized in the uppermost layer of a nonreconstructed Si(100) surface, in the sites between four silicon atoms. Each adsorbed atom forms seven bonds with the substrate. The first coordination sphere of a Co atom contains two silicon atoms from the second (subsurface) layer, involved in the formation of bridging bonds. The second coordination sphere contains five silicon atoms, four of which occur in the uppermost monolayer around the Co atom. Apparently, the interaction with these atoms saturates dangling bonds at the silicon substrate. The fifth atom is situated immediately below the adatom in the third subsurface layer.

On the passage from single adsorption events to extended submonolayer cobalt coverages of Co atoms, it should be taken into account that each atom on a nonreconstructed Si(100) surface has two dangling bonds. We can expect that saturation of these bonds as a result of the interaction with adatoms will be most effective when Co atoms are either adsorbed in a staggered order or form atomic rows similar to those of dimers on the Si(100)2 × 1 surface. We believe that the latter model is more likely, being confirmed by a diffraction pattern of the (2 × 1) type retained in the region of submonolayer coverages (according to [4], even for greater coverages up to 2.5 ML). In this case, the cobalt coverage corresponding to saturation is 0.5 ML. Then, the fact that deposition of 0.6 ML of cobalt leads to the loss of the initial reconstruction confirms the validity of the adsorption pattern outlined above.

Now let us turn to interpretation of the new mode observed in the Si 2*p* spectrum upon cobalt adsorption. First, note that the relatively low intensity of this component is evidence in favor of its assignment to silicon atoms of the second layer forming the shortest (bridging) bonds with cobalt adatoms. These silicon atoms are screened by atoms of the uppermost layer and by the incorporated cobalt adatoms (which also significantly contribute to attenuation of this mode). As for the negative value of the corresponding energy shift, this is characteristic [9] of the so-called adamantane disilicide [15] formed when tetrahedral voids in the crystal lattice of silicon are occupied with cobalt. Indeed, the aforementioned adsorption sites of Co adatoms on silicon just correspond to the positions of Co atoms on the surface of such silicide.

Thus, the results obtained in this study indicate that room-temperature adsorption of cobalt on Si(100)2 × 1 leads to the loss of this initial reconstruction. This effect is caused by Co adatoms incorporating into the uppermost layer of silicon, occupying the four-fold symmetry sites between silicon atoms and forming rows parallel to ⟨100⟩ directions on the Si(100) surface.

Acknowledgments. The work was supported by the Russian Foundation for Basic Research (project no. 01-02-17288), by the Ministry of Industry, Science, and Technology of the Russian Federation (project no. 40.012.1.1.1152), and by the Russian–German Laboratory at BESSY II.

REFERENCES

1. J. M. Gallero, R. Miranda, S. Molodtsov, *et al.*, Surf. Sci. **239**, 203 (1990).
2. U. Starke, W. Weiss, G. Rangelov, *et al.*, Surf. Sci. **352**, 89 (1996).
3. W. Weiss, U. Starke, K. Heinz, *et al.*, Surf. Sci. **347**, 117 (1996).
4. H. L. Meyrheim, U. Döbler, and A. Puschmann, Phys. Rev. B **44**, 5738 (1991).
5. G. Rangelov, P. Augustin, J. Stober, *et al.*, Phys. Rev. B **49**, 7535 (1994).
6. W. S. Cho, J. Y. Kim, N. G. Park, *et al.*, Surf. Sci. **453**, L309 (2000).
7. A. P. Horsfield, S. D. Kenny, and H. Fujitany, Phys. Rev. B **64**, 245332 (2001).
8. J. W. F. Egelhoff, Surf. Sci. Rep. **6**, 253 (1987).
9. G. Rangelov and Th. Fauster, Surf. Sci. **365**, 403 (1996).
10. A. Ishizaka and Y. Shiraki, J. Electrochem. Soc. **133**, 666 (1986).
11. W. S. Yang, F. Jona, and P. M. Marcus, Phys. Rev. B **28**, 2049 (1983).
12. E. Landemark, C. J. Karlsson, Y.-C. Chao, *et al.*, Phys. Rev. Lett. **69**, 1588 (1992).
13. T.-W. Pi, C.-P. Ouyang, J.-F. Wen, *et al.*, Surf. Sci. **514**, 327 (2002).
14. Y.-C. Chao, L. S. O. Johansson, C. J. Karlsson, *et al.*, Phys. Rev. B **52**, 2579 (1995).
15. W. R. L. Lambrecht, N. E. Christensen, and P. Blöchl, Phys. Rev. B **36**, 2493 (1987).

Translated by P. Pozdeev

Technical Physics Letters, Vol. 29, No. 6, 2003, pp. 500–501. Translated from Pis'ma v Zhurnal Tekhnicheskoĭ Fiziki, Vol. 29, No. 12, 2003, pp. 33–36.

Adsorption of Vanadium on Rutile: A Change in the Electron Work Function

S. Yu. Davydov and A. V. Pavlyk

Ioffe Physicotechnical Institute, Russian Academy of Sciences, St. Petersburg, 194021 Russia

St. Petersburg State Electrotechnical University, St. Petersburg, 197376 Russia

Received December 30, 2002

Abstract—A change in the electron work function caused by the adsorption of vanadium atoms on the (110)TiO_2 (rutile) surface was calculated taking into account both the dipole–dipole repulsion of adatoms and the adlayer metallization (in a parametric form) coverages. The results of model calculations agree well with the experimental data. © *2003 MAIK "Nauka/Interperiodica".*

The interaction of metal atoms with metal oxides, although not studied for a long period of time, is of considerable interest [1]. Among the variety of oxides, rutile (TiO_2) is a compound whose surface properties seem to be most thoroughly studied (probably because rutile is used as a catalyst in photoelectrolytic processes). A model proposed recently [2, 3] for the adsorption of alkali metals on rutile quite satisfactorily described the change $\Delta\phi$ in the electron work function as a function of the degree of surface coverage $\Theta = N_a/N_{ML}$, where N_a and N_{ML} are the adatom concentrations on the surface and in a monolayer.

In this study, the above model has been applied to description of the adsorption of vanadium on the (110)TiO_2 surface, which had been experimentally studied by Zhang and Heinrich [4].

Strictly speaking, the model developed in [2, 3] is inapplicable to description of the interaction of vanadium adatoms with this substrate. Indeed, in contrast to alkali metal atoms containing only one electron in the outer *s* shell, vanadium is characterized by a completely filled 4*s* shell. Within the framework of a description based on the Anderson Hamiltonian (see, e.g., [5]) on which the aforementioned model [2, 3] is based, one has, first, to introduce the creation–annihilation operators for each of the two sublevels in the *s* shell and, second, to solve the corresponding self-consistent problem for an isolated adatom before passing to the case of finite adsorption coverages.

However, estimates employing the experimental data on the electron work function reported in [4] show that only one electron (and, hence, only one electron orbital) in the *s* shell of vanadium is involved in adsorption, since the charge of an adatom is below unity. Therefore, we may suggest that, in the course of the adatom–substrate interaction, one 4*s* electron passes to the 3*d* shell (so that the adatom of vanadium features a $3d^4 4s^1$ configuration rather than the $3d^3 4s^2$ electron structure inherent in the vanadium atom), while another electron remains in the 4*s* state and performs a tunneling transition into the substrate (on Ti^{4+} ion). Additional evidence of this possibility is provided by the fact that the niobium atom (belonging to the same group V as does vanadium) possesses an outer electron shell configuration of $4d^4 5s^1$. These considerations allow us to apply the model [2, 3], developed for one-electron adatoms, to the case of two-electron vanadium.

According to the aforementioned model [2, 3], dependence of the adatom charge Z on the coverage Θ is described by the formulas

$$Z(\Theta) = \frac{2}{\pi}\arctan\frac{\Omega - \xi\Theta^{3/2}Z(\Theta)}{\Gamma(\Theta)},$$

$$\xi = 2e^2\lambda^2 N_{ML}^{3/2} A, \quad \Gamma = \Gamma_0(I + \gamma\Theta), \qquad (1)$$

$$\Omega = \phi - I + \Delta, \quad \Delta = e^2/4\lambda.$$

Here, Ω is the quasilevel energy of the adatom relative to the substrate Fermi level, ξ is the constant of the dipole–dipole repulsion between adatoms, 2λ is the surface dipole length, and $A \sim 10$ is a dimensionless coefficient weakly dependent on the adatom lattice geometry; where Γ_0 is the quasilevel halfwidth of an isolated adatom; γ is a dimensionless coefficient reflecting the band broadening (metallization effects); I is the ionization energy of adsorbed atoms; ϕ is the electron work function of rutile; and Δ is the Coulomb shift of the quasilevel of an adatom as a result of the interaction of its electron with substrate electrons.

The change in the electron work function upon adsorption is determined by the formulas

$$\Delta\phi(\Theta) = -\Phi\Theta Z,$$
$$\Phi = 4\pi e^2 N_{ML}\lambda. \qquad (2)$$

1063-7850/03/2906-0500$24.00 © 2003 MAIK "Nauka/Interperiodica"

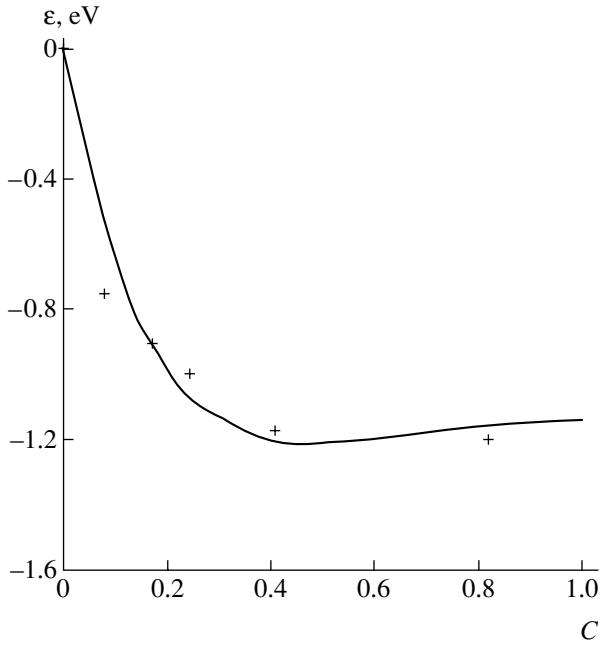

A change in the electron work function versus the adsorption coverage for vanadium on rutile: solid curve presents the result of numerical calculations using the proposed model, crosses represent the experimental data from [4].

The model parameters are specified using a scheme developed in [2]. As a result, we obtain $N_{ML} = 0.6 \times 10^{15}$ cm^{-2}, $\lambda = 1.31$ Å, $\Omega = 1$ eV, $\Gamma_0 = 2.04$ eV, $\gamma = 0.745$ eV, $\Phi = 27.4$ eV, $\xi = 19.4$ eV, $Z_0 = 0.29$, and $Z_{ML} = 0.04$.

Note that the energy parameters of the V–(110)TiO_2 system are virtually the same as those for the submonolayer films of alkali metals. However, the charges of vanadium adatoms for both zero (Z_0) and monolayer (Z_{ML}) coverages are significantly smaller than the values for alkali metal adatoms. This result agrees with experiment, where the maximum decrease in the electron work function upon vanadium adsorption is on the order of 1 eV, while the adsorption of alkali metal atoms leads to $\Delta\phi_{max} \sim -3$ eV. The results of $\Delta\phi(\Theta)$ calculations are presented in the figure. As can be seen, the calculated curve quite satisfactorily agrees with the experimental data [4].

Thus, we have demonstrated that a simple model developed for the adsorption of alkali metals is applicable to a wider range of systems.

REFERENCES

1. V. E. Henrich and P. A. Cox, *The Surface Science of Metal Oxides* (Cambridge University Press, Cambridge, 1994).
2. S. Yu. Davydov and I. V. Noskov, Pis'ma Zh. Tekh. Fiz. **27** (20), 1 (2001) [Tech. Phys. Lett. **27**, 844 (2001)].
3. S. Yu. Davydov and I. V. Noskov, Zh. Tekh. Fiz. **72** (11), 137 (2002) [Tech. Phys. **47**, 1481 (2002)].
4. Z. Zhang and V. E. Heinrich, Surf. Sci. **277**, 263 (1992).
5. C. Kittel, *Quantum Theory of Solids* (Wiley, New York, 1963; Nauka, Moscow, 1967).

Translated by P. Pozdeev

Technical Physics Letters, Vol. 29, No. 6, 2003, pp. 502–503. Translated from Pis'ma v Zhurnal Tekhnicheskoĭ Fiziki, Vol. 29, No. 12, 2003, pp. 37–41.

Operation Speed and Energy Consumption for Switching Cells of a Magnetooptical Spatial Light Modulator

M. V. Logunov*, N. V. Moiseev, Yu. N. Sazhin, and S. V. Yudina

Mordvinian State University, Saransk, Mordvinia, Russia

** e-mail: logunov@mrsu.ru*

Received January 9, 2003

Abstract—The dynamics of magnetization reversal in magnetooptical spatial light modulators based on bismuth-containing garnet ferrite films have been studied by high-rate photography techniques. It is shown that the dependence of the energy required for switching the spatial light modulator cells on the switching time exhibits a threshold character. © *2003 MAIK "Nauka/Interperiodica".*

Field-controlled magnetooptical spatial light modulators [1–6] are used in optical signal processors, printers, displays, and fiber optic commutators. These devices are more advantageous than their liquid crystal analogs [7], primarily due to higher operation speed. An important direction in the development of such spatial light modulators consists in decreasing the magnitude of the control magnetic field [8] and the duration of the magnetic field action. These parameters determine the level of heat evolution in the conductors generating the control fields and, hence, influence the thermal stability of device operation.

Below we present the results of investigation into the dynamic processes of magnetization reversal in a prototype spatial light modulator. The study was performed by a high-rate photography technique ensuring a time resolution of about 5 ns [9]. The prototype spatial light modulator with a cell size ~100 μm was obtained by diffusion annealing of a (210)-oriented single crystal film of a bismuth-containing garnet ferrite with the composition $(Bi,Y,Pr)_3(Fe,Ga)_5O_{12}$ [4, 10]. The deviation of the easy magnetization axis from the spatial light modulator plane normal (which is inherent in the garnet films with this orientation [11, 12]) did not exceed a few degrees. The state of the cells was changed by applying a quasistatic bias field H_b and/or a pulsed field H_p perpendicular to the spatial light modulator plane. The leading and trailing front durations of the H_p field pulses were about 20 ns.

Figure 1 shows the temperature variation of the main static parameters of the garnet ferrite film measured outside the spatial light modulator cells. These include the strip domain period P_0, the bubble domain collapse field H_0, the anisotropic field strength H_k, and the static cell switching field H_{st}. The presence of the point of magnetic moment compensation below room temperature was manifested by an increase in the cell switching field H_{st} on approaching room temperature. The monodomain state of the cells in the absence of H_b and H_p was retained far from the compensation point, at temperatures up to and above 100°C. On the whole, the thermal stability of the film parameters meets all requirements on the materials for spatial light modulators.

The data of high-rate photography showed that the main mechanism of magnetization reversal in a pulsed field for the spatial light modulator studied is via the motion of domain walls from the periphery to the center of the cell. In the case of fields $H_p > 200$ Oe, there is an additional mechanism via the nucleation of domains over the cell area during the field pulse action. High dynamic parameters of the prototype spatial light modulator are due to the (210) orientation of the film. This implies the presence of an orthorhombic anisotropy component [11, 12] known to increase the limiting velocity of the steady-state domain wall motion [10].

The main dynamic parameter determining the cell switching rate in the spatial light modulator is the

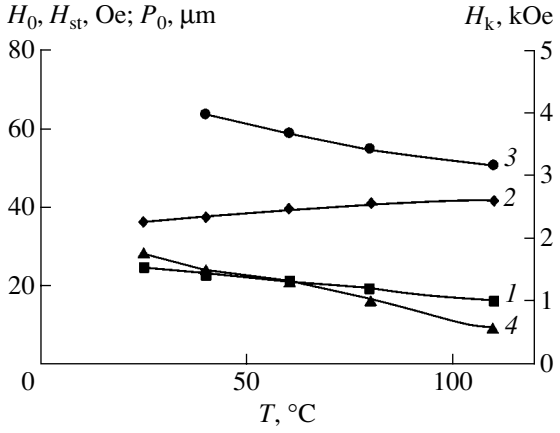

Fig. 1. Temperature variation of the main static parameters of the initial garnet ferrite film: (*1*) the strip domain period P_0; (*2*) the bubble domain collapse field H_0; (*3*) the anisotropic field strength H_k; (*4*) the static cell switching field H_{st}.

1063-7850/03/2906-0502$24.00 © 2003 MAIK "Nauka/Interperiodica"

domain wall saturation velocity V_S. In the working temperature interval of the spatial light modulator studied (T = 20–100°C), this parameter exhibited a twofold change with a minimum value of about ~350 m/s. This saturation velocity is more than ten times greater than the domain wall velocity in (111)-oriented films (the main material for magnetooptical devices, characterized by predominantly uniaxial anisotropy). This advantage determines the high dynamic properties of the spatial light modulator, in which the cell switching time can be reduced to below 0.1 μs (Fig. 2).

Another parameter significantly determining the choice of materials for magnetooptical devices is the energy E required for creating a magnetic field pulse during the magnetization reversal in the spatial light modulator cells. This characteristic influences the thermal stability of a magnetooptical device and determines the range of its stable operation. The value of E depends on the strength H_p and duration t_p of the pulsed magnetic field required for the cell switching as described by the relation

$$E \sim H_p^2 t_p.$$

We have established that the $E(t_p)$ curves exhibit two characteristic regions (see Fig. 2). In the system studied, the magnetization reversal time depends on H_p. As the H_p value grows, t_p decreases due to an increase in the domain wall velocity and in the density of the domain nucleation centers. The growth in the energy consumption (for the same switching time) is also related to a change in the relative contributions of these magnetization reversal mechanisms, mostly to a decrease in the domain wall velocity. Note that the two regions with different slopes of the $E(t_p)$ curve are observed at various temperatures in the entire range studied.

The nonlinear character of $E(t_p)$ is an important factor. For example, an attempt at decreasing the magnetization reversal time by a factor of 1.5–2 may lead to a more than tenfold increase in the energy consumption for the cell switching. This, in turn, can result in the spatial light modulator cell malfunction caused by increased energy evolution in the current-carrying elements generating the control magnetic fields and the related changes in the temperature regime of the spatial light modulator operation.

Knowledge of the threshold character of the energy consumption for the cell switching allows the spatial light modulator operation regime to be optimized by correctly choosing between maximum operation speed and acceptable energy evolution level in the spatial light modulator control system.

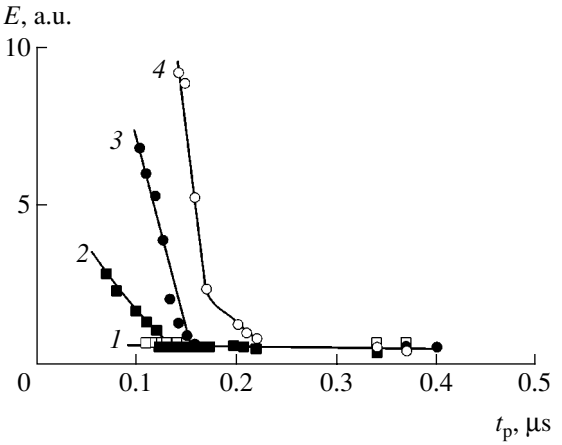

Fig. 2. Plots of the energy required for the spatial light modulator magnetization reversal versus cell switching time at various temperatures: T = 28 (*1*), 60 (*2*), 80 (*3*), and 107°C (*4*).

REFERENCES

1. B. Hill and K. P. Schmidt, Philips J. Res. **33** (5/6), 211 (1978).
2. P. B. Paroli, Thin Solid Films **114**, 187 (1984).
3. A. P. Gubarev, V. V. Randoshkin, V. B. Sigachev, *et al.*, Zh. Tekh. Fiz. **55** (7), 1393 (1985) [Sov. Phys. Tech. Phys. **30**, 803 (1985)].
4. M. V. Logunov, V. V. Randoshkin, Yu. N. Sazhin, *et al.*, Zh. Tekh. Fiz. **61** (4), 205 (1991) [Sov. Phys. Tech. Phys. **36**, 493 (1991)].
5. A. A. Balakhonskiĭ, N. N. Kiryukhin, V. A. Nikerov, *et al.*, Mikroélektronika **20** (3), 304 (1991).
6. J. Cho, S. Santhanam, T. Le, *et al.*, J. Appl. Phys. **76**, 1910 (1994).
7. V. L. Vladimirov, I. E. Morichev, N. I. Pletneva, *et al.*, Zh. Tekh. Fiz. **60** (3), 203 (1990) [Tech. Phys. **35**, 398 (1990)].
8. J. H. Park, K. Nishmura, M. Ionoue, *et al.*, J. Appl. Phys. **91**, 7014 (2002).
9. M. V. Logunov, V. V. Randoshkin, and V. B. Sigachev, Prib. Tekh. Éksp. **28** (5), 247 (1985).
10. V. P. Klin, M. V. Logunov, B. P. Nam, *et al.*, Pis'ma Zh. Tekh. Fiz. **15** (14), 79 (1989) [Sov. Tech. Phys. Lett. **15**, 571 (1989)].
11. A. M. Balbashov, F. V. Lisovskiĭ, and E. G. Mansvetova, Preprint IRÉ AN SSSR, No. 25 (100) (1988).
12. E. N. Il'icheva, A. V. Klushina, N. B. Shirokova, *et al.*, Zh. Tekh. Fiz. **67** (6), 32 (1997) [Tech. Phys. **42**, 615 (1997)].

Translated by P. Pozdeev

Technical Physics Letters, Vol. 29, No. 6, 2003, pp. 504–506. Translated from Pis'ma v Zhurnal Tekhnicheskoĭ Fiziki, Vol. 29, No. 12, 2003, pp. 42–48.

On the Mechanism of the External Magnetic Field Action on the Electron Temperature and Ion Charge State Distribution in a Vacuum Arc Plasma

I. A. Krinberg

Irkutsk State University, Irkutsk, Russia
e-mail: krinberg@physdep.isu.ru

Received January 10, 2003

Abstract—When an external axial magnetic field is applied to a vacuum arc, the radial expansion of plasma from cathode spots transforms into a plasma flow along the magnetic field, provided that the electron–ion collision frequency is smaller than the Larmor frequency. As the magnetic field strength increases, the diameter of the resulting cylindrical channel decreases. This leads to an increase in the electron temperature and the ion charge due to enhanced Joule heating of the plasma. Unlike the intrinsic azimuthal magnetic field, the external axial field only restricts expansion of the plasma, rather than compressing the plasma jet. © *2003 MAIK "Nauka/Interperiodica".*

Introduction. Vacuum arc discharge is widely used in ion-plasma coating devices and high-current sources of metal ion beams. An important problem encountered in the development of such discharge devices is related to the need for increasing the ion charge. A well-known approach to solving this problem consists in applying an axial magnetic field [1–3]. This method allows the average ion charge to be increased by a factor of 1.2–2.5 and provides for the appearance of a significant fraction of highly charged ions never observed in the absence of the field. It was established that the ion charge increases in magnetic fields on the order of $B \cong 10^{-2}$ T, but the growth ceases for $B \cong 0.2$–0.4 T [3]. An increase in the ion charge due to the magnetic field application is especially pronounced for a discharge current of $I = 10^2$–10^3 A and is less significant when the current grows further [1]. Recently [4], it was suggested to increase the ion charge by using a magnetic field increasing along the plasma jet axis.

Despite the wide practical use of a vacuum arc localized in the applied magnetic field, the mechanism of the field action on the arc plasma characteristics is still insufficiently studied. In the aforementioned papers [1–3], it was suggested that the growth of the fraction of multicharge ions is related to an increase in the electron temperature T_e in the near-cathode discharge region as a result of the increase in the arc operation voltage U upon application of the external magnetic field B. However, no relations between the values of B, U, and T_e were obtained within the framework of these notions [1–3]. The values of the electron temperature and density in the near-cathode region were empirically selected so as to make the measured ion charge close to the calculated value.

In this study, the phenomenon of the magnetic-field-induced increase in the ion charge is related to the appearance of anisotropy in the plasma conductivity upon application of the external magnetic field. We will consider the transition from radial expansion of the plasma to its longitudinal motion along the field, which leads to enhanced Joule heating of electrons and additional ionization of ions in the interelectrode gap outside the near-cathode region.

The effect of an external magnetic field. Let us consider the expansion of a plasma emitted from cathode spots during the vacuum arc discharge. Since the electron density at the plasma jet base (near the spot) is on the order of $N_e = 10^{16}$–10^{18} cm^{-3}, the electron–ion collision frequency $\nu_{el} = 1/\tau$ is significantly greater than the Larmor frequency $\omega = eB/m_e c$ (i.e., $\omega\tau \ll 1$) and the plasma is characterized by isotropic conductivity. The time between collisions is determined as [5]

$$\tau = \frac{3}{4}\sqrt{m_e/2\pi}(kT_e)^{3/2}/(e^4 Z^2 \ln\Lambda N_+), \qquad (1)$$

where e and m_e are the electron charge and mass, respectively; $\ln\Lambda$ is the Coulomb logarithm; $N_+ = N_e/Z$ is the ion density; and k is the Boltzmann constant.

In the initial part of the plasma jet, the expansion exhibits a nearly radial (spherical) character (within a cone of semi-vertex angle $\alpha \approx 30°$–$50°$). Since the electron density drops rapidly with the distance ($N_e \propto 1/x^2$), there is a certain value of x where $\omega\tau \geq 1$ and the transverse conductivity of the plasma $\sigma_\perp = \sigma/(1 + \omega^2\tau^2)$ becomes significantly lower than the longitudinal conductivity σ. For $\omega\tau \gg 1$, the current flows predominantly along the magnetic field lines and the plasma jet

1063-7850/03/2906-0504$24.00

ceases to expand. When the magnetic field strength increases, the transition to the longitudinal plasma flow begins closer to the cathode and the jet diameter decreases (Fig. 1). Should the condition $\omega\tau \geq 1$ be satisfied (for a certain $B = B_{max}$) immediately at the jet base (i.e., at the cathode spot), the plasma jet acquires a cylindrical shape and no longer changes with the field strength (for $B > B_{max}$).

It is easy to obtain a rough estimate for B_{max}. In a steady-state vacuum arc, the fluxes of mass $G = mN_+VS$ and charge $I = eN_e(V_e - V)S$ (m is the ion mass and S is the plasma jet cross section) do not change with the distance from the cathode. Using a dimensionless coefficient of erosion $\delta = eG/mI = \text{const}$, the electron velocity can be expressed through the ion velocity as $V_e = V(1 + 1/Z\delta)$. This leads to the following formula for the electron density:

$$N_e = IZ\delta/(eVS). \quad (2)$$

For an arc current of $I = 200$–500 A, the plasma jet originates from a group cathode spot with a diameter of $D_g \approx 1$–3 mm [6]. For the typical values of $S = \pi D_g^2/4 \approx 0.01$–$0.1$ cm^2, $Z\delta \approx 0.1$, and $V \approx 10^6$ cm/s at $I = 300$ A, we obtain $N_e \approx (3$–$30) \times 10^{15}$ cm^{-3}. Then, the condition $\omega\tau = 1$ yields $B_{max} \approx 0.2$–2 T (for $kT_e \cong 1$ eV). This estimate agrees with the results of measurements at $I = 300$ A, for which the ion charge ceased to increase at $B > 0.2$–0.3 T (near the cathode surface) [3]. For the currents $I \geq 1$ kA, the cathode spots usually spread over the whole surface and the initial jet diameter is equal to that of the cathode ($D_0 = D_{cath}$). In this case, provided there is a "strong" magnetic field ($B \geq B_{max}$), the plasma column diameter D coincides with the cathode diameter along the entire arc length. According to the results of measurements for $I = 1$–3 kA [1], the plasma jet diameter near the anode in the absence of an external field was $D \approx 20$ mm. Upon application of a field with $B = 0.1$–1 T, the column diameter decreased to $D \approx 5$ mm, which was close to the cathode diameter ($D_{cath} = 6$ mm).

Under the conditions of a weakly expanding jet ($S \approx \text{const}$), the energy $I^2/\sigma S^2$ supplied to electrons produces an increase in the electron temperature. As a result, both the rate of ionization by electron impact and the ion charge increase outside the near-cathode region. This mechanism is close to the mechanism of ion charge buildup under the action of the self-magnetic field of a current-carrying plasma column [7, 8]. However, unlike the intrinsic azimuthal magnetic field, the external axial field only restricts expansion of the plasma, rather than compressing the plasma jet.

Model description. Let us evaluate variation of the electron temperature and ion charge in a vacuum arc upon application of an external axial magnetic field using the following simple model. The condition of zero current through the side surface of a plasma jet in

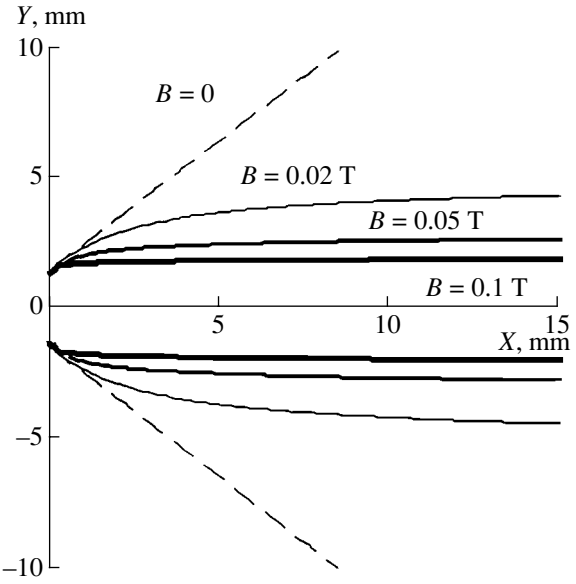

Fig. 1. Profile of the cathode plasma jet calculated for various values of the external axial magnetic field strength (Ti cathode, $I = 500$ A, $D_0 = 3$ mm).

the Cartesian coordinate system (Fig. 1) can be written as $j_x dy - j_y dx = 0$, where $j_x = \sigma E_x$ and $j_y = \sigma_\perp E_y$ are the longitudinal and transverse current densities. Then, the change in the jet radius $R = y$ is described by the equation $dR/dx = \sigma_\perp E_y/\sigma E_x$. In the initial portion of the jet (where $\sigma_\perp = \sigma$), we have $E_y/E_x = j_y/j_x = \tan\alpha$, where α is the semivertex angle of the plasma jet cone.

Calculation of the electric field distribution in the plasma is a rather complicated task. For a rough estimate, we assume that $E_y/E_x \cong \tan\alpha \cong 1$. This yields

$$\frac{dR}{dx} = \frac{\tan\alpha}{1 + \omega^2\tau^2}. \quad (3)$$

The thermal balance equation for electrons can be written as [5]

$$\frac{3}{2}P_e V_e \frac{d}{dx}\ln\left(\frac{P_e}{N_e^{5/3}}\right) = \frac{j^2}{\sigma} - Q_{ion}, \quad (4)$$

where $j = I/S$ is the current density, $P_e = N_e kT_e$ is the electron pressure, $\sigma = k_\sigma(kT_e)^{3/2}/Z$ is the conductivity of plasma ($k_\sigma = 3 \times 10^{13}$ eV$^{-3/2}$ s^{-1} for a typical value of the Coulomb logarithm $\ln\Lambda \approx 8$). The electron energy loss rate for ionization is given by the formula $Q_{ion} = N_e N_+ \sum_{n=1} E_{n+1} k_{n+1} f_n$, where $f_n = N_n/N_+$ is the fraction of ions with the charge n and the density N_n, and E_{n+1} and k_{n+1} are the energy and ionization coefficient for the formation of $(n + 1)$-charged ion, respectively. The

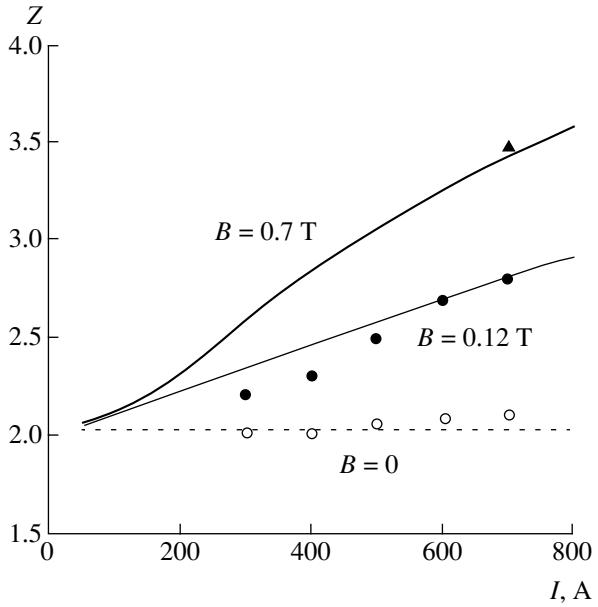

Fig. 2. Plots of the average ion charge Z versus arc current I for various values of the external axial magnetic field strength. Curves show the results of calculations using the proposed model; black and open circles represent the results of measurements for $B = 0.12$ T and $B = 0$, respectively [9]; triangle shows the experimental data for $B = 0.7$ T [1].

system of equations for calculating the ion charge distribution is as follows [7, 8]:

$$V\frac{\partial f_n}{\partial x} = k_n f_{n-1} N_e - k_{n+1} f_n N_e. \quad (5)$$

The average ion charge is defined as $Z = \sum_{n=1} n f_n$. The values of the ionization coefficients $k_n(T_e)$ can be found in [7, 8].

Results of calculation. The system of Eqs. (1)–(5) was solved for a vacuum arc with titanium cathode and an interelectrode gap length of $L = 15$ mm (corresponding to the experimental conditions studied in [9]). The change in the ion velocity V along the plasma jet axis was ignored. The calculation was performed for the following values of parameters: $\alpha = 45°$; $V = 1.5 \times 10^6$ cm/s; $Z_0\delta = 0.085$ [8]; and $2R_0 = D_g \approx 3$ mm [6]. The initial plasma jet cross section ($x = 0$) was characterized by $f_1^0 = 0.1$, $f_2^0 = 0.8$, $f_3^0 = 0.1$, $Z_0 = 2$, $kT_e = 1$ eV [8], and the electron density was determined by formula (2) for the known current I and the plasma jet cross section area $S = \pi R_0^2$.

The plasma jet profiles calculated for $I = 500$ A and various values of the magnetic field strength are presented in Fig. 1. The results clearly illustrate the transition from a cone-shaped jet to cylindrical column. As the applied field strength increases from 0.02 T to 0.05, 0.1, and 0.5 T the electron temperature acquires the values of 6, 10, 12, and 16 eV, respectively. The results of the calculation showed that the electron temperature and ion charge increase with the magnetic field strength until the latter reaches a level of approximately $B = 0.5$ T. As the field strength grows further, the plasma parameters remain unchanged. Figure 2 shows plots of the average ion charge versus current, $Z(I)$, calculated for the above parameters in comparison to the results of measurements reported in [1, 9]. As can be seen, the proposed model satisfactorily describes the trends in the ion charge variation with the external magnetic field and the discharge current.

Conclusions. The above analysis shows that the process of cathode plasma expansion in an external axial magnetic field ($B \geq 0.01$ T) leads to the appearance and increase of anisotropy in the plasma conductivity. As a result, the current flows predominantly along the magnetic field lines and a cylindrical plasma column (current channel) is formed with a diameter D decreasing with an increase in the field strength. For a given discharge current $I = jS$, a decrease in the current channel cross section leads to a sharp growth in the energy yield ($j^2/\sigma \propto 1/D^4$) per unit volume of plasma. This results in an increase in the electron temperature and the rate of ionization by electron impact. Since the axial magnetic field only restricts expansion of the plasma, rather than compressing the plasma jet, the column diameter can decrease only to a value equal to the cathode spot size. Further increase in the magnetic field strength ($B \geq 1$ T) changes neither the plasma column diameter nor the electron temperature nor the ion charge.

REFERENCES

1. E. M. Oks, A. Anders, G. Brown, *et al.*, IEEE Trans. Plasma Sci. **24**, 1174 (1996).
2. A. G. Nikolaev, E. M. Oks, and G. Yu. Yushkov, Zh. Tekh. Fiz. **68** (5), 39 (1998) [Tech. Phys. **43**, 514 (1998)].
3. A. Anders, G. Y. Yuskov, E. M. Oks, *et al.*, Rev. Sci. Instrum. **69**, 1332 (1998).
4. T. V. Kulevoĭ, R. P. Kubida, S. V. Petrenko, *et al.*, Preprints Inst. Teor. Éksp. Fiz., No. 14-01, 1 (2001).
5. S. I. Braginskiĭ, in *Problems in Plasma Theory* (Gosatomizdat, Moscow, 1963), Issue 1, pp. 183–272.
6. P. Siemroth, T. Schulke, and T. Witke, IEEE Trans. Plasma Sci. **25**, 571 (1997).
7. I. A. Krinberg, Pis'ma Zh. Tekh. Fiz. **27** (2), 9 (2001) [Tech. Phys. Lett. **27**, 45 (2001)].
8. E. A. Zverev and I. A. Krinberg, Prikl. Fiz., No. 5, 50 (2002).
9. M. Galonska, F. Heymach, R. Hollinger, *et al.*, in *Proceedings of NATO-Sponsored Research Workshop "Emerging Applications of Vacuum-Arc-Produced Plasma, Ion and Electron Beams"* (Kluwer Academic Publishers, Dordrecht, 2002), pp. 123–130.

Translated by P. Pozdeev

Technical Physics Letters, Vol. 29, No. 6, 2003, pp. 507–509. Translated from Pis'ma v Zhurnal Tekhnicheskoĭ Fiziki, Vol. 29, No. 12, 2003, pp. 49–53.

Controlled Switching Dynamics in Si–SiO_2–VO_2 Structures

A. A. Velichko*, N. A. Kuldin, G. B. Stefanovich, and A. L. Pergament

Petrozavodsk State University, Petrozavodsk, Karelia, Russia

** e-mail: velichko@mainpgu.karelia.ru*

Received January 8, 2003

Abstract—The dynamic current–voltage characteristics of a Si–SiO_2–VO_2 structure exhibiting the switching effect have been studied. It is demonstrated that the switching dynamics in this system can be controlled either by applying a bias voltage to the silicon substrate or by illuminating the vanadium dioxide surface. The latter method is based on the light-induced variation of the capacitance of the space charge region. The possibility of creating new semiconductor devices employing these effects is considered. *© 2003 MAIK "Nauka/Interperiodica".*

Investigations of the metal–insulator phase transition (MIPT) in vanadium dioxide (VO_2), being of interest from both basic and applied standpoints, still draw the attention of researchers [1, 2]. As is known, virtually all transition oxides featuring MIPT exhibit the switching effect. The mechanism of switching is usually described within the framework of the critical temperature model, according to which a current produces Joule heating of the material up to a temperature (T_t) of the transition to a metallic phase (for VO_2, T_t = 68°C), this being accompanied by a jump in the conductivity and the appearance of an S-shaped region of negative differential resistance on the current–voltage characteristic [1]. We have demonstrated that the MIPT temperature and, hence, the switching effect, can be controlled by application of the electric field [3] and by charge injection [4]. These effects can be successfully used as a means of control for the switching behavior, but the search for new methods of such control is currently important.

Here we report the results of investigations of a new means of controlling the dynamics of switching in a Si–SiO_2–VO_2 structure [5, 6]. The proposed method is based on changing the capacitance of the space charge region in this structure.

The experiments were performed with the structures representing a ~3000-Å-thick vanadium dioxide film on a Si–SiO_2 substrate (*p*-Si, ρ = 1 Ω cm; SiO_2 layer thickness, ~1000 Å). The VO_2 films were deposited by reactive magnetron sputtering in an Ar + O_2 atmosphere onto substrates heated to ~500°C, followed by 30-min annealing. Finally, aluminum film contacts were applied by thermal deposition in vacuum. The sample structure design, geometry, and the scheme of electrical measurements are illustrated in Fig. 1.

The ac current–voltage (*I–U*) characteristics of the samples were measured in the current generator regime (large R_1) using the scheme depicted in Fig. 1a. The ac probing signal ($U_\sim$) was supplied to the electrodes from generator *1* and the bias voltage (U_0) was applied to the silicon substrate from source *2*. All experiments involving the measurement of changes in the dynamic *I–U* curves of biased and illuminated structures were performed with the same amplitude of the probing signal ($U_\sim$ ~ 15 V) from generator *1*. The effect of illumination on the *I–U* characteristics was studied using an incandescent lamp.

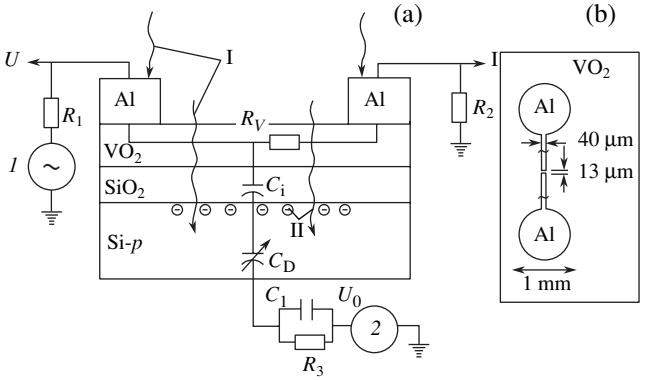

Fig. 1. Schematic diagrams of the Si–SiO_2–VO_2 structure studied, showing (a) the effective scheme of measurements and (b) the sample geometry: (*1*) probing signal generator (R_1 = 100 kΩ); (*2*) bias voltage source (R_2 = 10 Ω, R_3 = 560 kΩ, C_1 = 0.022 μF); (C_i) insulator capacitance; (C_D) space charge region capacitance; (R_V) VO_2 film resistance; (I) photons; (II) photoelectrons; (Al) aluminum contacts.

1063-7850/03/2906-0507$24.00 © 2003 MAIK "Nauka/Interperiodica"

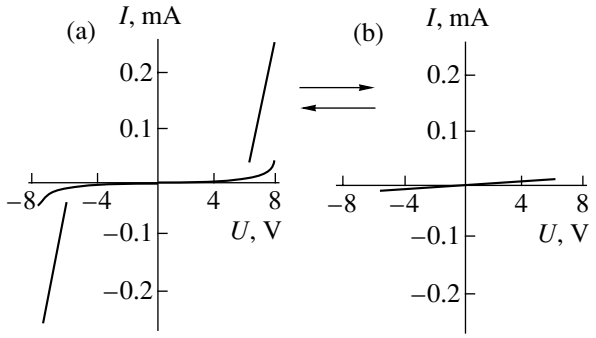

Fig. 2. The dynamic current–voltage characteristics of the Si– SiO_2–VO_2 structure in the regime (a) with and (b) without switching.

The Si–SiO_2–VO_2 structures studied exhibit current–voltage characteristics with switching (Fig. 2a). When the dynamic *I–U* curves were measured using a low-frequency (~100 Hz) probing signal, neither illumination of a sample nor a bias voltage applied to the silicon substrate (nor both these factors together) influenced the curve shape (at least in the range of U_0 from –30 to +30 V). However, when the measurements were performed with a signal of higher frequency, the structure could be reversibly converted into a state without switching by applying a certain bias voltage to the substrate. For example, the transition to a dynamic *I–U* curve of the type depicted in Fig. 2b, exhibiting no switching, was observed at a frequency of 6 kHz and $U_0 < -12.2$ V. With a positively biased substrate, degeneracy of switching was observed for $U_0 > 4.6$ V.

We have also observed the effect of illumination of the dynamics of switching in the structure studied. For $U_0 \geq 0$ (positively biased substrate), the illumination did not affect the switch operation. With a negative bias voltage applied to the substrate, even weak illumination led to the disappearance of switching on the dynamic *I–U* characteristic. For example, no switching was observed at 6 kHz for $U_0 = -8$ V and a radiant power flux of 5×10^{-4} J/(cm^2 s), whereby the *I–U* curve appeared as in Fig. 2b.

Thus, it was possible to control the dynamics of switching in the Si–SiO_2–VO_2 structure by changing the illumination intensity or the bias voltage U_0. In our opinion, the vanishing of switching on the dynamic *I–U* curve is related in all cases to an increase in the capacitance C_{iD} of the structure, comprising a sum of the C_i and C_D components (Fig. 1a). When the *I–U* measurements are performed with an ac signal, C_{iD} conducts a bias current and plays the role of a shunting element. This shunting leads to a decrease in the voltage drop across the VO_2 switch (R_V resistor in the scheme of Fig. 1a) and results in the disappearance of switching.

As is known, the capacitance of an insulator (C_i) is constant, while the capacitance of a space charge region (C_D) varies depending on the surface potential [7], the latter being controlled by the applied bias voltage U_0. When the measurements are performed at 6 kHz with $U_0 < -12.2$ V, the system occurs in the regime of strong inversion, while $U_0 > 4.6$ V corresponds to the regime of enrichment, both these states characterized by increasing capacitance of the space charge region. Under these conditions, $C_{iD} \approx C_D$ (according to our calculations, $C_D \sim 10^{-9}$ F).

Illumination of the sample gives rise to a photocapacitive effect well known in metal–insulator–semiconductor structures [8] irradiated within the intrinsic absorption wavelength band of the semiconductor component. The photoelectrons contribute to the density of inversion mobile electrons (Fig. 1a) in the vicinity of the Si–SiO_2 interface. As a result, the width of the space charge region decreases and the capacitance of this region under the illuminated interelectrode gap increases.

Thus, we have studied a new regime of operation of the vanadium dioxide based switch implementing a Si–SiO_2–VO_2 structure, in which the dynamics of switching can be controlled by applying a bias voltage U_0 to the substrate and/or by illuminating the VO_2 film surface. The structure featuring these effects can be used as a basis for the development of new semiconductor devices analogous to thyristors and photothyristors. Since the structures with switching can be also used as autooscillators [9], the Si–SiO_2–VO_2 system can be used for creating light sensors with a frequency-dependent response. By decreasing the interelectrode gap width (e.g., with the aid of photolithography [10]), it is possible to significantly reduce the switching time of a planar VO_2 based switch. In a submicron switching channel operating at low temperature, an important role is played by the field effects [3]. This can be used to expand the frequency range of devices based on the Si–SiO_2–VO_2 system. A change in the optical properties of VO_2 upon the MIPT can be promising in developing optoelectronic devices based on such structures.

Acknowledgments. This study was supported by the Ministry of Education of the Russian Federation (project nos. PD-1.2-283 and UR.01.01.038) and by the US Civilian Research and Development Foundation for the Independent States of the Former Soviet Union (CRDF Award No. PZ-013-02).

REFERENCES

1. A. A. Bugaev, B. P. Zakharchenya, and F. A. Chudnovskiĭ, *Metal–Semiconductor Phase Transition and Its Application* (Nauka, Leningrad, 1979).

2. A. A. Bugaev, S. E. Nikitin, and E. I. Terukov, Pis'ma Zh. Tekh. Fiz. **27** (21), 76 (2001) [Tech. Phys. Lett. **27**, 924 (2001)].
3. P. P. Boriskov, A. A. Velichko, A. L. Pergament, *et al.*, Pis'ma Zh. Tekh. Fiz. **28** (10), 13 (2002) [Tech. Phys. Lett. **28**, 406 (2002)].
4. G. Stefanovich, A. Pergament, and D. Stefanovich, J. Phys.: Condens. Matter **12**, 8837 (2000).
5. A. A. Velichko, N. A. Kuldin, and G. B. Stefanovich, in *Proceedings of Int. Conf. "Physics of Materials for Electronics," Kaluga, 2002*, pp. 362–363.
6. A. A. Velichko and N. A. Kuldin, in *Abstracts of Int. Conf. "Lomonosov-2002," Moscow, 2002*, p. 191.
7. S. Sze, *Physics of Semiconductor Devices* (Wiley, New York, 1981; Mir, Moscow, 1984).
8. N. A. Pennin, Fiz. Tekh. Poluprovodn. (St. Petersburg) **34** (5), 562 (2000) [Semiconductors **34**, 545 (2000)].
9. I. M. Vikulin and V. I. Stafeev, *Physics of Semiconductor Devices* (Radio i Svyaz', Moscow, 1990).
10. A. L. Pergament, G. B. Stefanovich, A. A. Velichko, *et al.*, in *Abstracts of the All-Russia Sci. Conf. on the Low-Temperature Plasma Physics, Petrozavodsk, 2001*, p. 169.

Translated by P. Pozdeev

Technical Physics Letters, Vol. 29, No. 6, 2003, pp. 510–512. Translated from Pis'ma v Zhurnal Tekhnicheskoĭ Fiziki, Vol. 29, No. 12, 2003, pp. 54–61.

Gyro-Backward-Wave Oscillator Synchronized by Distributed External Action

A. A. Koronovskiĭ* and A. E. Khramov

Saratov State University, Saratov, Russia
State Scientific Center "College", Saratov, Russia
** e-mail: alkor@cas.ssu.runnet.ru*

Received January 10, 2003

Abstract—The possibility of synchronizing oscillations in a gyro-backward-wave tube (gyro-BWT) by means of distributed introduction of a control signal into the interaction space has been theoretically studied for the first time. It is established that the use of coupled waveguide systems for this purpose allows the synchronization bandwidth to be significantly increased as compared to the case when the external control signal is fed to the input of the interaction space (the collector end of a gyro-BWT). © *2003 MAIK "Nauka/Interperiodica".*

Problems related to the synchronization of distributed autooscillation systems are of considerable interest in modern microwave electronics. Among these problems, of special importance is the task of synchronizing oscillations in a system of the "helical electron beam–backward electromagnetic wave" type (cyclotron resonance maser) [1–5]. Questions pertaining to the synchronization of autooscillations in a gyro-backward-wave tube (gyro-BWT) with an external control signal introduced at the collector end were considered in detail previously [4–7]. These investigations revealed the main laws of synchronization and nonautonomous spatiotemporal dynamics of the active medium containing a helical electron beam in the case of a "lumped" external action.

The most important features of synchronization in distributed electron systems (in particular, in gyro-BWT) include the appearance of quasisynchronization regimes (manifested by complication of the spectral composition of the output signal of a synchronized microwave oscillator [4, 7]) and the complication of spatial dynamics in the nonautonomous distributed system [5, 7]. The latter phenomenon is observed in a gyro-BWT under the action of a harmonic control signal with amplitude F_0 and frequency Ω introduced at one end of the interaction space ($\xi = A$, where A is the interaction space length of the gyro-BWT). The character of changes in the spatial dynamics consists in the appearance of oscillation modes at the external signal frequency in the synchronization and quasisynchronization regimes. The escape from a quasisynchronization regime is accompanied by the formation of two characteristic regions in the interaction space, featuring different frequencies of the field oscillations. The first of these regions (with the length A_s called the synchronization length [5, 7]), occurring at the gyro-BWT input, features oscillations at a frequency (Ω) of the external control action. The second region features breakage of the induced oscillations (breakdown of synchronization), whereby the base oscillation frequency ω deviates from Ω on approaching the system output ($\xi = 0$). Accordingly, the boundary of the quasisynchronization wedge is determined by equality of the synchronization length to the total interaction space length ($A_s \equiv A$).

An analysis shows that one possible means of expanding the gyro-BWT synchronization bandwidth consists in maintaining the synchronization regime in a distributed active medium of the "helical electron beam–backward wave" type by providing for the control signal action along the whole system (distributed external action). Such a distributed action can be implemented by a distributed signal input via coupled waveguide systems (CWSs).

Recently [8] we have studied the system of gyro-BWT with CWSs in detail and obtained a system of working equations describing processes in such systems (see also the monographs [9, 10] devoted to the devices with extended interaction of the *O*-type and CWSs). These relationships include the conditions of excitation for each waveguide system and the equations of motion for oscillating electrons in the helical beam:

$$\frac{\partial F_1}{\partial \tau} - \frac{\partial F_1}{\partial \xi} - j\alpha F_2 = -\frac{1}{2\pi}\int_0^{2\pi} \beta d\theta_0, \tag{1}$$

$$\frac{\partial F_2}{\partial \tau} - \frac{\partial F_2}{\partial \xi} - j\alpha F_1 = 0, \tag{2}$$

$$d\beta/d\xi - j\mu(1 - |\beta|^2)\beta = F_1, \tag{3}$$

$$F_1(\xi = A) = 0, \quad F_2(\xi = A) = F_3,$$
$$\beta(\xi = 0) = \exp(j\theta_0), \quad \theta_0 \in [0, 2\pi]. \tag{4}$$

1063-7850/03/2906-0510$24.00 © 2003 MAIK "Nauka/Interperiodica"

In writing these equations, it was assumed that the helical beam passes through the first waveguide system. The initial conditions (4) correspond to an external synchronizing signal $F_3 = F_0\exp[j\Omega\tau]$ fed to the input ($\xi = A$) of the second waveguide system. In Eqs. (1)–(4), $F_{1,2}$ are quantities proportional to the slowly varying complex field amplitudes in the first and second waveguide systems, respectively; α is the coupling parameter [8]; $\beta = r\exp(j\theta)$ is the complex radius of the electron trajectory in a helical beam; μ is the parameter of nonisochronism of the oscillating electrons [11, 12]; and ξ and τ are the dimensionless longitudinal coordinate and time, respectively. The simplifying assumptions underlying the proposed model and the expressions for dimensionless variables are considered in detail elsewhere [8, 12].

Let us consider a gyro-BWT synchronized by a distributed external action under the same conditions and control parameters ($\mu = 2.0$, $A = 3.0$) as in [4, 7], where the signal was introduced at the collector end of the tube.

Figure 1a shows the plots of the normalized synchronization bandwidth $\Delta\omega/\Delta\omega_0$ for a gyro-BWT with distributed introduction of the external high-frequency control signal versus coupling coefficient α for various amplitudes F_0 of the external action. Here, the synchronization bandwidth $\Delta\omega$ is normalized to the quasisynchronization bandwidth $\Delta\omega_0$ for the gyro-BWT under the action of a control signal with the same amplitude F_0 fed to the collector end (see [4, 5, 7]). As can be seen from these data, the width $\Delta\omega$ of the synchronization band (i.e., the band where the external signal frequency locks the base frequency of the gyro-BWT) in the system with distributed external action significantly increases in a certain interval of the coefficient of coupling between waveguide systems through which the control signal acts upon the active medium (i.e., upon the helical electron beam). When the external signal amplitude is small (Fig. 1a, $F_0 = 0.05$) the synchronization bandwidth increases ($\Delta\omega > \Delta\omega_0$) for $\alpha > 0.25$. As the control signal intensity grows, the interval of α values in which the synchronization bandwidth increases exhibits narrowing ($0.35 < \alpha < 0.8$). The increase in F_0 is also accompanied by a decrease in the normalized synchronization bandwidth $\Delta\omega/\Delta\omega_0$.

Expansion of the synchronization bandwidth in the system with distributed introduction of the control signal is explained by peculiarities of the physical processes in a nonautonomous gyro-BWT. In the case of a "lumped" introduction of the control signal at the collector end, the external field acts upon a well-bunched electron beam. In contrast, the distributed synchronizing field acts upon the helical beam along the entire length of the interaction space. The latter case provides conditions for an effective modulation of the helical beam at the control signal frequency even near the tube output (where electrons are weakly bunched). A helical beam grouped due to phase modulation of the ensemble

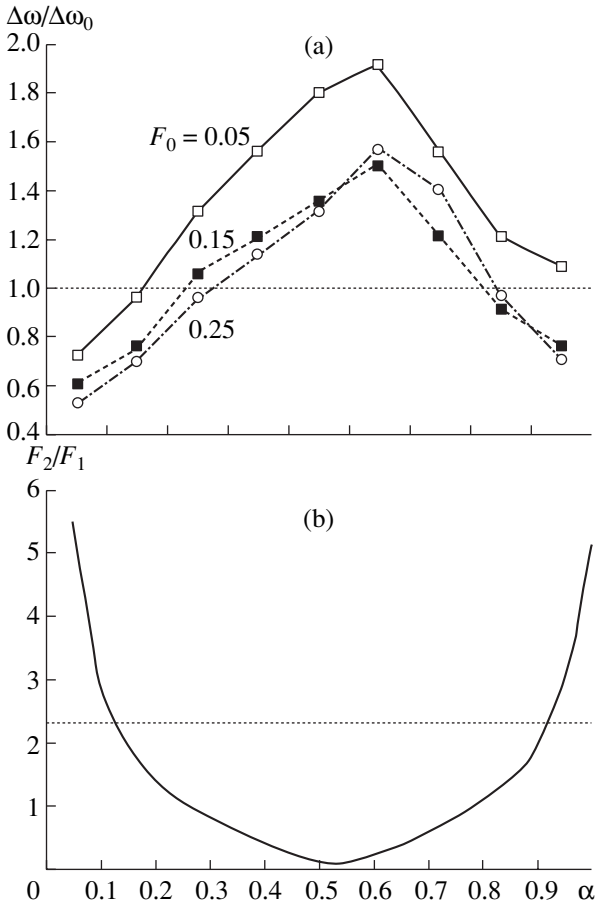

Fig. 1. Plots of (a) the normalized synchronization bandwidth $\Delta\omega/\Delta\omega_0$ for various amplitudes F_0 of the external action and (b) the field amplitude ratio F_2/F_1 at the CWS outputs in the absence of the electron beam versus waveguide coupling coefficient α for a gyro-BWT–CWS system with distributed introduction of the external high-frequency control signal.

of oscillating electrons exhibits a more rapid buildup of the grouped current harmonic (with the control signal frequency Ω) toward the collector end as compared to the case when a control signal of the same intensity is introduced at the input of the interaction space ($\xi = A$). As a result, the synchronization length A_s in the system with distributed external action increases up to the total length of the interaction space within a frequency interval $\Delta\omega$ exceeding that ($\Delta\omega_0$) for the "lumped" external action on the same system.

Thus, the synchronization bandwidth in the system with distributed introduction of the control signal significantly increases, provided optimum coupling between CWSs. For the gyro-BWT considered above (with $A = 3.0$), the optimum coupling coefficient $\alpha \approx 0.65$ provides for a (1.5–2)-fold increase in the synchronization bandwidth in the system with distributed external action relative to the gyro-BWT with "lumped" action (at the collector end). In the general

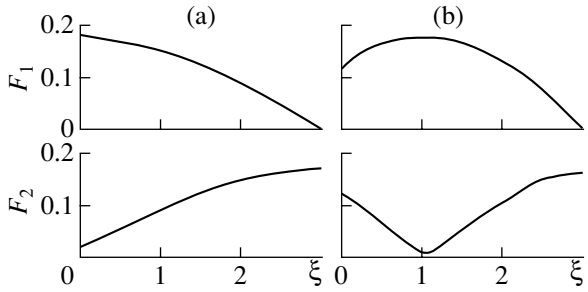

Fig. 2. High-frequency field amplitude profiles in the interaction space for "cold" CWSs with $\alpha = 0.5$ (a) and 0.8 (b). The external field with a frequency equal to that of the autonomous gyro-BWT operation is fed to the second waveguide system input ($\xi = A = 3.0$).

case, the optimum α value is determined by features of the high-frequency power redistribution between the two CWSs.

Figure 1b shows a plot of the F_2/F_1 ratio at the system output ($\xi = 0$) versus the coupling coefficient α (F_1 and F_2 are the field amplitudes in the "cold" waveguide systems without the electron beam). The external field with amplitude F_0 and a frequency equal to that of the autonomous gyro-BWT operation is fed to the second waveguide system: $F_1(\xi = A) = 0$, $F_2(\xi = A) = F_0$. As can be seen, only a part of the high-frequency power is pumped from the second to first waveguide system when the coupling coefficient is small. In a gyro-BWT synchronized via a CWSs with such α value, the effective field power acting upon the electron beam decreases as a result of incomplete pumping into the interaction space.

The same system with $\alpha \sim 0.4$–0.7 features almost complete pumping of the high-frequency power from one to another waveguide system. This is illustrated in Fig. 2a showing the field distribution along the interaction space in each of the "cold" CWSs for the coupling coefficient $\alpha = 0.5$. As can be seen, virtually all power of the signal fed to the second waveguide system is transferred to the first system: $F_1(\xi = 0) \approx F_0$, $F_2(\xi = 0) \approx 0$. In this case, the synchronization bandwidth is maximum: the whole power of the external synchronizing signal acts upon the helical electron beam along the entire length of the interaction space.

In the case of large coupling coefficients ($\alpha > 0.6$), the system features reverse pumping of the high-frequency power from first to second waveguide system and the field amplitude at the second output begins to grow (Fig. 1b). As can be seen from Fig. 2b showing the field profiles for $\alpha = 0.8$, virtually complete pumping of the high-frequency power to the first waveguide system takes place over a length of $\xi = (2/3)A$, after which the reverse pumping begins. This is equivalent to a decrease in the effective length of the interaction space in which the external field acts upon the electron beam (for $\alpha = 0.8$, this decrease amounts to $(1/3)A$). As a result, the gyro-BWT synchronization bandwidth decreases. In the case of large coupling coefficients ($\alpha > 0.9$–1.1), the length of the interaction space in which the high-frequency power is effectively pumped from one to another accounts for a small part of the interaction space and the synchronization bandwidth drops especially sharply (significantly below the $\Delta\omega_0$ value for the system with "lumped" introduction of the external signal).

In conclusion, it should be noted that gyro-BWTs operating in a synchronized regime with distributed introduction of the external signal are characterized by increased generation efficiency. For the optimum coupling coefficient ($\alpha = 0.65$), the efficiency reached $\eta = 23.2\%$ (against 18.7% in an autonomous regime).

Acknowledgments. This study was supported by the Russian Foundation for Basic Research (project nos. 02-02-16351 and 01-02-17392).

REFERENCES

1. C. S. Kou, S. H. Chen, L. R. Barnett, *et al.*, Phys. Rev. Lett. **70**, 924 (1993).
2. A. H. McCurdy, Appl. Phys. Lett. **66**, 1845 (1995).
3. K. L. Felch, B. G. Danly, H. R. Jory, *et al.*, Proc. IEEE **87** (5), 752 (1999).
4. D. I. Trubetskov and A. E. Khramov, Pis'ma Zh. Tekh. Fiz. **28** (18), 34 (2002) [Tech. Phys. Lett. **28**, 767 (2002)].
5. D. I. Trubetskov and A. E. Khramov, Izv. Ross. Akad. Nauk, Ser. Fiz. **66** (12), 1761 (2002).
6. A. A. Koronovskiĭ, I. S. Rempen, D. I. Trubetskov, and A. E. Khramov, Izv. Ross. Akad. Nauk, Ser. Fiz. **66** (12), 1754 (2002).
7. A. A. Koronovskiĭ, D. I. Trubetskov, and A. E. Khramov, Izv. Vyssh. Uchebn. Zaved., Radiofiz. **45** (9), 773 (2002).
8. A. A. Koronovskiĭ and A. E. Khramov, Pis'ma Zh. Tekh. Fiz. **29** (4), 63 (2003) [Tech. Phys. Lett. **29**, 160 (2003)]; A. A. Koronovskiĭ, D. I. Trubetskov, and A. E. Khramov, Zh. Tekh. Fiz. **73** (6), 110 (2003) [Tech. Phys. **48**, 768 (2003)].
9. W. H. Louisell, *Coupled Mode and Paramagnetic Electronics* (Wiley, New York, 1960; Inostr. Lit., Moscow, 1963).
10. D. I. Trubetskov, in *Lectures on Microwave Electronics and Radiophysics: Proceedings of the 3rd Winter School-Workshop for Engineers* (Saratov. Univ., Saratov, 1978), Part 5, p. 89.
11. A. Yu. Dmitriev, D. I. Trubetskov, and A. P. Chetverikov, Izv. Vyssh. Uchebn. Zaved., Radiofiz. **34** (9), 595 (1991).
12. A. Yu. Dmitriev, A. E. Konevets, L. A. Pishchik, *et al.*, in *Lectures on Microwave Electronics and Radiophysics: Proceedings of 7th Winter School-Workshop for Engineers* (Saratovskiĭ Univ., Saratov, 1986), Part 3, p. 61.

Translated by P. Pozdeev

Technical Physics Letters, Vol. 29, No. 6, 2003, pp. 513–515. Translated from Pis'ma v Zhurnal Tekhnicheskoĭ Fiziki, Vol. 29, No. 12, 2003, pp. 62–67.

Selective Effect of Weak Electromagnetic Field on Ferroelectric Crystals with Hydrogen Bonds

M. N. Levin*, V. V. Postnikov, and M. Yu. Palagin

Voronezh State University, Voronezh, Russia

** e-mail: levin@lev.vsu.ru*

Voronezh State Technical University, Voronezh, Russia

Received January 16, 2003

Abstract—It is found that the ferroelectric crystals of triglycine sulfate and potassium dihydrogen phosphate are selectively sensitive to a weak electromagnetic field. The effect detected is supposed to be associated with the decay of defect complexes stabilized by hydrogen bonds. *© 2003 MAIK "Nauka/Interperiodica".*

Recently, we found that the short-term impact of weak pulsed magnetic field causes long-term changes in the ferroelectric and dielectric characteristics of nominally pure triglycine sulfate crystals [1]. However, the questions of what ferroelectric crystals can exhibit such behavior and whether the pulsed character of the magnetic field action is a necessary condition for this effect still remain open.

In order to clarify these questions, we have studied the effect of weak constant magnetic fields on hydrogen-containing and oxygen-octahedral ferroelectric crystals. As the objects for investigation, we chose the triglycine sulfate (TGS), potassium dihydrogen phosphate (KDP), and barium titanate ($BaTiO_3$) crystals, which are known as model ferroelectrics [2].

The TGS and KDP samples were cut from the corresponding nominally pure single crystals grown by temperature-controlled cooling of supersaturated aqueous solutions. These samples had the shape of rectangular plates $7 \times 7 \times 0.5$ mm in size with the polar *Y* axis perpendicular to the large faces of the plates. The samples of $BaTiO_3$ single crystals with dimensions of $2 \times 4 \times 0.3$ mm were grown from the KF melt. Silver film electrodes on the large faces of the samples of all three types were formed by thermal deposition in vacuum.

The samples were exposed to a magnetic field in the gap between two sets of magnetized ferrite plates. The value of magnetic induction, as determined by the gap width, could be varied from 0.02 to 0.2 T and measured by a magnetometer with the Hall probe. Each sample was exposed to magnetic field for 30 min at any value of the magnetic induction. The samples of KDP, TGS, and $BaTiO_3$ in the ferroelectric state were exposed to a magnetic field at temperatures of 77, 293, and 350 K, respectively. The TGS and KDP samples were oriented in the magnetic fields in two different ways, so that the polar *Y* axis was either parallel or perpendicular to the magnetic field lines. The TGS and $BaTiO_3$ samples were treated and kept in air, while the KDP samples were always contained in a special vacuum cryostat.

Before and after the exposure magnetic field, we measured the temperature dependences $\varepsilon'(T)$ of the active component of the dielectric permittivity in the vicinity of the ferroelectric transitions in the crystals studied. The permittivity was measured at a frequency of $\omega = 10^4$ Hz using a Tesla BM 484 bridge. The temperature was measured by a platinum resistance thermometer with an accuracy of $\leq 2.5 \times 10^{-3}$ K. The samples were heated at a controlled rate, equal to 1.5 K/h in the vicinity of the Curie temperature T_C for each ferroelectric crystal.

The main results of this investigation are shown in Fig. 1 and consist in the following. The exposure to magnetic field significantly changes the $\varepsilon'(T)$ curves for TGS and KDP samples, lowering the ferroelectric transition temperature by $\Delta T_C = 0.8 \pm 0.1$ K and multiplying the height of the permittivity peak at the Curie point. For the TGS samples, this effect was observed when the polar *Y* axis of the sample was perpendicular to the magnetic field lines, and it was absent when this axis was oriented along the magnetic field. By contrast, this effect in the KDP samples occurred when the polar *Y* axis was directed along the field and was absent when this axis was perpendicular to the field. At the same time, exposure to magnetic fields in the entire range of magnetic fields studied cause no changes in the characteristics of $BaTiO_3$ samples.

The observed changes in the $\varepsilon'(T)$ characteristics of the TGS and KDP samples have a long-term character, relaxing at room temperature for several days after the exposure to magnetic field. A specific feature of the effect reported is its selective character, whereby the observed phenomena are manifested in a narrow range of the magnetic induction. Dependences of the Curie temperature shift ΔT_C and the relative permittivity maximum $\varepsilon'_m/\varepsilon'_{m0}$ at the ferroelectric transition temperature

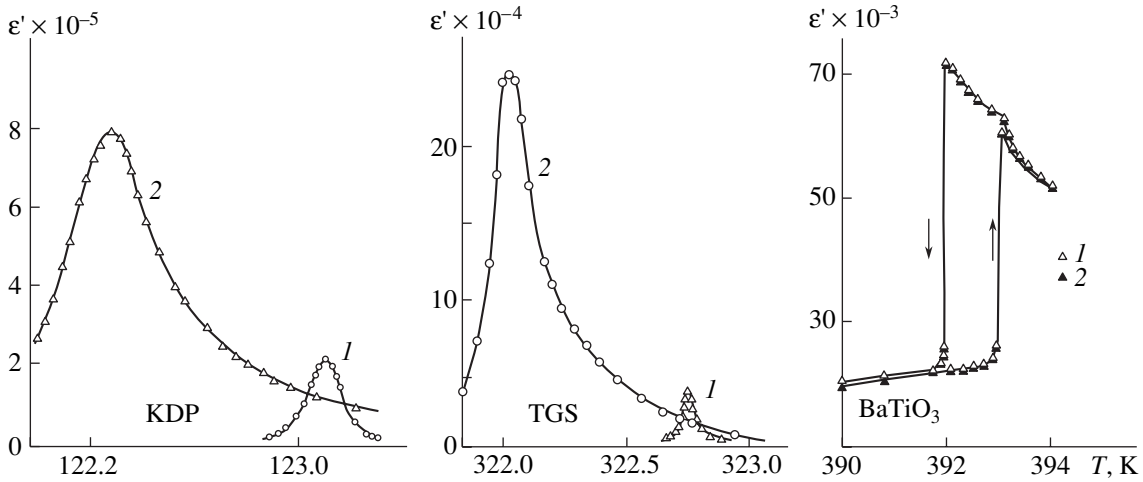

Fig. 1. Temperature dependences of the permittivity ε'(*T*) of KDP, TGS, and $BaTiO_3$ crystals (*1*) before and (*2*) after the exposure to magnetic field (*B* = 0.08 T, 30 min).

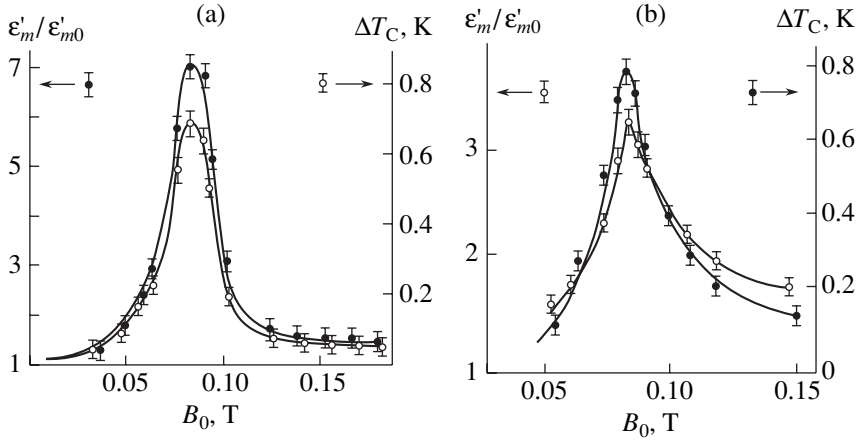

Fig. 2. Dependences of the Curie temperature shift ΔT_C and the relative permittivity maximum $\varepsilon'_m/\varepsilon'_{m0}$ at the phase transition temperature on the magnetic field induction for the (a) TGS and (b) KDP crystals. The magnetic field exposure time was 30 min for all values of the magnetic induction.

on the magnetic induction for the TGS and KDP crystals are shown in Fig. 2.

The obtained results provide unambiguous answers to the above questions. First, the magnetic field induced effects are observed in the hydrogen-containing crystals and are absent in ferroelectrics of the oxygen-octahedral type. Second, the pulsed character of the magnetic field is not a necessary condition for the effects found.

The new experimental results do not contradict our previous interpretation [1] of the magnetic field induced effects in TGS crystals. According to this, the increase in the permittivity of the magnetic field treated samples is related to an increase in the mobility of domain walls due to their depinning from the defects acting as stoppers, while the shift of the Curie point is caused by a decrease in the internal field strength due to the disorientation of the polar defects initially pinned to the domain walls. Within the framework of this interpretation, a necessary condition for the magnetic field induced effects is the existence of defect complexes in the initial crystals which can decompose under the magnetic field action into mobile point defects capable of forming a new defect structure. In other words, the magnetic field induced effects, which are impossible in perfect crystals without magnetic order, can take place in real crystals with a certain imperfection.

Unfortunately, defects responsible for the pinning of domain walls and the formation of an internal field in the nominally pure (undoped) TGS and KDP crystals are not identified on a microscopic level, which hinders modeling of the observed effects. Nevertheless, this study provides additional experimental data for the discussion of the nature of these effects.

The similarity of the effects observed in various hydrogen-containing ferroelectrics and their total

absence (in the same range of field strengths) in a ferroelectric crystal of another type suggest that hydrogen bonds probably participate in the observed phenomenon. This assumption is confirmed by the selective character of these effects occurring in a narrow range of the magnetic induction. Chemistry and molecular physics contain spin-dependent reactions of radical pairs, which are selectively sensitive to a weak magnetic field [3]. It is believed that such reactions in constant magnetic fields are possible only if a radical pair contains at least one nucleus with a nonzero spin involved into intercombination transitions through the mechanism of the hyperfine interaction [4]. It would be natural to assume that the selective sensitivity of the TGS and KDP crystals to the magnetic induction is caused by participation of the hydrogen bond protons in the spin-dependent processes of the transformation of defect complexes in real crystals.

In conclusion, it should be pointed out that the ferroelectric properties of the crystals studied make it easier to observe the magnetic field induced effects but are not a necessary condition for their appearance. It is quite probable that the selective sensitivity to magnetic field will be detected in nonferroelectric molecular crystals with hydrogen bonds.

REFERENCES

1. M. N. Levin, V. V. Postnikov, M. Yu. Palagin, and A. M. Kostsov, Fiz. Tverd. Tela (St. Petersburg) **45**, 513 (2003) [Phys. Solid State **45**, 542 (2003)].
2. M. E. Lines and A. M. Glass, *Principles and Applications of Ferroelectrics and Related Materials* (Oxford Univ. Press, Oxford, 1977; Mir, Moscow, 1981).
3. Ya. B. Zel'dovich, A. L. Buchachenko, and E. L. Frankevich, Usp. Fiz. Nauk **155** (3), 3 (1988) [Sov. Phys. Usp. **31**, 385 (1988)].
4. K. M. Salikhov, Yu. N. Molin, R. Z. Sagdeev, and A. L. Buchachenko, *Spin Polarization and Magnetic Effects in Radical Reactions* (Elsevier, Amsterdam, 1984) [Russian original: A. L. Buchachenko, R. Z. Sagdeev, and K. M. Salikhov, *Magnetic and Spin Effects in Radical Reactions* (Nauka, Novosibirsk, 1978)].

Translated by M. Basieva

Technical Physics Letters, Vol. 29, No. 6, 2003, pp. 516–518. Translated from Pis'ma v Zhurnal Tekhnicheskoĭ Fiziki, Vol. 29, No. 12, 2003, pp. 68–73.

The Primary Macrofragmentation of Shear in Compressed Aluminum Single Crystals

D. V. Lychagin and L. A. Teplyakova

Tomsk State Architecture Building University, Tomsk, 634003 Russia

e-mail: dvl-tomsk@mail.ru

Received February 7, 2003

Abstract—We have experimentally studied the pattern of a deformation relief formed on the side faces of an aluminum single crystal in the initial stages of plastic straining. The single crystal sample exhibits the formation of macroscopic fragments differing by organization of the shear process. The main factors determining the character of this macrofragmentation are considered. © *2003 MAIK "Nauka/Interperiodica".*

The phenomenon of macrofragmentation in single crystals subjected to compressive straining, whereby a sample exhibits regions with different organization of the shear process, has been reported by many researchers. However, it was not until the past decade that these regions (called shear fragments or domains) have become the objects of independent investigation. On a macroscopic level, shear fragments have been studied in single crystals of some fcc metals and alloys such as nickel, copper, aluminum, Ni_3Fe alloy (in both ordered and disordered states), and Ni_3Ge (intermetallic compound) [1–4]. Recently [5] it was established that the phenomenon of shear fragmentation takes place in a broad range of scales, from the macroscopic to microscopic level. It was experimentally demonstrated that, as the degree of straining increases, the formation of shear fragments is followed by the appearance of bending-torsion and rotation fragments. The boundaries of these fragments may serve as the sites of formation of superlocalized strain bands [6].

The laws governing the formation of macrofragments are still insufficiently studied, and not all factors determining the morphology of these fragments have been established. Detailed investigation of the phenomenon of fragmentation is obviously important for description of plastic straining as a process proceeding on various structural and dimensional levels, including the macroscopic level. In this context, we have studied the laws of shear macrofragmentation in single crystals subjected to compressive straining.

The experiments were performed on aluminum single crystals oriented so that the axis of compression coincided with the [001] direction; the side faces had a {110} orientation. The samples had the shape of parallelepipeds with linear dimensions of $3 \times 3 \times 6$ mm. The crystal orientation was checked by X-ray diffraction on an IRIS-3 setup with an error not exceeding 2°. The samples were compressively strained at room temperature in an Instron testing machine operated at a rate of 3×10^{-4} s^{-1}. It should be noted that investigations of the deformation relief are most frequently performed on samples strained in the tension mode. However, evolution of the pattern of shear in compressed crystals is also of considerable interest, since this case represents the configuration of principal stresses and strains analogous to that encountered in forging and rolling–the most frequently employed methods of metal processing by pressure [7]. The pattern of deformation relief over the whole crystal sample was studied using a scanning electron microscope of the Tesla-BS301 type.

For the compression axis orientation used in our experiments, there are 8 (or 16 with allowance of the opposite shear signs) equiloaded octahedral slip systems. Under these conditions, one can expect that three systems of shear traces—two sloped and one horizontal—will appear on each side face of the sample. In particular, the sloped trace systems on the (110) face are due to the shear along $(\bar{1}11)$ and $(1\bar{1}1)$ planes, while the horizontal systems are due to the shear along (111) and $(11\bar{1})$ planes. Assuming that the main macroscopic shear proceeds only by two (of the four) families of octahedral planes, which are oriented symmetrically relative to the compression axis, the single crystal can be subdivided into volumes as depicted in Fig. 1. In the $V_{2A} + V_3 + V'_{2A}$ and $V_{2B} + V_3 + V'_{2B}$ macrovolumes, the octahedral shear planes emerge on all side faces of the sample, while in macrovolumes V_1 and V'_1 the shear planes on one side contact with plungers of the testing machine. Finally, macrovolumes V_4 and V'_4 emerge at the free surfaces on three sides of the crystal. Accordingly, the motion of shear carriers in the first case can proceed toward the free surfaces in all four directions (with allowance of the opposite shear signs); in the volumes contacting plungers of the testing machine, the

1063-7850/03/2906-0516$24.00 © 2003 MAIK "Nauka/Interperiodica"

motion of carriers toward the contact surface is hindered.

Figure 2 shows a schematic diagram of the typical pattern of a deformation relief formed on two mutually perpendicular faces of the single crystal strained to a small extent. As expected, there are three systems of shear traces. Despite the high symmetry of the axis of loading, the systems of shear traces developed differently on various crystal faces. On the (110) face, one of the sloped shear trace systems is more developed than the other. The maximum part of traces of this system is localized in the region bounded by exits of the parallel octahedral planes passing through opposite vertices of the face (i.e., the shear proceeded in the $V_{2A} + V_3 + V'_{2A}$ macrovolumes, Fig. 1). This region has a high density of shear traces and is visually manifested as a shear macroband. The second in extent of development is another sloped shear trace system, which results from the shear proceeding in the $V_{2B} + V_3 + V'_{2B}$ macrovolumes. This system, with the density of traces being lower as compared to the first one, is essentially secondary and appears also as a shear macroband. The third system of shear traces (representing horizontal layers) is localized predominantly in the top and bottom parts of the (110) face (Fig. 2) and characterized by a relatively low density of traces.

Thus, in aluminum single crystals oriented for the multiple slip, the shear is localized from the very onset of plastic straining in certain regions of the crystal, evidencing fragmentation on a macroscopic level. It should be emphasized that, despite the high symmetry of the single crystal orientation, the macroscopic localization of shear proceeds only in two of the four equiloaded octahedral slip planes, and even these are differently manifested. In other words, compressive straining of a highly symmetric single crystal is accompanied by significant asymmetry in the shear development in the scale of the whole sample. The possible reasons for this shear asymmetry are as follows: (i) minor deviations from exact orientation; (ii) uncontrollable nonparallelism of the testing machine plungers relative to each other and with respect to the sample edges; (iii) uneven edge surfaces leading to spot contacts. Any one of these factors would predetermine the appearance of shear asymmetry under usual straining conditions. However, it is difficult to predict a priori which of these shear systems will start operating first. Once appearing, the shear asymmetry is manifested in the primary fragment morphology: straining developed in one shear system of a given fragment hinders the development of shear in the other systems.

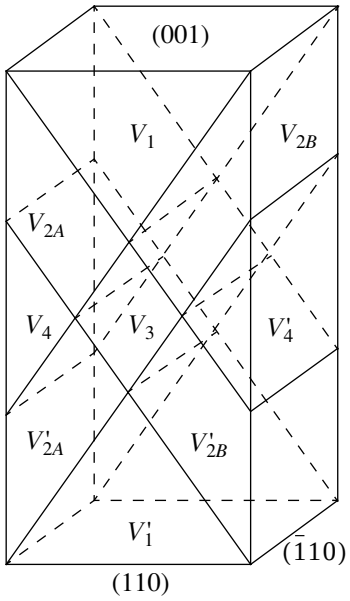

Fig. 1. A schematic diagram illustrating selected macrovolumes for macroscopic shear along two families of octahedral planes in a strained fcc single crystal with {110} side faces compressed along the [001] direction.

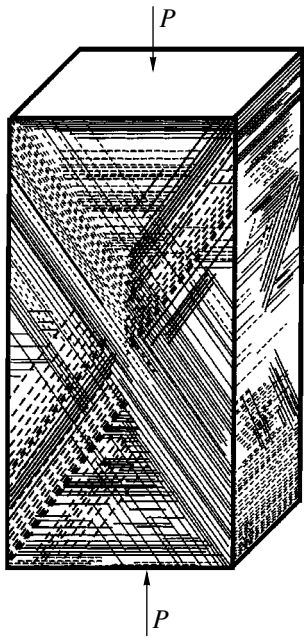

Fig. 2. A schematic diagram showing the pattern of a deformation relief manifested on two mutually perpendicular faces of an aluminum single crystal strained to $\varepsilon = 0.05$ (solid and dashed lines representing light and dark traces, respectively).

As is known [7], a sample subjected to compressive straining may feature the realization of different schemes of principal stresses in adjacent regions. In the near-edge regions, the friction between plunger and sample leads to the scheme of hydrostatic compression, whereas the central region of a moderately strained sample with height greater than width exhibit uniaxial compression. A comparison of these schemes to the pattern of localization of the shear trace systems (Fig. 2) and the diagram of macrovolumes (Fig. 1) leads to the conclusion that the shape of macrofrag-

ments in the case of compressive straining is uniquely determined by the sample shape and the mutual orientation of the compression axis and single crystal faces (i.e., by the crystal geometry characteristics). This fragmentation, naturally called primary, is developed from the very onset of plastic straining. The primary fragments (macrofragments) appeared as most coarse among all formed in the single crystals studied under plastic shear straining conditions. The linear dimensions of these fragments are comparable with the single crystal dimensions.

In the analysis of such data, it is especially important to take into account the crystallographic orientation of side edges of a single crystal sample. Indeed, the results of our study showed that the mutual orientation of the shear direction and the side crystal faces determines the crystal region in which the shear starts developing and the dimensions of macrofragments. The most intensive shear is observed in those macrovolumes where the shear axis passes between free crystal surfaces.

REFERENCES

1. V. A. Starenchenko, L. G. Chernykh, and N. Yu. Ivanova, Izv. Vyssh. Uchebn. Zaved., Fiz., No. 8, 116 (1989).
2. Yu. A. Abzaev, V. A. Starenchenko, Yu. V. Solov'eva, *et al.*, Prikl. Mekh. Tekh. Fiz. **39**, 154 (1998).
3. L. A. Teplyakova, T. S. Kunitsyna, N. A. Koneva, *et al.*, Fiz. Mezomekh. **3** (5), 77 (2000).
4. L. A. Teplyakova, R. V. Shaekhov, and D. V. Lychagin, *Modern Problems of Materials Strength. Proceedings of the 2nd International Seminar* (Novgorod. Gos. Univ., Novgorod, 2001), Vol. 1, pp. 168–172.
5. L. A. Teplyakova, Author's Abstract of Doctoral (Phys.–Math.) Dissertation (Tomsk, 1999).
6. V. A. Starenchenko, Author's Abstract of Doctoral (Phys.–Math.) Dissertation (Tomsk, 1991).
7. S. I. Gubkin, *Plastic Deformation of Metals* (Metallurgizdat, Moscow, 1961), Vol. 1.

Translated by P. Pozdeev

Technical Physics Letters, Vol. 29, No. 6, 2003, pp. 519–520. Translated from Pis'ma v Zhurnal Tekhnicheskoĭ Fiziki, Vol. 29, No. 12, 2003, pp. 74–77.

The Relationship between Plastic Flow Macrolocalization and a Dislocation Structure

L. B. Zuev, T. M. Poletika, and G. N. Narimanova

Institute of Strength Physics and Materials Science, Siberian Division, Russian Academy of Sciences, Tomsk, 634055 Russia

e-mail: levzuev@mail.tomsknet.ru

Received January 15, 2003

Abstract—We have established a quantitative relationship between the spatial period of localization of plastic straining and the parameters of the dislocation structure of a zirconium alloy. It is found that the wavelength of localized straining is proportional to the average size of elements of a dislocation substructure formed in the material in various stages of plastic flow. A quantitative interpretation of this relationship is proposed. *© 2003 MAIK "Nauka/Interperiodica".*

The problem of interrelation between the macroscopic localization of plastic straining and the dislocation characteristics of a deformable medium has been considered for a rather long time [1–4]. However, the lack of direct experimental evidence hindered establishing the form and understanding the nature of such a relationship.

In the present study performed on polycrystalline samples of a zirconium-based alloy (1 wt % Nb, 0.4 wt % Fe, 1.2 wt % Sn) [5] with a grain size of ~3.5 μm, this relationship was analyzed by comparing the wavelength λ of localized straining (determined according to [6] as the distance between the active foci of plastic straining in the stage of parabolic strengthening) and the average size $\bar{d}$ of elements of a dislocation structure for the same level of total straining.

The latter characteristic ($\bar{d}$) was determined (in various stages of straining of the sample alloy) with the aid of electron microscopy (thin foil technique). These data indicated that the material studied exhibits the following sequence of transformations of the dislocation substructures: chaotic distribution of dislocations ⟶ dislocation pileups ⟶ network substructure ⟶ cellular network substructure ⟶ band substructure ⟶ substructure with continuous and discrete misorientations ⟶ fragmented structure [7]. The average characteristic size $\bar{d}$ of elements of the dislocation structure in the case of a cellular network substructure was determined as the distance between dislocation pileups; in a band substructure, as the distance between subboundaries; and in a fragmented substructure, as the fragment size.

It was established that the λ and $\bar{d}$ values exhibit correlation (see figure) described by a simple linear (correlation coefficient, ~0.9) relation of the type

$$\lambda = \lambda_0 + \alpha\bar{d}, \quad (1)$$

where $\alpha \approx 1.3 \times 10^4$ is a dimensionless coefficient and $\lambda_0 \approx 4.2$ mm is a constant quantity.

Let us consider the qualitative meaning of this relationship. Recently [6, 8], it was demonstrated that (i) localization of the plastic flow is a result of the self-organized elementary events of plastic straining in crystals and (ii) the kinetics of this process obeys the so-called reactive diffusion equations describing changes in the elastic stress and plastic strain fields. A

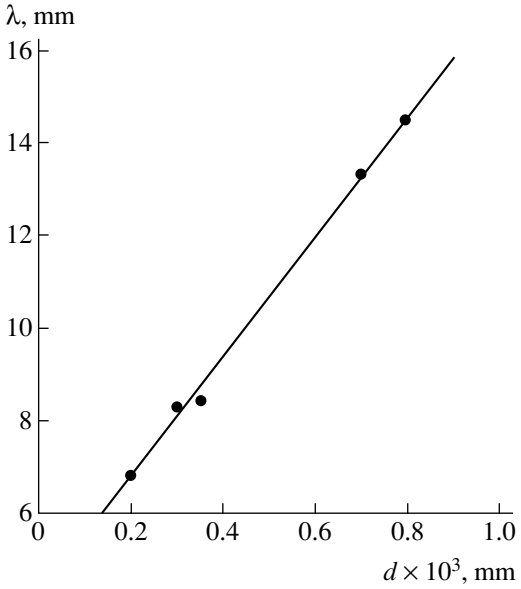

A plot of the wavelength λ of localized straining versus the average size $\bar{d}$ of elements of a dislocation structure for a zirconium alloy.

1063-7850/03/2906-0519$24.00 © 2003 MAIK "Nauka/Interperiodica"

diffusion-like transport coefficient D entering into these equations [6, 8] determines the spatial macroscopic periodicity of the strain field in terms of the well-known relation

$$\lambda^2 \approx D\Theta, \tag{2}$$

where Θ is the temporal period of the process. Previously [9], it was established in the diffusion approximation that the D value is determined on a macroscopic level by a relation involving the spatial scale Λ_{meso} of the lower (mesoscopic) level:

$$D = \Lambda_{meso} V_S = \frac{\Lambda_{meso}^2}{\tau}, \tag{3}$$

where τ is the characteristic time of relaxation of the dislocation processes and V_S is the rate of redistribution of the elastic stresses (sound velocity). Substituting formula (3) into relation (2), we obtain

$$\lambda^2 \approx \Theta/\tau\Lambda_{meso}^2, \quad \text{or} \quad \lambda \approx \sqrt{\Theta/\tau}\Lambda_{meso}. \tag{4}$$

Under the natural assumption that $\Lambda_{meso} \equiv \bar{d}$, this result agrees with the experimental data.

Let us treat the problem quantitatively. Obviously, $\alpha \approx \sqrt{\Theta/\tau}$ and, using the experimental data from [10], we obtain the estimate $\Theta \approx 150$ s. The characteristic time τ can be roughly estimated within the framework of the theory of activated plastic straining [11] as

$$\tau \approx \omega_D^{-1} \exp\frac{U - \gamma\sigma}{k_B T}, \tag{5}$$

where $H = U - \gamma\sigma \approx 0.4$ eV is the enthalpy of the elementary shear event in zirconium [12], and $\omega_D = 10^{13}$ s^{-1} is the Debye frequency. For $T = 300$ K, formula (5) yields $\tau \approx 9 \times 10^{-7}$ s; therefore, $\alpha \approx \sqrt{\Theta/\tau} \approx 1.3 \times 10^4$, which coincides with the empirical coefficient of proportionality in relation (1).

The qualitative agreement of the character of relationship ($\lambda \sim \bar{d}$) and the quantitative coincidence of the experimental and calculated values of the coefficient α show the existence of interrelation between the dislocation structure of a deformed alloy and the period of localization of the plastic straining in this alloy. This result confirms the idea formulated previously [9] about the close quantitative relation of the phenomena characteristic of plastic flow on the macroscopic and microscopic levels. This relationship is mediated by diffusion-like transport coefficients and described by expressions analogous to relation (3).

REFERENCES

1. Yu. Z. Estrin and L. P. Kubin, Acta Met. **34**, 2455 (1986).
2. B. K. Barakhtin, V. I. Vladimirov, S. A. Ivanov, *et al.*, Fiz. Met. Metalloved. **63** (6), 1185 (1987).
3. G. A. Malygin, Fiz. Tverd. Tela (Leningrad) **31** (1), 175 (1989) [Sov. Phys. Solid State **31**, 96 (1989)].
4. Sh. Kh. Khannanov, Fiz. Met. Metalloved. **68** (4), 14 (1992).
5. A. S. Zaĭmovskiĭ, A. V. Nikulina, and N. G. Reshetnikov, *Zirconium Alloys in Nuclear Power Engineering* (Énergoatomizdat, Moscow, 1994).
6. L. B. Zuev, Ann. Phys. **10**, 965 (2001).
7. T. M. Poletika, V. I. Danilov, G. N. Narimanova, *et al.*, Zh. Tekh. Fiz. **72** (9), 57 (2002) [Tech. Phys. **47**, 1125 (2002)].
8. L. B. Zuev, V. I. Danilov, and B. S. Semukhin, Usp. Fiz. Met. **3**, 237 (2002).
9. L. B. Zuev, Metallofiz. Nov. Tekhn. **18** (5), 55 (1996).
10. V. I. Danilov, S. Yu. Zavodchikov, S. A. Barannikova, *et al.*, Pis'ma Zh. Tekh. Fiz. **24** (1), 26 (1998) [Tech. Phys. Lett. **24**, 12 (1998)].
11. A. Lowley and G. Mikine, *Microplasticity* (Metallurgiya, Moscow, 1972).
12. I. N. Khristenko, I. I. Papirov, G. F. Tikhinskiĭ, *et al.*, *Preparing KhFTI No. 76-51* (Kharkov. Fiz.-Tekh. Inst., Kharkov, 1976).

Translated by P. Pozdeev

Technical Physics Letters, Vol. 29, No. 6, 2003, pp. 521–522. Translated from Pis'ma v Zhurnal Tekhnicheskoĭ Fiziki, Vol. 29, No. 12, 2003, pp. 78–82.

Application of the Holographic Interferometer for Modeling of Processes in a Vapor Phase Epitaxy Reactor

V. B. Konstantinov, V. A. Babenko, and Yu. V. Zhilyaev

Ioffe Physicotechnical Institute, Russian Academy of Sciences, St. Petersburg, 194021 Russia

e-mail: V.Konstantinov@mail.ioffe.ru; babenko@mail.ioffe.ru

Received January 24, 2003

Abstract—Using holographic interferometry techniques, it is possible to visualize flows in the gas phase and obtain quantitative data about vapor phase density distribution in a given volume. The possibility of using this approach for monitoring processes in a vapor phase epitaxy (VPE) reactor has been studied using an experimental setup comprising a reactor chamber with two transparent windows, a real-time holographic interferometer, a gas supply system, and a system for visual observation of the gas flows. The results show good prospects of this method for optimization of the reactor design and the VPE process parameters. © *2003 MAIK "Nauka/Interperiodica".*

Holographic interferometry allows real-time visualization of transparent inhomogeneities, both in working equipment and in model systems reproducing processes in various reactors. The holographic diagnostics provide information about parameters of a medium which are monitored by changes in the refractive index of the gas phase [1–4]. Subsequent calculations provide information about density distribution and flow velocities in the gas phase.

In this study, we observed the flow of a gas supplied to a horizontal reactor; the gas was monitored in the direction perpendicular to the flow velocity. The experiments were performed in a model tube reactor passing inside a compact holographic interferometer.

Epitaxial films are grown under the conditions of a laminar gas flow in a reactor tube, whereby the Reynolds number of the flow ($\mathrm{Re} = D\nu\rho/\eta$) is smaller than a critical value ($\mathrm{Re}_c = 2000$); here, D is the reactor diameter, ν is the gas flow velocity, ρ is the gas density; and η is the gas viscosity. The flux of reactants to and from a substrate surface (equal to the number of molecules passing via unit area per unit time) was determined by the formula $J = (n_g - n_s)/\gamma$, where n_g and n_s are the reactant concentrations in the gas flow and at the substrate surface, respectively. In designing a reactor, it is necessary to take into account the influence of the coefficient γ on the mass transfer. This coefficient, determining the flux of reactants to the surface, is inversely proportional to the gas flow rate. In order to provide for a homogeneous growth of epitaxial films along the reactor (at a given temperature), it is necessary to select an optimum thickness of a boundary layer (consistent with variations in the temperature and reactant concentration). By changing the Reynolds number, it is possible to control simultaneously both the gas flow rate and the film growth velocity.

The holographic interferometer is used as an analyzer detecting changes in the optical density of the gas phase. Images of the interference pattern obtained using a CCD camera are displayed on a TV monitor and/or fed via interface into a computer. This device provides visualization of various physical and chemical processes in liquids and gases. The system includes a He–Ne laser with an output power of about 2 mW, a set of optical elements, a power supply unit, and a holo-

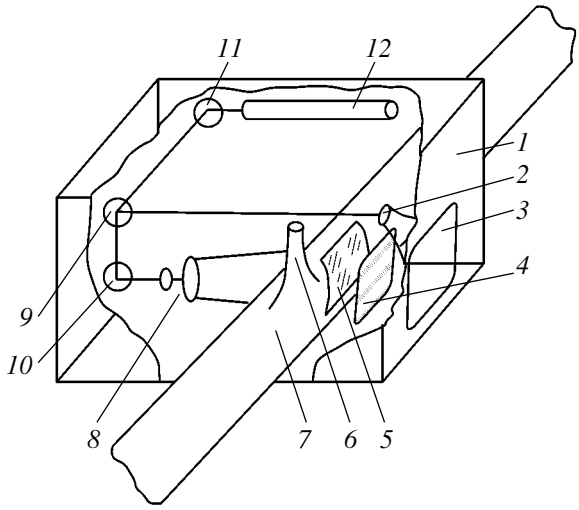

Fig. 1. Experimental setup: (*1*) holographic camera; (*2*) microlens; (*3*) hologram recorder; (*4*) diffuser (depolished glass plate); (*5*) object (reactor zone with parallel windows); (*6*) gas inlet; (*7*) tube reactor; (*8*) collimator; (*9*) beam splitter; (*10*, *11*) mirrors; (*12*) laser.

1063-7850/03/2906-0521$24.00 © 2003 MAIK "Nauka/Interperiodica"

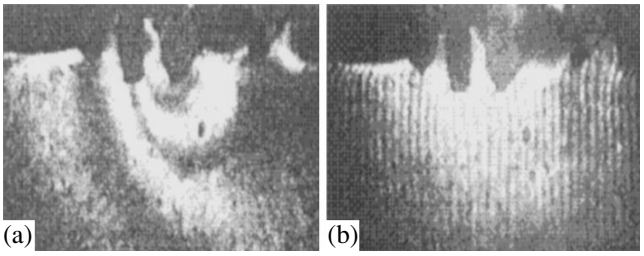

Fig. 2. A typical interferogram of helium flow monitored using bands of (a) infinite and (b) finite width.

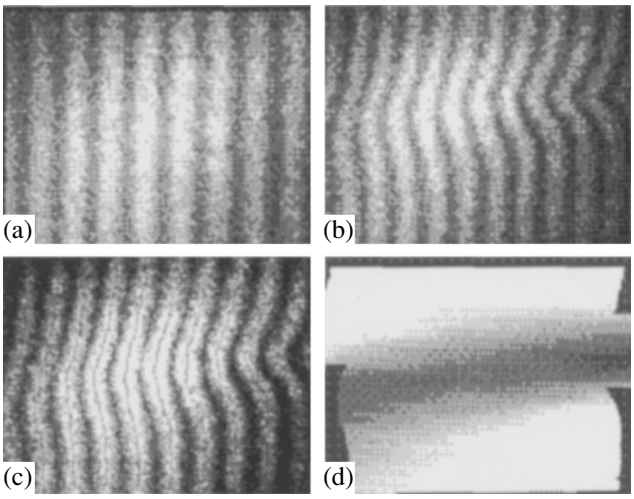

Fig. 3. Patterns illustrating visualization of a gas (propane) flow: (a) interferogram the of initial state without flow; (b) gas flow admitted; (c) calculated interferogram; (d) gas flow image.

gram recorder [5]. The experimental setup schematically depicted in Fig. 1 comprises reactor *7* and a holographic camera. A gas is supplied to the reactor via inlet *6*. The radiation of laser *12*, reflected from mirror *11*, strikes beam divider *9*. One part of the light passes through lens *2* forming the reference beam. Another part of the light reflected from mirror *10* passes through collimator *8*. Diffuser *4* facilitates localization of the interference fringes. A hologram is recorded in plane *3* onto a photothermoplastic plate. Object *5* represents the reactor interior. Windows used for transilluminating the reactor have plane-parallel surfaces. The object dimensions are $30 \times 40 \times 20$ mm; the holographic chamber *1* has the dimensions $530 \times 220 \times 130$ mm and a weight of about 6 kg. The holographic interferometer is an autonomous shock-proof device that can be installed into various working reactor systems.

Model experiments were performed with helium and propane at room temperature. Figure 2 shows typical interferograms of a helium flow. Owing to high sensitivity of the holographic interferometry, this method can be used for monitoring the flows of light gases such as helium and hydrogen (STP densities, 0.1785 and 0.08988 kg/m^3, respectively). Real-time holographic interferometry can be used for monitoring gas flow rate, detecting turbulence development at the substrate surface, etc. The regular pattern of interference bands observed in the main part of the reactor volume corresponds to a stable homogeneous laminar flow. Holographic interferometry provides information about space-averaged gas phase density gradient in the reaction zone, which is correlated with the reactant supply rate.

Using a holographic interferometer correlator [6], it is possible to monitor processes taking place in a vapor phase epitaxy (VPE) reactor. This device detects violation of the deposition process against the background of a gas flow.

Interferograms of transparent objects are processed with a computer using the specially developed software of [7]. The proposed method can be used both for real-time monitoring of processes in a reactor and for extracting quantitative information. Figure 3 gives an example of visually monitored flux of propane and the results of computer processing. The initial data are the interference pattern of a flow in the initial state and the analogous pattern obtained at a preset time. Data processing includes filtering of the images, selecting reference lines, digitizing images, and calculating changes in the refractive index. Detailed pattern of the refractive index variation over the monitored reactor zone is obtained through interpolation.

Thus, we have demonstrated that holographic interferometry techniques can be successfully used for monitoring the process of vapor phase epitaxy.

REFERENCES

1. L. Giling, J. Electrochem. Soc. **129**, 634 (1982).
2. S. M. Turilin, I. N. Sorokin, and K. I. Antonenko, Neorg. Mater. **31** (2), 151 (1995).
3. K. I. Antonenko, A. A. Arendarenkom, I. N. Sorokin, and S. M. Turilin, Izv. Akad. Nauk, Mekh. Zhidk. Gaza, No. 6, 118 (1996).
4. J. Pezol'dt, K. Antonenko, and G. Eiichorn, Mat. Res. Soc. Symp. Proc. (San Francisco) **429**, 65 (1996).
5. S. Gurevich and V. Konstantinov, Opt. J. **10**, 3 (1996).
6. S. Gurevich, V. Babenko, and V. Konstantinov, *Fringe 2001*, Ed. by W. Osten and W. Juptner (Elsevier, 2001), pp. 641–645.
7. V. Bat'kovich, O. Budenkova, V. Konstantinov, *et al.*, Zh. Tekh. Phys. **69** (6), 106 (1999) [Tech. Phys. **44**, 704 (1999)].

Translated by P. Pozdeev

Technical Physics Letters, Vol. 29, No. 6, 2003, pp. 523–524. Translated from Pis'ma v Zhurnal Tekhnicheskoĭ Fiziki, Vol. 29, No. 12, 2003, pp. 83–88.

Real-Time Holographic Interferometer Correlator

V. A. Babenko, S. B. Gurevich, V. B. Konstantinov, V. M. Levushkin, and A. F. Malyĭ

Ioffe Physicotechnical Institute, Russian Academy of Sciences, St. Petersburg, 194021 Russia

e-mail: V.Konstantinov@mail.ioffe.ru; babenko@mail.ioffe.ru

Received January 24, 2003

Abstract—We suggest using a holographic interferometer correlator for a real-time analysis of changes in objects transparent in the visible spectral range. Combined with determination of the correlation function, holographic interferometry ensures high-quality visualization of the phase inhomogeneities in transparent objects.

For detecting changes in the state of a three-dimensional object, it is sometimes necessary not only to know the distribution of the refractive index but also to detect integral changes in the object at a current moment relative to the initial moment. Illuminating a hologram by a reference wave, we obtain a reconstruction of the object wave, while illuminating this hologram by an object wave reconstructs the reference wave. If the object wave exhibits a change, the intensity of the reconstructed reference wave drops to zero and the correlation between the initial object wave and that illuminating the hologram for reconstruction disappears [1, 2].

Using compact holographic interference devices developed previously [3–6], we have designed and constructed a new holographic interferometer correlator for real-time monitoring of changes in phase-contrast objects. The principle of the device operation is based on the two-beam writing of a hologram of the initial state, followed by two-beam reconstruction of the wave front using an unchanged reference beam and a variable object beam (reflecting changes in the medium studied). The output information reflects both the difference between interference patterns of the initial and current states (determined from an image reconstructed by the reference beam) and the correlation function reflecting integral changes (a difference between the initial and final states determined from an image reconstructed by the object beam reflecting the changed state).

A plane reference wave is incident onto the hologram plane at an angle θ. Using the directions around this angle and $\theta = 0$ (perpendicular to the hologram plane) in reconstructing the wave front by the reference wave and the signal wave of a changed phase object, it is possible to obtain on a real-time scale both the interference pattern and the correlation function reflecting changes in the phase distribution in the object [7].

The initial and changed states of the medium are written and viewed in the transmission mode when the object beam passes through the medium. The object is observed with a CCD camera, the output signal of which is fed to a storage oscillograph.

We have performed two series of experiments. In the first case, the temperature of the medium changed with time. The corresponding variations in the refractive index detected by passing a changed object beam with superimposed image of the initial state (reconstructed from the initial hologram) yield a pattern of variations in the spatial temperature distribution at each moment of time. Simultaneously, the changed object beam reconstructs the current shape of the focused reference beam representing a correlation function reflecting integral changes in the new state of the object relative to the initial state. Figure 1 shows a pattern of interference bands observed on heating water in a cell.

In experiments of the second series, we used the correlation function to determine the change in the velocity of a liquid flowing through a medium. First, a hologram of the initial state of the liquid flowing at a preset

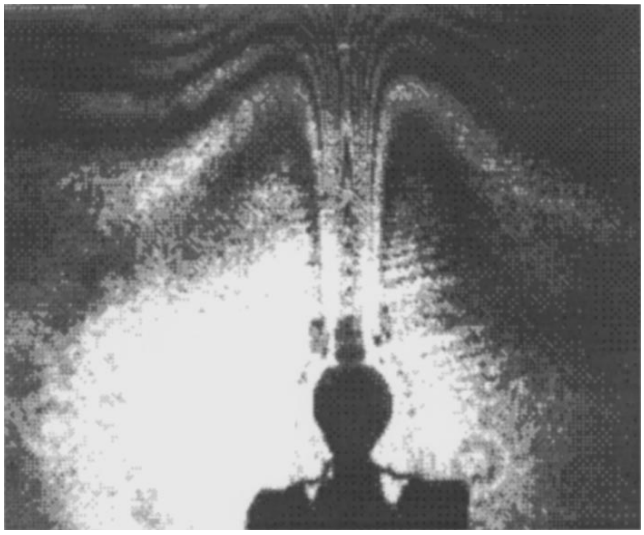

Fig. 1. Interferogram of a flow of heated liquid in a cell.

1063-7850/03/2906-0523$24.00 © 2003 MAIK "Nauka/Interperiodica"

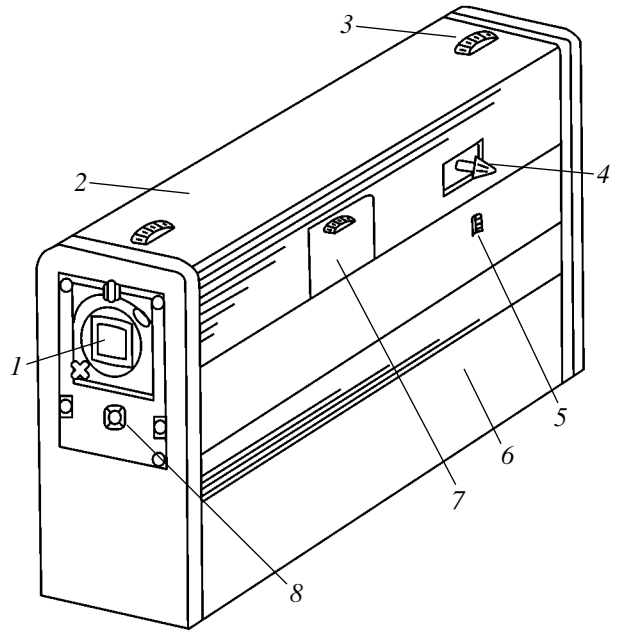

Fig. 2. General view of the holographic interferometer correlator: (*1*) viewing window; (*2*) upper panel (removable); (*3*) fixing clamps; (*4*) carrier; (*5*) shutter; (*6*) bottom panel (removable); (*7*) window for test object; (*8*) CCD camera connector.

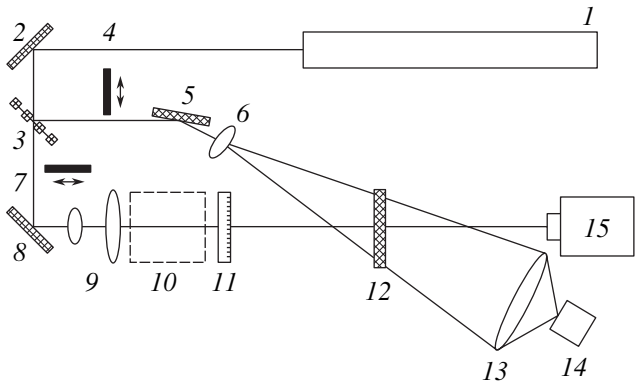

Fig. 3. Optical scheme of the holographic interferometer correlator: (*1*) laser; (*2*, *5*, *8*) mirrors; (*3*) beam divider; (*4*, *7*) shutters; (*6*) microlens; (*9*) collimator; (*10*) object; (*11*) diffuser; (*12*) hologram recorder; (*13*) lens; (*14*) TV camera; (*15*) photodetector.

velocity was written. If the flow velocity remains unchanged, the image reconstructed using an object beam in the focal plane yields a point corresponding to a correlation function in the form of the δ function. When the liquid flow velocity changes, a difference between the initial changed velocities can be determined from a distribution that appears instead of the δ function.

The experimental setup with dimensions 530 × 220 × 130 mm and a weight of about 6 kg includes a He–Ne laser operating at a wavelength of 0.63 μm and an output power of about 1 mW, a set of optical elements, a power supply unit, a hologram recorder, and a cell with liquid medium. The cell is equipped with a heater for the first experiment and with a pump controlling the liquid flow velocity for the second experiment. The holograms of the initial state were written on PFG-05 photographic plates or on FTPN photothermoplastic plates. An advantage of the latter material consists in the ability of dry self-development. The maximum hologram size is 60 × 60 mm and the maximum object dimensions are 40 × 40 × 100 mm. Figure 2 presents a general view of the holographic chamber. All experimental data can be processed and analyzed by a computer using a special program package [8].

Figure 3 shows an optical scheme of the holographic interferometer correlator. Here, the light beam of laser *1* reflects from mirror *2* and passes through beam divider *3*. One part of the light passes through lens *6* to form the reference beam. Another part of the light, passed through collimator *9*, forms the object beam. Diffuser *11* facilitates visualization of the interference bands. The object and reference beams yield an interference pattern in the plane of the hologram recorder *12*. TV camera *14* is used for visual monitoring of the object. The reference source intensity is measured by photodetector *15*. Shutters *4* and *7* are used for blocking the object and reference beams during observations of a reconstructed pattern.

Thus, the holographic interferometer correlator described above provides for a real-time monitoring of spatial changes in the medium and overall changes in the system during physical and physicochemical experiments. This system can also be used for the investigation of optical inhomogeneities in phase-contrast objects.

Acknowledgments. This study was supported by the Russian Foundation for Basic Research, project nos. 00-15-96771 and 02-02-17689a.

REFERENCES

1. S. B. Gurevich, V. B. Konstantinov, V. F. Relin, and V. A. Babenko, Proc. SPIE **3402**, 344 (1997).
2. V. V. Nekrasov, Opt. Zh., No. 5, 72 (1995).
3. V. A. Babenko, E. V. Konstantinova, and V. B. Konstantinov, Proc. SPIE **2329**, 379 (1995).
4. V. A. Babenko, L. F. Grebenovskaya, E. V. Konstantinova, *et al.*, Prib. Tekh. Éksp. **42** (1), 159 (1999).
5. V. A. Babenko, L. F. Grebenovskaya, E. V. Konstantinova, *et al.*, *Abstracts of Papers*, *International Conference of Young Scientists "Optics-99," St. Petersburg, 1999*, p. 204.
6. V. A. Babenko, V. B. Konstantinov, and V. M. Levushkin, Nauch. Pribor. **10** (1), 97 (2000).
7. S. B. Gurevich, V. B. Konstantinov, V. F. Relin, and V. A. Babenko, Proc. SPIE **3238**, 16 (1997).
8. V. V. Bat'kovich, O. N. Budenkova, V. B. Konstantinov, *et al.*, Zh. Tekh. Fiz. **69** (6), 106 (1999) [Tech. Phys. **44**, 704 (1999)].

Translated by P. Pozdeev

Technical Physics Letters, Vol. 29, No. 6, 2003, pp. 525–527. Translated from Pis'ma v Zhurnal Tekhnicheskoĭ Fiziki, Vol. 29, No. 12, 2003, pp. 89–94.

An Analog of the Hollow Cathode Effect in Low-Pressure High-Frequency Capacitive Discharge

D. A. Malik, K. E. Orlov, A. S. Smirnov, and T. V. Chernoizyumskaya

St. Petersburg State Technical University, St. Petersburg, 195251 Russia

e-mail: orlov@phtf.stu.neva.ru

Received January 24, 2003

Abstract—We have studied the process of ion flux formation in a low-pressure high-frequency capacitive discharge in the presence of a cavity on the electrode surface. If the cavity size is on the order of an electrode space charge sheath thickness, the spectrum of ions arriving at the cavity bottom surface contains a low-energy peak. The mechanism responsible for this peak is analogous to the hollow cathode effect in a dc discharge. © *2003 MAIK "Nauka/Interperiodica".*

Radio-frequency E-type (RFE) discharge is widely used in plasma technologies for thin film deposition [1]. Homogeneity of such coatings is provided by leveling plasma parameters over the entire discharge volume. If the processed surface has a developed relief, the structure of plasma in the electrode sheaths is significantly disturbed in the region of inhomogeneities on the electrode surface [2].

We have experimentally studied the process of plasma formation and the structure of electrode space charge sheaths in a low-pressure RFE discharge in the region of electrode surface inhomogeneity representing a cavity. This study was aimed at establishing a relation between discharge parameters in the electrode cavity and in the discharge bulk.

The experiments were performed using the experimental setup schematically depicted in Fig. 1a. An RFE discharge was initiated between two planar electrodes. The top electrode (22 cm in diameter) was connected to a high-frequency (13.56 MHz) voltage source. The bottom electrode was grounded and connected to the discharge chamber. The power deposited in the discharge could be varied from 0.5 to 100 W. The inert working gas (Ar) pressure was within 5–30 mTorr. The process of electrode space charge sheath formation was studied by measuring the energy spectrum of ions arriving at the grounded electrode surface. The ions were collected via a 1-mm-diam orifice in the bottom electrode. A multigrid retarding-field energy analyzer [3–5] was mounted in a lower differentially pumped high-vacuum chamber. The energy spectrum of ions was obtained by differentiating the retarding energy curves. The total energy resolution in the spectra was on the order of 1 eV. The system design allowed the measurements to be performed in two regimes, representing a plane electrode and an electrode with cavity. In the latter case the inhomogeneity on the electrode surface was modeled by placing a disk with cylindrical opening (10 mm in depth and 15 mm in diameter) onto the grounded bottom electrode, so that the axes of the cylindrical opening and the energy analyzer entrance hole would coincide (Fig. 1a).

In the first series of experiments, we measured the energy spectra of ions arriving at the plane electrode surface. These spectra exhibit a pronounced peak in the region of energies close to the maximum ion energy. The shape of the spectrum shows no significant changes with increasing power deposited in the discharge, while the maximum ion energy exhibits mono-

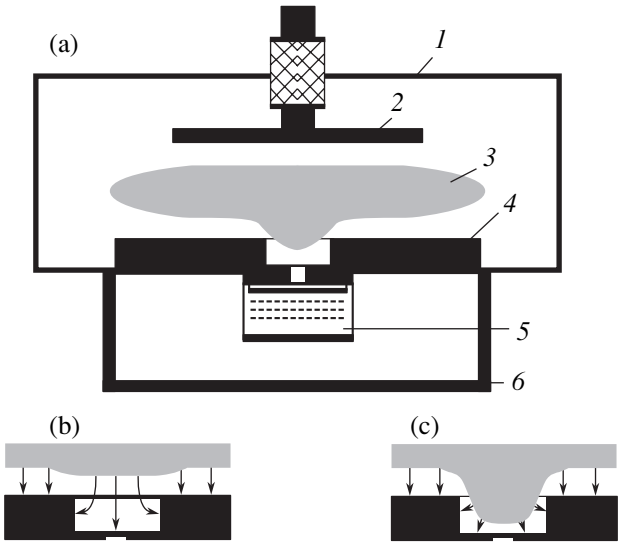

Fig. 1. Schematic diagrams of (a) experimental setup and (b, c) plasma structure in the region of a cavity on the electrode surface: (*1*) discharge chamber; (*2*) high-frequency electrode; (*3*) quasineutral plasma; (*4*) grounded electrode; (*5*) multigrid retarding-field energy analyzer; (*6*) high-vacuum chamber.

1063-7850/03/2906-0525$24.00 © 2003 MAIK "Nauka/Interperiodica"

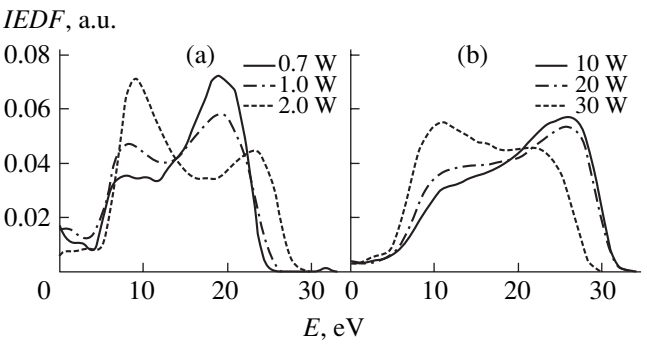

Fig. 2. Ion energy spectra (normalized to the total ion flux) for various levels of high-frequency power deposited in the discharge in Ar at $p = 5$ mTorr.

tonic growth due to increasing voltage drop across the sheath. Analogous results were repeatedly observed and interpreted by various researchers [5–7].

In the second series of experiments, we measured the flux of ions arriving at the bottom of the cavity. In this case, evolution of the spectra (Fig. 2) with increasing power deposited in the discharge significantly differs from the pattern observed with plane electrode. At a relatively low power (Fig. 2a), the energy spectrum of ions is similar to that observed with a plane electrode. As the discharge power increases, an additional low-energy peak (corresponding to an ion energy of ~7–10 eV) appears in the spectrum. Further growth of the discharge power (Fig. 2b) leads to reverse variation, and the low-energy spectral features eventually disappear.

In order to interpret the above results, let us consider the mechanism of electrode space charge sheath formation in low-pressure RFE discharge. In the indicated range of discharge parameters, the plasma obeys the condition $\omega_i \ll \omega \ll \omega_e$ (where ω_i and ω_e are the ion and electron plasma frequencies, respectively, and ω is the frequency of the applied driving voltage). In this case, ions form a steady-state concentration profile determined by a period-average electric field strength, while the motion of electrons is controlled by the instant field strength. The central region of discharge features a quasineutral plasma, and the near-electrode region represents a positive space charge layer. The thickness of the space charge layer region and the voltage drop across this region vary between zero and maximum values (L and U_{max}, respectively) during the field variation period. The shape of the energy spectrum of ions arriving at the plane electrode surface is determined by the relation between the mean free path of ions (λ) and the maximum thickness L of the electrode space charge sheath. In a collisionless regime ($\lambda \gg L$), the ion energy equals the period-average potential drop $\langle U \rangle$ across this layer and the spectrum exhibits a pronounced peak at an energy of $e\langle U \rangle$.

An analysis of the experimental spectra of ions measured with a planar electrode shows that the motion of ions in the electrode space charge sheath occurs in a low-collision regime ($\lambda > L$). The ratio of the mean free path of ions to the maximum layer thickness λ/L can be estimated from the exponential decay in the low-energy region of the experimental spectrum. At a working gas pressure of 5 mTorr, this ratio amounts to about 4–5. Then, using the known cross section for the argon charge-exchange collisions [8], we can estimate the space charge layer thickness as $L \sim 0.5$ cm.

In the presence of a cavity on the electrode surface, the electrode space charge sheath formation must obviously depend on the ratio of the inhomogeneity size (d) to the space-charge layer thickness L. For $d \ll 2L$ (thick layer) and $d \gg 2L$ (thin layer), the two-dimensional perturbation of the structure of an electrode space charge sheath and a quasineutral plasma is minimal. In the intermediate case ($d \sim 2L$), the surface inhomogeneity significantly violates the potential distribution in the boundary region. Under the experimental conditions studied, $d = 15$ mm and the above estimate of the space charge layer thickness yields $2L \sim 1$ cm. Therefore, the potential shape in the cavity significantly differs from that in the initial planar case, comprising both normal (perpendicular to the cavity bottom) and radial electric field components (Fig. 1b).

The experimentally observed variations in the energy spectrum of ions arriving at the bottom cavity (Fig. 2) can be explained with allowance of the secondary electron emission from the electrode surface and the effects analogous to those observed in a dc discharge with hollow cathode [9]. Electrons emitted from the cavity surface are confined in a radially symmetric potential and can leave the cavity only after several flights in radial directions. Accordingly, the mean free path of such secondary electrons in a two-dimensional layer is many times greater than as compared to the case of a plane electrode. At a small deposited power, the potential drop in the layer is insufficient for accelerating the secondary electrons up to the potential of ionization of Ar atoms. As the discharge power grows, both the total potential drop across the layer and the energy acquired by the secondary electrons in the radial field increase.

The first change observed in the spectrum (Fig. 2a) corresponds to the moment at which the radial electric field becomes sufficiently strong to accelerate the secondary electrons up to the potential of ionization of Ar atoms ($\epsilon_i = 15.8$ eV): $eU_{max}d/(L + 2d) \sim \epsilon_i$. Here, it should be taken into account that electrons are accelerated in the radial electric field equal to the instantaneous value of the high-frequency field applied to the layer. The period-average potential accelerating ions is lower approximately by half and, hence, the energy of ions produced by ionization in the cavity must be on the order of 8 eV, in agreement with the value observed in experiment. As can be seen from Fig. 2a, the flux of ions produced by ionization in the space charge layer (with an energy of $\epsilon \sim \epsilon_i/2$) is comparable with the flux

of ions supplied from the plasma–layer interface ($\epsilon \sim \epsilon_{max}$).

As the discharge power increases, the efficiency of ionization in the cavity grows and the corresponding ion density (n_i) increases. The maximum thickness of the space charge layer is related to the ion density and the maximum potential drop across the layer as $L \sim (U_{max}/en_i)^{1/2}$ [10]. Since the voltage across the layer is determined by the condition of equipotential quasineutral plasma in the discharge bulk, a local increase in the ion density leads to a decrease in the space charge layer thickness in the cavity. As a result, the cavity becomes filled with a quasineutral plasma and the plasma–space charge layer boundary follows the cavity surface shape (Fig. 1c). In this case, all ions arriving at the cavity surface are accelerated by the total potential drop in the layer. As a result, the ion energy spectrum exhibits a change (Fig. 2b) manifested by disappearance of the low-energy features. Thus, variation of the discharge power leads to the transition from a "thick" ($d \ll 2L$) to "thin" ($d \gg 2L$) space charge layer regime. An additional ionization by secondary electrons confined by the radially symmetric potential in the cavity accounts for an increase in the ion current to the cavity surface as compared to the case of plane electrode.

Acknowledgments. This study was supported by the Russian Foundation for Basic Research (project no. 01-02-16874) and by the NATO Science for Peace Program (grant no. 974354). One of the authors (K.E.O.) received support within the framework of the Joint Project of the Ministry of Education of the Russian Federation and the St. Petersburg Administration.

REFERENCES

1. *Plasma Processing for VLSI*, Ed. by N. Einspruch and D. Brown (Academic, New York, 1984; Mir, Moscow, 1987).
2. C.-K. Kim and D. J. Economou, J. Appl. Phys. **91**, 2594 (2002).
3. I. G. Kozlov, *Current Problems in Electron Spectroscopy* (Atomizdat, Moscow, 1978).
4. C. Bohm and J. Perrin, Rev. Sci. Instrum. **64**, 31 (1993).
5. A. S. Smirnov, K. S. Frolov, and A. Yu. Ustavshchikov, Zh. Tekh. Fiz. **65** (8), 38 (1995) [Tech. Phys. **40**, 768 (1995)].
6. A. S. Abramov, A. Ya. Vinogradov, A. I. Kosarev, *et al.*, Zh. Tekh. Fiz. **68** (2), 52 (1998) [Tech. Phys. **43**, 180 (1998)].
7. K. Kohler, J. W. Coburn, D. E. Horne, *et al.*, J. Appl. Phys. **57**, 59 (1985).
8. S. C. Brown, *Basic Data of Plasma Physics* (MIT Press, Cambridge, Mass., 1959; Atomizdat, Moscow, 1961).
9. B. I. Moskalev, *Hollow Cathode Discharge* (Énergiya, Moscow, 1969).
10. A. S. Smirnov, Zh. Tekh. Fiz. **54** (1), 61 (1984) [Sov. Phys. Tech. Phys. **29**, 34 (1984)].

Translated by P. Pozdeev